The Effects of Wind Energetics on the Angular Momentum Outflow from Late-Type Stars

Georgios Pantolmos

Submitted by Georgios Pantolmos to the University of Exeter as a thesis for the degree of Doctor of Philosophy in Physics, August, 2018.

I certify that all material in this thesis which is not my own work has been identified and that no material has previously been submitted and approved for the award of a degree by this or any other University.

Signed: .....

Georgios Pantolmos

Date: .....

Abstract

Sun-like and low-mass stars (i.e. late-type stars) possess high temperature coronae and lose mass in the form of stellar (or coronal) winds, driven by thermal pressure and complex magnetohydrodynamic processes. The effect of coronal winds on the stellar mass during a star's main-sequence life is relatively small, but they have an enormous impact on stellar rotation by exerting a spin-down torque on the stellar surface, a mechanism known as magnetic braking. The critical parameter, which determines the stellar-angular-momentum loss, is the Alfvén radius, the radius at which the flow reaches the local Alfvénic speed. This critical radius represents the effective lever-arm of the outflow and determines the efficiency of the braking torque.

From a theoretical perspective, the objective is to provide analytic stellar-torque prescriptions based on fundamental stellar parameters (e.g. stellar mass, radius, rotation rate, magnetic field properties, and coronal conditions). Studies, employing multidimensional stellar wind simulations, demonstrated that the effective lever arm (or Alfvén radius) scales as a power law with a quantity called the wind magnetization, which depends on stellar parameters (i.e stellar mass, radius, mass-loss rate, and surface magnetic field strength). Using this method, we investigate how the wind energetics, which affect the flow velocity and acceleration profile, can influence the magnetic braking of late-type stars. In this work, with the use of 2.5D stellar-wind numerical simulations, we show that a faster wind has a smaller magnetic lever arm, and therefore the braking torque exerted on the star decreases. We derive new predictive torque formulae that quantify this effect over a wide range of flow acceleration profiles. We further show how numerical-diffusion effects (due to different approaches in the simulation setup) can influence the accuracy of the torque prescriptions presented here.

Contents

List of Figures

List of Tables

Declaration

I declare that all the research presented in this thesis was performed by myself, in collaboration with my PhD supervisor Sean P. Matt. All the numerical simulations presented in this work were completed with the PLUTO code, developed by Andrea Mignone and his collaborators at the University of Torino. In this thesis, Chapter 3 is presented as it was accepted for publication in the Astrophysical Journal.

Acknowledgements

First and foremost, I would like to express my deep gratitude to Sean Matt and Matthew Browning, my research supervisors, for their support, patient guidance, enthusiastic encouragement, and useful critiques of this research work

I would like to thank Claudio Zanni for his help with the PLUTO code. Also, I am particularly grateful to my Ph.D mentor Gyaneshwar (GP) Srivastava.

I thank my colleagues in the AWESoMeStars group, Victor See, Louis Amard, Dominique Meyer, and Adam Finley for the all the fruitful and stimulating discussions during the last years.

I thank my examiners Moira Jardine and Clare Dobbs for their helpful comments on improving this work.

Last, and certainly not least, I wish to thank my family and Eva for their support and encouragement throughout my studies and life in general.

Georgios Pantolmos

Exeter, U.K.

6th August 2018

Chapter 1

Introduction

A *stellar wind* is the continuous, supersonic outflow of gas from the outer atmosphere of a star. The terms *stellar wind* and *solar wind* (i.e., the solar example of a stellar wind) were first introduced by Eugene Parker (1958, 1960) in his pioneering work on describing the dynamics of the solar wind (i.e., streams of plasma launched from Sun's atmosphere, which expand throughout the heliosphere with supersonic speeds). Over the last 60 years, several studies, on the theory and observational properties of stellar winds, have shown that undoubtedly all type of stars are subjected to outflows, during all the stages of their lives, from the very beginning, when they are born in the hearts of big molecular clouds, until their death (see e.g., textbooks by Lamers and Cassinelli 1999; Hartmann 2001; Tsinganos et al. 2009, and references therein). Stellar winds can affect the evolution of a star (e.g., Lamers and Cassinelli 1999), create planetary nebulae and cosmic superbubbles due to their interactions with the ambient medium (e.g., Kwok 1994; Lamers and Cassinelli 1999; Balick and Frank 2002), and have an impact on planet formation and evolution (e.g., Ollivier et al. 2009; Lammer and Khodachenko 2015; Lammer and Blanc 2018). Futhermore, they play an important role in star formation (e.g., Krumholz et al. 2014; Krumholz 2015), enrich the interstellar medium with chemical elements (e.g., Tielens et al. 2005), are among the drivers of galactic outflows that influence the evolution of both the galaxies and Universe (e.g., Veilleux et al. 2005). It is clear that studying the physical processes related to stellar outflows is of great importance to our understanding the nature

of stars, planets and galaxies.

This thesis focuses on stellar winds from late-type stars (i.e., Sun-like and low-mass stars), which are called coronal winds (see below). Such outflows affect the rotation of these stars, because they can effectively remove stellar angular momentum and therefore slow down the stellar rotation (see e.g., Bouvier et al. 2014). This is the so-called *magnetic braking* by a stellar wind (for more details see discussion below). The objective in our work is to use multidimensional numerical simulations, to investigate and quantify how variations in the energetics of coronal winds, affect the spin-down of late-type stars.

In the following section (§1.1), we introduce the different types of stellar winds, as they can be classified, based on their driving mechanisms. Since we focus on coronal winds, in section 1.2 we briefly review aspects on the theory and observations of the solar wind, which is the best studied example of a coronal wind. In section 1.3 of this chapter we discuss the angular-momentum-loss problem in late-type stars. Finally, we close this introduction with section 1.5, presenting the overall structure of this thesis.

1.1 Introduction to Stellar Winds

Stellar winds from stars of different spectral types and/or in different stages of their stellar evolution involve different driving physics. Therefore, stellar winds can be classified in three broad categories, based on the physical processes that accelerate the stellar material. These classes include: 1) line-driven winds; 2) dust-driven winds; and 3) coronal winds.

In this section, we briefly intoduce the mechanisms which trigger these three types of stellar outflows, and their global properties, such as wind mass loss rates and terminal speeds. This is presented to highlight how the properties of coronal winds differ from their counterparts of other classes of stellar outflows. Furthermore, this discussion informs the wind modeling and input parameters adopted for the studies presented in the following chapters.

1.1.1 Line-Driven Winds

This class of stellar outflows is driven by scattering of the star's continuum radiation in a large ensemble of spectral lines (see e.g., Castor et al. 1975; Lamers and Cassinelli 1999; Owocki 2009a, 2015). The photospheric radiation flux transfers momentum to the gas in the stellar atmosphere, producing a radiative acceleration, which drives a stellar wind. Such outflows are often referred in the literature as radiatively-driven winds. Line-driven winds from massive, hot, luminous stars (of types O, B and A) exhibit terminal speeds up to ~ 3000 km s^{-1}, with mass-loss rates as high as $\sim 10^{-5} M_{\odot}$ yr^{-1} (see e.g., Pauldrach et al. 1986; Lamers and Cassinelli 1999, and references therein). Such high mass-loss rates cause the star to lose a significant fraction of its initial stellar mass during main sequence life, with consequenses for its stellar evolution (Castor et al. 1975).

A small population of early-type stars ($\sim 10\%$ of type O and B) possess large-scale, organized magnetic fields (mostly dipolar, with ranges in dipolar strength from 10^2 to a few times 10^4 G, Petit et al. 2013). The interplay between a line-driven wind and a rotating magnetic field leads to stellar angular momentum loss, causing rotational braking (Ud-Doula et al. 2009; Townsend et al. 2010). Furthermore, these fields determine the global structure of the outflow, by chanelling the stellar plasma in the wind zone. In addition, wind-fed magnetospheres are formed by material that is trapped in closed magnetic loops. This latter feature impacts the observational properties of early-type stars (e.g, in X-ray and Balmer line emission, ud-Doula et al. 2013; ud-Doula et al. 2014; Owocki et al. 2016, and references therein).

1.1.2 Dust-Driven Winds

Dust-driven winds are observed from luminous, cool, post-main sequence stars (see e.g., Sedlmayr and Dominik 1995; Cox et al. 2012). This class of stellar outflows is driven due to absorption and scattering of the stellar continuum radiation by dust grains, formed in the circumstellar envelopes, in which these evolved stars are embedded (see e.g. Gilman 1972; Lamers and Cassinelli 1999). Dust-driven winds can also be referred as radiatively accelerated flows but they should be distinguished from line-driven winds, because their driving mechanism is different. Red supergiants and asymptotic giant branch stars, with

effective temperatures from 2000 to 3000 K, allow grain formation and growth in their outer atmospheres (e.g., silicate and carbon grains; for more details see Lamers and Cassinelli 1999; Höfner 2015). The dust grains, which are coupled to the gas (due to collisions), gain momentum due to the interactions with the stellar photons. As the dust particles move outwards, transfer momentum to the gas by dragging it along, and the whole process triggers this type of stellar outflows. More recent studies show that shock waves, due to stellar pulsations, are also important for the driving of these winds (see e.g., Höfner 2015). Dust-driven winds are slow, with typical speeds of $\lesssim 40$ km s^{-1}, but with high mass-loss rates, $10^{-8} - 10^{-4} M_{\odot}$ yr^{-1}, which siginificantly influence star's structural evolution (see e.g., Sedlmayr and Dominik 1995; Lamers and Cassinelli 1999).

Lastly, it should be mentioned, that dust-driven-wind theory may not be capable of explaining the slow stellar outflows ($\lesssim 100$ km s^{-1}) from late-type, cool giant stars (see e.g., Dupree 1986; Harper 1996; Lamers and Cassinelli 1999). Magnetohydrodynamic processes, similar to the ones proposed to drive coronal winds (e.g., dissipation of Alfvén waves), may also be involved in the outflow acceleration mechanism from these giant stars (see e.g., Suzuki 2007; Cranmer and Saar 2011, and references therein).

1.1.3 Coronal Winds

Coronal winds are driven by gas thermal pressure and magnetohydronamic processes, such as dissipation of magnetic waves, turbulence, and magnetic reconnection (see e.g., Lamers and Cassinelli 1999; Cranmer 2008). Magneto-centrifugal forces, due to the combined effects of fast stellar rotation and magnetism, can also contribute to the driving of coronal winds (see e.g., Belcher and MacGregor 1976; Washimi and Shibata 1993; Lamers and Cassinelli 1999; Lovelace et al. 2008; Vidotto et al. 2011; Réville et al. 2016a, and further discussion in section 2.3.2). All main-sequence, low-mass stars ($M_{*} \lesssim 1.3 M_{\odot}$), with spectral types of F and later exhibit hot (of the order of 10^{6} K) and magnetized coronae (e.g., Wright et al. 2011, 2011) and therefore are observed or believed to lose mass through this type of stellar outflows (e.g., Holzwarth and Jardine 2007; Cranmer and Saar 2011; Cohen 2011; Suzuki et al. 2013; Wood et al. 2015).

An example of a coronal wind is the solar wind. The gas located in the *solar*

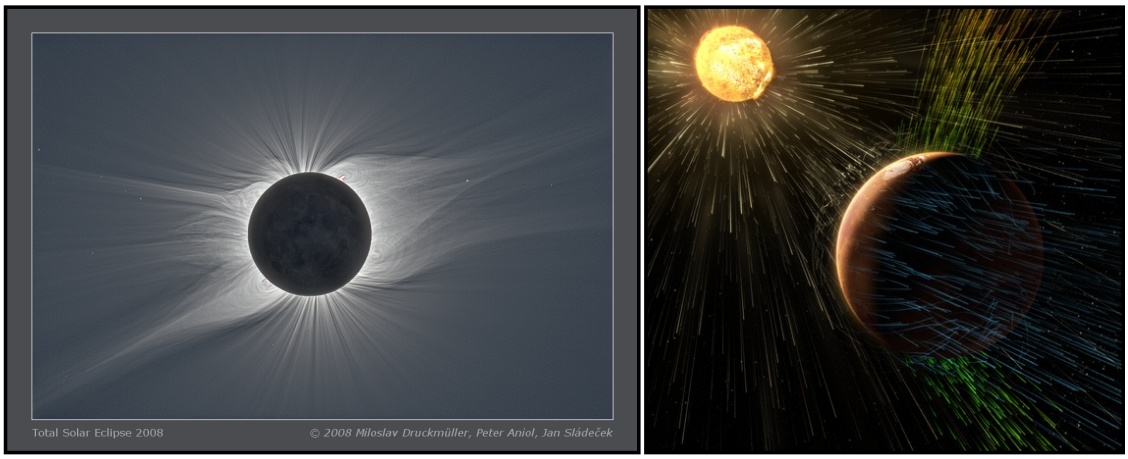

Figure 1.1: (Left) The solar corona during a 2008 eclipse (see also Pasachoff et al. 2009). The solar corona is the upper part of Sun's atmosphere, above the transition region, chromosphere, and photosphere (for more details see e.g., textbooks by Golub and Pasachoff 1997; Priest 2014). It is structured with coronal holes (i.e., regions with open magnetic field lines, along which the solar wind flows), and dead zones (i.e., regions with magnetic loops, which confine the solar plasma). Credit: Miloslav Druckmüller, Peter Aniol, Jan Sládeček. (Right) Artist's rendering of the solar wind, as expands thoughout the interplanetary space, interacting with the martian atmosphere. Credit: NASA/GSFC.

corona, the upper layers of Sun's atmosphere (see left panel of figure 1.1), is heated to temperatures of a few times 10^6 K. The hot solar plasma exerts a gradient of thermal pressure force, which counteracts gravity, and the solar atmopshere expands outwards, forming an outflow and filling the heliosphere (see right panel of figure 1.1). Thus thermal pressure is important for accelerating the flow (Parker 1958, 1963), and therefore coronal winds are often called thermally-driven winds. However, thermal pressure alone cannot fully reproduce the observed coronal dynamics and the resulting solar-wind acceleration (see e.g., review by Cranmer et al. 2017, and further discussion in section §1.2.2). The solar wind reaches speeds at Earth's orbit in the range between $250 - 800$ km s^{-1} (see e.g., McComas et al. 2003; McComas et al. 2008; Cranmer et al. 2017), and the solar mass-loss rate is low, about $2 \times 10^{-14} M_\odot$ yr^{-1} (see e.g., Wang 1998; Cranmer 2008), compared to mass-loss rates from other types of stellar winds.

Coronal winds have low densities and therefore, they are optically thin. As a consequence, these stellar outflows cannot be directly detected. However recent studies (Wood et al. 2002; Wood et al. 2005a; Wood et al. 2014), using spectra of the H I Lyman α

lines of nearby stars, succeeded to extract mass loss rates of coronal winds by studying the regions where these outflows interact with the interstellar medium (ISM). These interaction regions are called "astrospheres" like the heliosphere that is created by the Sun. The collision between a fully ionized stellar wind and the partially ionized ISM produces a dense region of neutral hydrogen atoms between the bow shock and the astropause. This region is called the hydrogen wall and produces absorption on the H I Lyman α line. Wood et al. (2002), Wood et al. (2005a), and Wood et al. (2014) showed that the excess H I absorption on the blue side of the line is a result of astrospheric absorption. The amount of this excess absorption, which depends on the density of the hydrogen wall, is used to compute the wind mass-loss rate. Wood et al. (2002), Wood et al. (2005a), and Wood et al. (2014) measure that that the mass-loss rates of late-type stars, due to coronal winds, can range from $0.5\dot{M}_{\odot}$ to $100\dot{M}_{\odot}$, and theroretical models predict an upper threshold for these mass-loss rates as high as $1000\dot{M}_{\odot}$ (Suzuki et al. 2013). Furthermore, studies based on numerical simulations show that coronal winds exhibit characteristics and terminal speeds similar to the ones observed in the solar wind (ranging from 200 to 1000 km s^{-1}, see e.g., Vidotto et al. 2009; Réville et al. 2016a; Alvarado-Gómez et al. 2016; O'Fionnagáin and Vidotto 2018). There is albeit the extreme case of M-dwarf V374 Peg, for which, simulations predict that magnetocentrifugal acceleration could increase wind's terminal velocity up to $\sim$ 2000 km s^{-1} (Vidotto et al. 2011). Most likely, coronal winds do not significantly influence the stellar structural evolution, but they have a major impact on the angular momentum evolution of cool main-sequence stars, by braking the rotation due to their interaction with the rotating, stellar magnetic field (see e.g., Schatzman 1962; Weber and Davis 1967; Mestel 1968; Mestel and Spruit 1987; Bouvier et al. 2014, and section §1.3).

1.2 The Solar Wind

The objective in our work is to derive magnetic-braking laws for late-type stars, based on realistic numerical modeling of coronal winds. Therefore, comprehension on how the adopted wind theory, for our studies, deviates from the current state of solar-wind knowledge is critical in order to predict the stellar rotational evolution.

In this section we discuss in more detail the global observational properties of the solar wind and the current theoretical understaning of the solar-wind acceleration problem. The solar wind represents the most well-studied case of outflows from late-type main sequence stars and the main basis of understanding the dynamics of coronal winds, because it can be directly observed.

1.2.1 Global Properties of the Solar Wind

The supersonic and magnetized nature of the solar wind was first confirmed observationally by Neugebauer and Snyder (1962, 1966), who used data from the space probe, Mariner II. Current detections show that the solar wind is organized with fast and slow streams, and furthermore, has global properties that vary during the solar 11-year sunspot (or magnetic-activity) cycle (e.g, McComas et al. 2007; McComas et al. 2013, and references therein). Despite the fact that observations reveal further long-term variability (McComas et al. 2008; McComas et al. 2013), studies predict that the global morphology of the solar wind (see below) has not significantly changed over the last 400 years (Owens et al. 2017). Since most of the structural changes in the solar wind occur during the transition from the sunspot minimun to maximum, here we briefly discuss this feature, in terms of solar wind's large-scale observational properties.

During the solar minimum, the wind is bimodal (see left panel of Figure 1.2), comprising a fast and slow wind component (e.g., Holzer 2005; McComas et al. 2007; McComas et al. 2008; Tokumaru et al. 2010; Cranmer et al. 2017, and references therein). The fast solar wind emerges from large polar coronal holes and is observed to be steady, of low density ($n \simeq 2-4$ cm^{-3}), with speeds of $450-800$ km s^{-1}. In contrast, the slow solar wind is denser ($n \simeq 5-20$ cm^{-3}) and more variable, but slower, detected with velocities of $250-450$ km s^{-1}. In addition, these slow streams emerge from lower-latitude, equatorward regions. Using measurements at 1AU of the plasma's density and velocity, the flow mass-loss rate, during the solar minimum, is estimated to be about $2\times10^{-14}M_{\odot}$ yr^{-1} (Wang 1998).

During the solar maximum, the wind is slower, more irregular, and highly variable (e.g., McComas et al. 2003; McComas et al. 2007; Holzer 2005; Tokumaru et al. 2010;

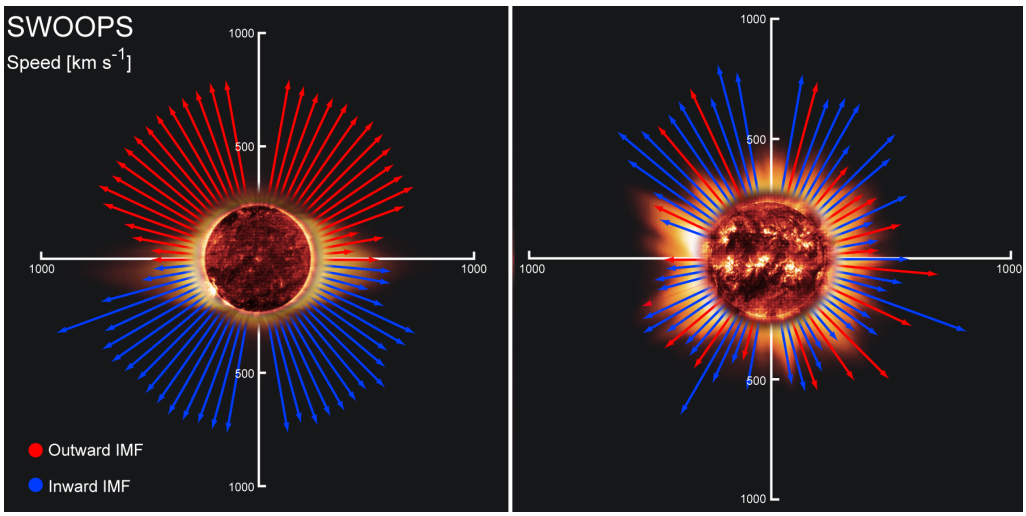

Figure 1.2: Polar plots of the solar wind speed over the first (left) and second (right) orbit of Ulysses. The vectors are blue and red coloured to show the polarity of the solar interplanetary magnetic field (IMF). At the first orbit, during the solar minimum, Ulysses captures a bimodal solar wind, with fast wind emerging from the poles, and slow wind over the equator. During the solar maximum (second orbit), Ulysses shows that solar wind becomes more irregular, with fast and slow wind components at all latitudes. (Credit: ESA; see also McComas et al. 2007)

Cranmer et al. 2017, and references therein). Observations capture slow wind at all latitudes (see right panel of Figure 1.2) and the average flow speed is around $400-500$ km s^{-1}. During the sunspot maximum, the solar mass loss rate increases and is estimated to be about $3 \times 10^{-14} M_{\odot}$ yr^{-1} (Wang 1998).

1.2.2 Theory of the Solar Wind

Parker (1958) developed the first theory, which showed the expansion of the solar corona in the form of a supersonic outflow. Under the assumptions of spherical symmetry, steady state, and an isothermal, single-species flow, Parker found that for "realistic" coronal conditions (i.e., temperature and density), the pressure of the flow, at the base of the corona, prevails over any expected interstellar pressure. Therefore, the solar atmosphere must expand supersonically as the solar wind (further details can be found in section 2.1). The description of a thermally expanding solar corona (isothermal or polytropic, see also Parker 1963; Lamers and Cassinelli 1999) has been employed in several works, either studying in more detail the dynamics of the solar wind and its interaction with the ambient solar magnetic field (e.g., Weber and Davis 1967; Pneuman and Kopp 1971;

Nerney and Suess 1975; Kopp and Holzer 1976; Steinolfson et al. 1982; Washimi and Sakurai 1993; Mikić et al. 1999; Réville and Brun 2017) or intermittent phenomena in the solar atmosphere (e.g., Linker et al. 2011; Lionello et al. 2013; Higginson et al. 2017). However, one of the inconsistencies in Parker's theory is that it cannot reproduce the observed solar-wind bimodality. Furthermore, the model requires much higher coronal-base temperatures, compared to the observed ones (at least by a factor 2, for more details see §2.1), to predict the fast solar-wind component, indicative of missing physics in Parker's formalism, which contribute to the flow acceleration.

The idea that the solar wind cannot be described as a flow driven only by thermal pressure was discussed in several early studies (e.g., Parker 1965; Holzer 1977; Jacques 1977). More recent studies show that more realistic energy sources (e.g., Alfvén waves), radiative losses, heat conduction, multi-fluid approaches are required in solar wind modeling in order to reproduce the observed wind structure and properties (e.g., Usmanov et al. 2000; Usmanov et al. 2016; Schwadron and McComas 2003; Suzuki and Inutsuka 2006; Cranmer et al. 2007; Lionello et al. 2009; Wang et al. 2009; Verdini et al. 2010; van der Holst et al. 2014, and references therein).

The solar wind is the consequence of the hot solar corona and therefore the flow energy input and resulting acceleration is related to the coronal heating problem. The physical processes that heat the solar corona to temperatures of 10^6 K, compared to the relatively cool chromosphere of 10^4 K and photosphere of 6000 K, are not well understood and still puzzle the solar community (see e.g., reviews by Aschwanden 2005; Klimchuk 2006, 2015; Parnell and De Moortel 2012; De Moortel and Browning 2015). Furthermore, the answer of how the solar corona is heated might be different, considering open (i.e., coronal holes with solar wind) and magnetically confined (or active) regions (see e.g., Aschwanden 2005; Velli et al. 2015; Cranmer et al. 2015). Here, we refer shortly to the two leading theoretical models that have been proposed to explain both the coronal heating and acceleration of the solar wind (for more details see reviews by Antiochos et al. 2012; Cranmer 2012; Hansteen and Velli 2012; Cranmer et al. 2017). In the first scenario, the required energy and acceleration to drive the solar wind is provided by turbulent dissipation driven by Alfvén waves (e.g., Cranmer et al. 2007; Verdini et al. 2010; van

der Holst et al. 2014, and references therein). The second model describes a solar wind, which is energized and accelerated by large or small scale magnetic reconnection (e.g., Fisk 2003; Schwadron and McComas 2003; Antiochos et al. 2011; Rappazzo et al. 2012, and references therein). We do not have definitive answers on how the solar corona is heated and which is the exact mechanism that accelerates the solar plasma.

For the studies presented here, we consider polytropic, Parker-like wind models. Therefore, in our wind simulations, the coronal conditions are controlled by adopting a specific value for the stellar coronal temperature and polytropic index of the flow (for more details see §2.2). From the above, it is clear that this approach is simpler than the current solar wind theory. Nonetheless, it is suitable for our work because we do not attempt to reproduce the solar case and its observational characteristics such as bimodality. Furthermore, it is still an open issue whether the current models of solar coronal heating and wind acceleration can be largely applied to every late-type star with coronal outflows, but different stellar parameters and age (see also discussion in §3.1). The objective in this work is to investigate the influence of different flow energetics on the magnetic braking of low-mass stars using a more general and comprehensive approach due to the uncertainties in the solar/stellar coronal heating problem.

1.3 The Angular Momentum Loss from Late-Type Stars

The spin-down of main sequence late-type stars was discovered by early observations, which showed the stellar rotation to decrease with advancing stellar age (Kraft 1967; Skumanich 1972). Over the last years, astronomers have provided measurements of rotation periods for thousands of low-mass stars in star forming regions and young open clusters (see e.g., Bouvier et al. 2014). A common technique on observing the rotation periods of low-mass (and magnetically active) stars is photometry. These stars exhibit starspots at their surfaces that modulate the stellar luminocity in a periodic way. From these photometric light curves, observers can infer stellar rotation periods (see e.g., Bouvier 2013). These recent observations reveal a dependence of the stellar rotation period on both the stellar mass and age (e.g., Barnes 2003, 2010; Irwin and Bouvier 2009; Meibom et al. 2011; Meibom et al. 2015; Davenport 2017). In particular, during the first few Myrs of their

lifes, late-type stars exhibit a wide distribution of spin rates. However, by an age of about 10 Gyrs they have spun down, producing a tight relation between period and mass. This relation gives the rotation rate to decrease towards a lower stellar mass (see e.g., Bouvier et al. 2014, and references therein). This feature indicates an angular-momentum-loss mechanism that depends on the stellar parameters. The rotational braking of late-type stars can be explained as a consequence of magnetically coupled stellar winds, which carry away stellar angular momentum (e.g., Schatzman 1962; Weber and Davis 1967; Mestel 1968; Mestel and Spruit 1987).

The stellar angular momentum loss is a manifestation of stellar magnetism. Late-type stars harbor global magnetic fields generated by a dynamo mechanism, driven by stellar convection and rotation (see e.g., Priest 2014; Brun and Browning 2017). The presence of magnetic fields in these stars is directly linked with the so-called stellar *magnetic activity*. Magnetic activity is a collective term which includes numerous phenomena observed in late-type stars, such as chromospheric and coronal emission (see e.g., reviews by Hall 2008; Testa et al. 2015), photospheric starspots that modulate the stellar light curves (see e.g., review by Strassmeier 2009), and mass loss in the form of magnetized outflows (see e.g., review by Wood et al. 2015). Magnetic activity is found to correlate well with stellar rotation and in particular to decrease with an increasing rotation period and thus, advancing age (e.g., Skumanich 1972; Noyes et al. 1984; Mamajek and Hillenbrand 2008; Pizzolato et al. 2003; Wright et al. 2011).

In addition, the large-scale structure of stellar magnetic fields can be mapped with the Zeeman Doppler imaging (ZDI) technique (see e.g., Donati and Brown 1997; Donati and Landstreet 2009). In the presence of a magnetic field, the Zeeman effect splits a spectral line into several components, which are called π and σ components. Then the magnetic field can be inferred from the separation of these two components. Furthermore, the polarization properties of the Zeeman splitting can give access to the orientation of the field (i.e, the line-of-sight or longitudinal, and perpendicular or transverse component of the field). The Zeeman spectropolarimetry combined with Doppler imaging (i.e., a technique to model periodic modulation of Zeeman signatures during the stellar rotation) is the ZDI technique and can provide the poloidal and toroidal components (expressed

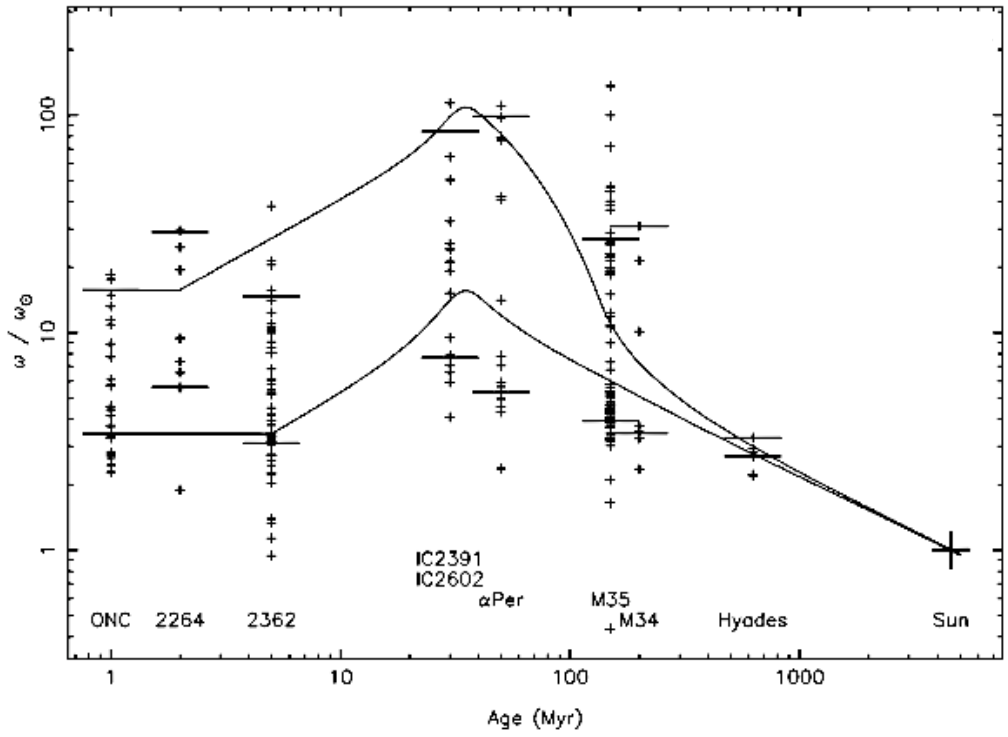

Figure 1.3: Angular velocity distributions of solar-type stars (with masses ranging from $0.9M_{\odot}$ to $1.1M_{\odot}$) in young open cluster and the Sun. $\omega_{\odot}$ is the solar rotation rate. In the figure, each cluster is represented by a vertical line consisted of crosses. The short horizontal lines show the 25^{th} and 90^{th} perecntiles of the data in order to characterize the slow and fast rotators, respectively. The black solid lines show the modeled evolution of ω in time for $1M_{\odot}$ stars, assuming solid body rotation. The clusters shown in the figure are the ONC, NGC 2264, NGC 2362, IC 2391, IC 2602, Per, M35, M34, Hyades, and the big cross represents the Sun. From Irwin and Bouvier (2009).

as spherical harmonics expansions) of the stellar magnetic field (for a detailed analysis of the ZDI technique see review by Donati and Landstreet 2009). While studies reveal a wide variety of magnetic field properties (i.e., field strength and geometry) in late-type stars, they still demonstrate a dependence of the stellar-magnetic-field generation on both stellar rotation and age (e.g., Petit et al. 2008; Vidotto et al. 2014a; See et al. 2015; See et al. 2016; Folsom et al. 2018). The existence of such a coherent age-rotation-activity relation manifests a global process, by which magnetized stellar winds brake the stellar rotation, which in turn reduces the efficiency of the stellar dynamo to produce magnetic fields.

The objective in modeling the spin-down of late-type stars is to reproduce the rotation-period distributions observed in open clusters at different ages (e.g. Reiners and

Mohanty 2012; van Saders and Pinsonneault 2013; Gallet and Bouvier 2015; Johnstone et al. 2015a; Matt et al. 2015; Amard et al. 2016; Sadeghi Ardestani et al. 2017; See et al. 2017). An example of the rotational evolution of solar-type stars is given in figure 1.3. The vertical stripes in the figure correspond to the measured rotation periods of solar type stars (with masses $0.9 - 1.1 M_{\odot}$) in young open clusters at different ages. The two black solid lines, characterizing fast and slow stellar rotators, show the modeled angular momentum evolution of $1 M_{\odot}$ stars (using solid-body rotation). During the first few Myrs (i.e., the T-Tauri phase of solar-like stars), rotation evolution models assume a constant stellar rotation period in order to fit that data. The T-Tauri phase of low-mass stars is characterized by complex magnetic interactions between the young star and its surrounding disk. When the disk dissipates the star spins up, due to contraction, and after ~ 30 Myrs, solar-type stars enter the zero-age main sequence. As the star evolves at the main-sequence, its rotation period starts to increase, due to magnetized stellar winds, which effectively remove angular momentum and threrefore, brake the stellar rotation. At about 1 Gyr, angular-momentum evolution models suggest convergence of rotation rates for both fast and slow rotators. For a more detailed discussion on the rotational evolution of solar-type stars, we point to the reader to review by Bouvier et al. (2014). Later studies show that in partially convective stars, internal angular-momentum-transport mechanisms might also be important for the stellar rotational evolution (e.g., MacGregor and Brenner 1991; Gallet and Bouvier 2013). Therefore, one of the key ingredients for the success of these models are the angular-momentum-loss prescriptions, which predict the braking torque acting on the star and therefore must depend on fundamental stellar and/or wind parameters (e.g., stellar mass, radius, rotation rate, magnetic field properties, wind mass loss rate). Assuming solid-body rotation and that magnetized stellar winds is the only mechanism braking the stellar rotation, early works attempted to provide such stellar-torque laws, but they adopted several approximations for the flow and magnetic field properties (e.g. Schatzman 1962; Mestel 1984; Mestel and Spruit 1987; Kawaler 1988). More recent studies tackle the problem by computing *physical torques*, which therefore are derived from realistic multidimensional wind simulations. There are two approaches in the literature. The first one provides scalings between the angular-momentum-loss rate and observable quantities or wind properties, derived from stellar-wind simulations for indi-

vidual stars with known stellar and magnetic field parameters (e.g., Vidotto et al. 2014b; Alvarado-Gómez et al. 2016). The second approach provides global braking laws derived from parametric studies, also based on numerical simulations. However, these studies employ a wide range of stellar, magnetic field and flow properties as input parameters for their simulations (e.g., Matt et al. 2012a; Cohen and Drake 2014; Garraffo et al. 2016; Réville et al. 2015a; Finley and Matt 2018). The latter scalings can be used in rotational evolution models. For our studies we adopt the second approach. In the next section we discuss in more detail the method used in our studies and the main motivation of this work.

Understanding the rotational evolution of late-type stars is one of the goals in stellar astrophysics, because it might explain the various trends in X-ray and chromospheric activity and therefore, provide constraints on the action of stellar dynamos (e.g. Brun et al. 2014; Brun and Browning 2017) and the stellar-corona heating problem (e.g. Cranmer 2008). In addition, by determining the rotational evolution of late-type stars stars, rotation periods can be used to extract stellar ages (i.e., the concept of Gyrochronology, e.g., Barnes 2003, 2010; van Saders and Pinsonneault 2013; Meibom et al. 2015). Furthermore, constraining the stellar angular momentum loss due to winds might be useful for rotational evolution studies, which include internal angular-momentum-transport mechanisms, in order to quantify the efficiency of these processes and their effect on the stellar rotational evolution (see e.g., Amard et al. 2016, and references therein). Lastly, during the accreting phase of T-Tauri (or pre-main sequence low-mass) stars, observations show approximately a constant stellar spin-rate (e.g., Bouvier et al. 2014), indicative of interactions between the star and disk, and angular-momentum-loss processes (including stellar winds) that prevent the star to spin up (due to both contraction and accretion, e.g., Pudritz and Matt 2014; Romanova and Owocki 2015).

1.4 A Method to Study the Effects of the Wind Enrgetics on the Magnetic Braking of Late-type stars

Weber and Davis (1967) used one-dimensional wind theory in the framework of ideal magnetohydrodynamics to show that the total specific angular momentum carried away

by the solar wind is given as the product of the stellar rotation rate times the wind Alfvén radius squared. The Alfvén radius is the distance, in which the flow becomes super-Alfvénic and acts as a lever arm to brake the stellar rotation (for a more detailed discussion on the Weber-Davis model see §2.3.1). Therefore, this critical radius determines the efficiency of the magnetic torque exerted on the star.

Matt and Pudritz (2008) derived a semianalytic stellar-torque formula by showing that the flow Alfvén radius, which determines the efficiency of the magnetic braking by a wind, scales as a power law with a quantity called the *wind magnetization*. This quantity depends on basic stellar and wind parameters (i.e., stellar mass, radius, mass-loss rate, and surface magnetic field strength, for more details see §3.3.2). After Matt and Pudritz (2008), a series of studies (Matt et al. 2012a; Réville et al. 2015a; Réville et al. 2016a; Finley and Matt 2017, 2018), improved this torque formulation by including the effects of fast stellar rotation and different or mixed field geometries. These works employed polytropic, Parker wind models, modified by rotation and magnetic fields (e.g., Washimi and Shibata 1993; Keppens and Goedbloed 1999), but they kept fixed the flow thermodynamics (i.e. coronal temperature and polytropic index), which control the wind velocity and acceleration profiles.

In this work, we employ the method introduced in Matt and Pudritz (2008). We investigate how variations in the critical parameters that influence the outflow acceleration, within the polytropic approximation, will affect the stellar angular momentum loss. For polytopic winds, these two critical parameters is the coronal temperature and the polytropic index, γ, which determines the energy input in the flow. While γ is a rather free parameter for polytropic flows (as long its value procuces accelerating flows, see discussion in the following chapters), stellar coronal temperatures can be inferred from observations. Stellar coronae exhibit closed loops, at which the plasma is trapped and heated in several millions degrees of Kelvin. Therefore, these coronal structures emit in X-ray (see e.g., Vaiana et al. 1981). Stellar coronal temperatures can be inferred from high resolution X-Ray spectroscopy, by studying lines forming at different temperatures (see e.g., reviews by Güdel 2004; Güdel and Nazé 2009). Alternatively, averaged coronal temperatures can be estimated from empirical laws, which show the levels of stellar X-ray activity to scale with

coronal plasma temperatures (see e.g., Telleschi et al. 2005). For example Johnstone and Güdel (2015), using this latter approach, estimate that the averaged coronal temperatures in low-mass stars can differ by a factor of 10. Note that, these temperatures correspond to coronal regions, at which the plasma is confined, and not to coronal holes, which are the source of stellar winds and appear dark in X-rays. For example, Aschwanden (2005) describes the solar corona to have open-field regions (i.e., coronal holes with solar wind) with temperatures of ~ 1 MK, closed-field regions (e.g., the quiet Sun) with temperatures of ~ 1 - 2 MK, and active regions with $T \sim 2-6$ MK. Therefore such coronal temperature estimations are not necessarily suitable for stellar wind modeling.

Our simulations are limited to stars which are slow rotators (i.e., magnetocentrifugal effects are negligible) and include only dipolar field geometries. Studies show that the dipole field component is the dominant one among other higher order field components (i.e. quadrupoles, octupoles, etc.) at larger scales, and the component that mainly needs to be considered when studying the magnetic braking (See et al. 2017; Finley and Matt 2018, and references therein). We present results from two parameter studies, in which wind models with either different coronal-base temperatures or both different coronal-base temperatures and polytropic indices are employed. We show that the flow energetics affect the angular-momentum-loss rate of late-type stars and new torque formulae are presented, which quantify this effect over a wide range of wind acceleration profiles.

1.5 Thesis Overview

In the following chapter (§2), we introduce the formulation of stellar winds driven by thermal pressure, in the frameworks of both hydrodynamics and ideal magnetohydrodynamics. In chapter 3, we present the results from a parameter study, which quantifies how the different coronal-base temperatures and the resulting flow acceleration influence the efficiency of stellar torques. In chapter 4, we generalize the previous findings with a second parameter study, which includes a wider range of flow acceleration profiles by having wind models with both different coronal-base temperatures and flow polytropic indices. Furthermore, in this chapter, we discuss how numerical effects can influence the accuracy of our braking laws, since this study is carried out with a more numerically accurate scheme.

Finally in chapter 5, we summarize the main results and discuss the future perspectives of this work.

Chapter 2

Theory of Thermally Driven Stellar Winds

In this chapter, we introduce the formulation of one-dimensional thermally-driven (or Parker's) winds in the framework of hydrodynamics and ideal magnetohydrodynamics for winds interacting with a rotating magnetic field. For our studies, we consider multidimensional Parker-like winds modified with rotation and magnetic fields. Therefore understanding the structure and limitations of Parker-type wind solutions, even in the context of one-dimensional wind theory, is important for our work. In the following section (§2.1), we derive the isothermal solar wind model. In section 2.2 we present the formulation of polytropic, hydrodynamic wind models. Next, we discuss the effect of rotation and magnetic fields in wind theory (§2.3). In section 2.3.1, we introduce the basic equations of the Weber-Davis model. Our simulation parameter studies only include slow rotators. However, for completeness, in section 2.3.2, we briefly introduce the magneto-centrifugal mechanism, which provides additional acceleration in stellar outflows. We close this chapter with section 2.3.3, where we briefly present some of the properties of two-dimensional, axisymmetric, ideal MHD flows.

2.1 The Isothermal Solar Wind Model

The isothermal solar-wind model (Parker 1958) is the simplest wind theory, which delivers part of the phenomenology observed in the solar wind and can be generalized for any thermal-pressure-driven (or coronal) stellar outflow. The wind solution obtained from this particular formulation describes a single-species flow that is isothermal, steady (i.e. time-independent), and spherically symmetric.

Parker's model assumes that there are only two forces acting on the ouflowing plasma: the inward directed gravity force and the outward directed gradient of thermal pressure force. The equations of mass continuity for a plasma having mass density ρ and velocity vetcor $\boldsymbol{\upsilon}$ is given by

$$\nabla \cdot (\rho \boldsymbol{\upsilon}) = 0, \tag{2.1}$$

which can be written in its integrated form as

$$\rho \upsilon_r r^2 = \text{const.} \equiv f_m, \tag{2.2}$$

where υ_r is the flow radial velocity. The equation of momentum (or motion) for a one-dimensional flow is written as

$$\upsilon_r \frac{d\upsilon_r}{dr} = -\frac{1}{\rho}\frac{dp}{dr} - \frac{GM_*}{r^2}, \tag{2.3}$$

where G is the Newton's gravitational constant, M_* is the stellar mass, and r is the radial distance from the center of the star. p is the thermal pressure of the gas, which is given by the equation of state for an ideal gas

$$p = \frac{\rho k_B T}{\mu m_p}, \tag{2.4}$$

where T is the gas temperature, k_B is the Boltzmann constant, μ is the mean atomic weight, and m_p is the proton mass.

Then equations (2.2), (2.3), and (2.4) can be combined to yield

$$\frac{1}{\upsilon_r}\frac{d\upsilon_r}{dr} = \frac{\frac{2c_{s,iso}^2}{r} - \frac{GM_*}{r^2}}{\upsilon_r^2 - c_{s,iso}^2}, \tag{2.5}$$

where $c_{s,iso}$ is the isothermal sound speed and is given by

$$c_{s,iso}^2 = \frac{p}{\rho}. \tag{2.6}$$

Equation (2.5) exhibits a singularity or in other words possesses a critical point when $\upsilon_r = c_{s,iso}$, since the derivative $d\upsilon_r/dr$ cannot be defined. In order to have wind solutions in which the velocity gradient will be finite at the critical point, both the numerator and denominator of equation (2.5) must be zero. Therefore, solutions that go through the critical point, require

$$\upsilon_r(r_c) = c_{s,iso} \quad \text{at} \quad r_c = \frac{GM_*}{2c_{s,iso}^2}, \tag{2.7}$$

where r_c is the critical distance (i.e. the radial distance of the sonic point from the stellar surface). Analytic integration of equation (2.5) provides the outflow velocity profile, $\upsilon_r(r)$, which depends implicitly on the radial distance, r, as

$$\frac{\upsilon_r}{c_{s,iso}} = \left\{4\frac{r_c}{r} + C + 2\ln\left[\left(\frac{r_c}{r}\right)^2\left(\frac{\upsilon_r}{c_{s,iso}}\right)\right]\right\}^{1/2}, \tag{2.8}$$

where C is just the integration constant and its value determines the type (or behavior) of each wind solution obtained from equation (2.8). In figure 2.1 the topology of the families of wind solutions, for different values of the constant C, is presented. Each type of the solution, shown in figure 2.1, describes different sets of boundary conditions at the base of the flow (i.e., stellar surface) and at infinity. Solutions plotted with black curves are not physical, because they decribe outflows that they either possess supersonic or subsonic speeds everywhere or they are double valued and they do not connect the base of the flow with regions far from the star. Such flow behaviors are not observed in the solar wind (for a more detailed analysis on the topolgy of the solutions, see e.g., Lamers and Cassinelli 1999; Priest 2014). We are interested in solutions that are transonic, meaning that they

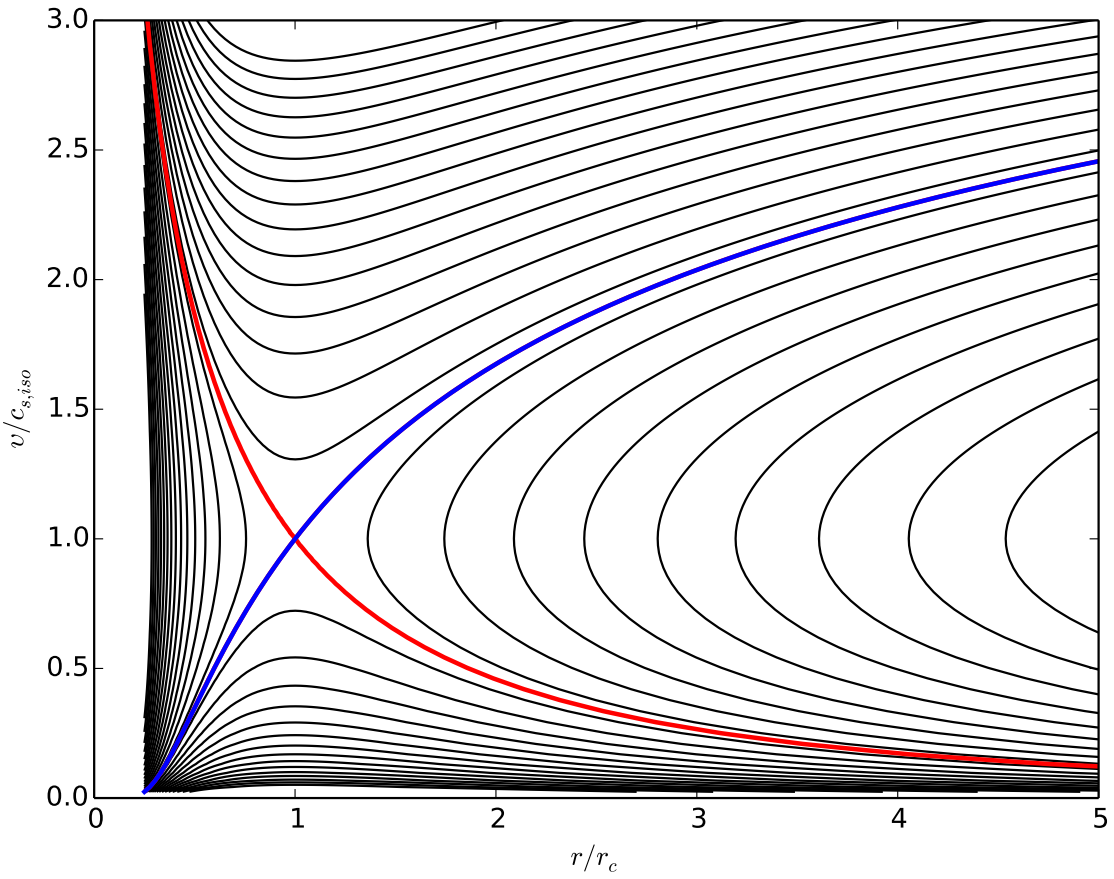

Figure 2.1: The different types of wind solutions of the Parker's isothermal solar wind model. Wind solutions depicted by the black and red curves are unacceptable, since they exhibit phenomenology that is not observed in the solar wind. There is only one physical and transonic solution, depicted by the blue curve. The flow starts out subsonically, reaches the speed of sound, $c_{s,iso}$, at the critical radius, r_c, and becomes supersonic above r_c.

pass through the critical point. There are two transonic (or critical) wind solutions which correspond to $C = -3$. This value of constant C can be obtained by applying condition (2.7) in equation (2.8). The wind solution depicted by the red curve in figure 2.1 is not acceptable because the flow exhibits supersonic velocities at the stellar surface. Solar wind observations suggest that the solar wind is higly subsonic close to the sun and eventually reaches the speed of sound and becomes supersonic farther outwards (see e.g., McComas et al. 2007; Priest 2014). Therefore, the only acceptable wind solution is the blue curve in figure 2.1 because it depicts a flow that has a posivite gradient of v_r. This transonic velocity law describes an outflow, which is subsonic at the stellar surface, reaches the speed of sound at the sonic point, r_c, and becomes supersonic above this radius.

For a given set of boundary conditions at the stellar surface the isothermal wind

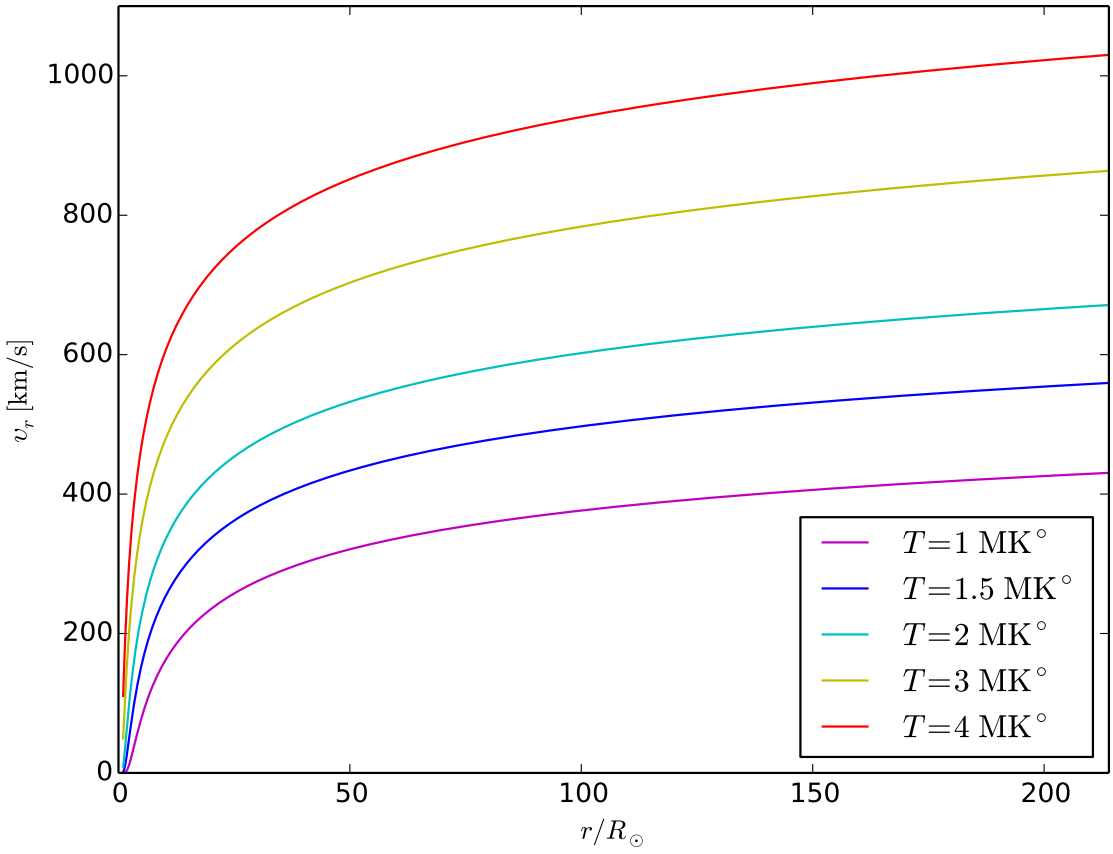

Figure 2.2: Velocity laws of Parker's isothermal solar wind solutions. Each profile corresponds to a different temperature. A higher coronal/flow temperature results in a wind that exhibits a higher base speed, accelerates faster, and reaches a higher terminal velocity. The value of $\sim 214 R_\odot$ on x-axis, where $R_\odot$ is the solar radius, is about 1AU.

model can predict the observed speeds of the solar wind at Earth's orbit. Using the ideal gas equation of state (see equation 2.4), the solar coronal temperature can be written in terms of the parameter $c_{s,iso}/v_{esc}$, which is the ratio of the isothermal sound speed to the escape speed from the solar surafce, $v_{esc} = \sqrt{2GM_\odot/R_\odot}$, where $M_\odot$, $R_\odot$ are the solar mass and radius respectively. Using this approach, one does not have to adopt a specific value for the surface mass density, which varies between solar coronal holes and active regions (e.g., Feldman et al. 2005). The solar coronal temperature is given by

$$T_\odot = \left(\frac{c_s}{v_{esc}}\right)^2 \left(\frac{2GM_\odot \tilde{\mu} m_p}{R_\odot k_B}\right). \tag{2.9}$$

Furthermore,for a given value of c_s/v_{esc}, the above formulation can be used for any solar-type star with known stellar parameters M_*, R_*, and μ. In figure 2.2, solar wind velocity profiles for different coronal temperatures are shown. For this demonstration, the following solar parameters are adopted: $M_\odot = 1.99 \times 10^{33}$ g, $R_\odot = 6.96 \times 10^{10}$ cm, and for a solar coronal plasma $\mu = 0.6$ (e.g., Priest 2014). From figure 2.2 it is clear that higher coronal temperatures produce wind solutions that are faster everywhere. Studies have shown that the Parker's isothermal wind model can predict the velocity profile of the slow solar wind, with terminal speeds of $\sim$ 400 km s^{-1}, (see e.g., Ofman 2004), but require unrealistic coronal temperatures to reproduce the fast wind, with speeds at Earth's orbit of $\sim$ 800 km s^{-1}. Specifically, observations (see e.g., Feldman et al. 2005; Cranmer et al. 2017) show that the fast wind emanates from polar coronal holes with electron temperatures of $\sim$ 1 MK°, while figure 2.2 shows that such flow speeds can be achieved by an expanding isothermal stellar atmosphere only when its temperature is above 2.5 MK°. Another difficulty with Parker's theory is that it delivers solutions with infinite speeds at infinity and therefore requires an infinite energy input in order the flow to be kept isothermal.

2.2 The Polytropic Wind Model

In the polytropic wind model (e.g., Parker 1963; Keppens and Goedbloed 1999; Lamers and Cassinelli 1999; Priest 2014), a polytropic relation between the temperature of the flow and the mass density is employed. The isothermal assumption is dropped and the flow temperature will now vary spatially. The polytropic relations between the temperature

and the mass density or the thermal pressure and the mass density are given, respectively, by

$$T(r) \propto \rho(r)^{\gamma-1} \quad \text{or} \quad p(r) \propto \rho(r)^{\gamma}, \tag{2.10}$$

where γ is the polytropic index, defined as the ratio of specific heats

$$\gamma \equiv \frac{c_p}{c_v}, \tag{2.11}$$

where c_p, c_v have their usual meaning. Therefore the temperature structure is determined by the value of γ.

At this point it is useful to introduce the specific enthalpy of an ideal gas for polytopic processes, which is the sum of the gas specific internal energy plus the work done by the gas through an adiabatic expansion (i.e., constant entropy or no heat transfer),

$$h = u + pV = u + \frac{p}{\rho} = \frac{\gamma}{\gamma - 1}\frac{p}{\rho}, \tag{2.12}$$

where u is the specific internal energy of the gas and V the specific volume (i.e., $V = \rho^{-1}$). For a mono-atomic gas (i.e., gas composed of neutral atoms, ions and electrons), $u = 3k_BT/(2\mu m_p)$, $\gamma = 5/3$, and thus, $h = 5k_BT/(2\mu m_p)$. In stellar-wind theory, any polytropic relation with a value of γ less than 5/3 has the effect of implicit heating in the momentum equation of the flow. In other words, the polytropic approximation mimics an expanding stellar atmosphere with $\gamma = 5/3$ but with extended coronal heating, resulting in a temperature profile $T(r) \propto \rho(r)^{\gamma-1}$. Furthermore, the exact value of the polytropic index in equation (2.10) specifies the "energy input" in the flow (see also equation (2.16) below). A small value of γ (approaching the value of 5/3) corresponds to a large energy deposition in the wind (e.g., $\gamma = 1$ is the isothermal case), while a large value of γ corresponds to a small one, since the flow temperature decays faster with distance as the gas expands. In principle, the polytropic index can vary between $1 \leq \gamma \leq 5/3$. The extreme case of $\gamma = 5/3$ is not of interest, since this polytrope corresponds to a zero energy input in the wind (i.e., adiabatic expansion). Wind solutions with γ taken to be between 5/3 and 3/2 are transonic but they are not acceptable. Such flows are supersonic at the

stellar surface and their speed decrease outwards. Cases with $\gamma = 3/2$ exhibit a contant speed. Therefore, acceptable polytropic wind solutions have $\gamma < 3/2$. Such solutions are transonic and their velocity profiles increase monotonically with radial distance. In the literature, typical values of the polytropic index that have been used in solar or stellar wind studies are in the range $1 < \gamma < 1.15$ (e.g., Parker 1963; Kopp and Holzer 1976; Steinolfson et al. 1982; Washimi and Shibata 1993; Washimi and Sakurai 1993; Keppens and Goedbloed 1999; Mikić et al. 1999; Vidotto et al. 2014a).

The mass continuity and momentum equations, assuming sperical symmetry and steady state, have the same form for a hydrodynamic and polytropic wind as in the case of the isothermal model (see equations (2.2) and (2.3)). Therefore, the momentum equation can be written as

$$\frac{1}{v_r}\frac{dv_r}{dr} = \frac{\frac{2c_s^2}{r} - \frac{GM_*}{r^2}}{v_r^2 - c_s^2}, \tag{2.13}$$

where c_s is the adiabatic speed of sound, given now as

$$c_s^2 = \frac{\gamma p}{\rho} \tag{2.14}$$

The critical solution again requires us to impose the numerator and denominator on the RHS of equation (2.13) to be zero. Thus the condition for a transonic velocity law is

$$v(r_c) = c_s(r_c) \quad \text{and} \quad r_c = \frac{GM_*}{2c_s^2(r_c)}. \tag{2.15}$$

The adiabatic sound speed is not constant, but varies with the radial distance, r. Therefore, the momentum equation (2.13) cannot be directly integrated to provide an analytic solution, which gives the wind velocity law. Now, integration of the momentum equation gives the Bernoulli function, which is a constant of motion for a steady-state flow. The Bernoulli function or energy constant gives the specific energy input in the wind, and is given as

$$\epsilon = \frac{v^2}{2} + \frac{\gamma}{\gamma - 1}\frac{p}{\rho} - \frac{GM_*}{r} = \text{const.} \tag{2.16}$$

Equation (2.16) comprises the flow specific kinetic energy, enthalpy, and potential energy. Evaluating equation (2.16) at infinity, the potential energy goes to zero, the term $(p/\rho)_\infty$ also goes to zero, and hence, the specific kinetic energy dominates, $\epsilon = v_\infty^2/2 > 0$. In other words, the Bernoulli function is a positive quantity for any flow that escapes the stellar gravitational potential. Lastly, equation (2.16) can now explain the fact that polytropic models with $\gamma = 3/2$ exhibit a constant speed. In this special case of a polytropic flow, we have $v = \text{const.}$ and therefore, $v^2/2 = v_\infty^2/2 = \epsilon$. The latter implies that the values of the specific enthalpy and potential energy, $\gamma p/((\gamma-1)\rho)$ and GM_*/r, respectively, must be equal at any radial distance. As a consequence, the ratio p/ρ scales with radius as r^{-1}. Using the polytropic relation between thermal pressure and density (i.e., $p \propto \rho^\gamma$), one gets $\rho \propto r^{\frac{1}{1-\gamma}}$. The mass continuity equation (2.2) gives $\rho \propto r^{-2}$, for a flow propagating at constant speed. Therefore a value of $\gamma = 3/2$ is required, in order these two conditions for density to be satisfied.

Equations (2.2), (2.10), (2.14). and (2.16) can be combined to yield the location of the critical distance, r_c, the distance at which a polytropic wind reaches the sound speed. We get

$$\frac{R_*}{r_c} = \frac{\gamma-1}{5-3\gamma}\left[\frac{2c_{s,*}}{v_{esc,*}}\right]^{\frac{4}{1-\gamma}}\left[\frac{R_*}{r_c}\right]^{\frac{5-3\gamma}{\gamma-1}} + \frac{2}{5-3\gamma}\left[\frac{2c_{s,*}}{v_{esc,*}}\right]^2 - \frac{4(\gamma-1)}{5-3\gamma}, \tag{2.17}$$

where R_* is the stellar radius, $c_{s,*}$ and $v_{esc,*}$ are the sound speed and the escape speed at the surface of the star, respectively. Equation (2.17) can be solved numerically, for a given value of $c_{s,*}/v_{esc,*}$ and γ to yield the critical radius, r_c/R_*, of a polytropic flow.

The velocity profile of a polytropic wind can be derived from the Bernoulli function (2.16), (e.g., Lamers and Cassinelli 1999). By introducing the dimensionless parmeters.

$$x = \frac{r}{r_c} \quad \text{and} \quad w = \frac{v}{v(r_c)} = \frac{v}{v_c}, \tag{2.18}$$

where v_c is the wind speed at r_c, given by equation (2.15), w can be written in terms of x in the following implicit form,

$$w^{\gamma+1} - w^{\gamma-1}\left[\frac{4}{x} + \frac{5-3\gamma}{\gamma-1}\right] + \frac{2}{\gamma-1}x^{2-2\gamma} = 0. \tag{2.19}$$

Equation (2.19), combined with equation (2.17), can be solved numerically for w and x and provides the wind velocity profile $\upsilon(r)$, for a given value of $c_{s,*}/\upsilon_{esc,*}$ and γ. Determining the sonic point, r_c, from equation (2.17) and the flow velocity law from equation (2.19), the following relation (see also Keppens and Goedbloed 1999) should be satisfied by a polytropic wind solution

$$\frac{r_c}{R_*} = \left(\frac{\upsilon_{esc,*}}{2c_{s,*}}\right)^{\frac{2(\gamma+1)}{5-3\gamma}} \left(\frac{c_{s,*}}{\upsilon_{r,*}}\right)^{\frac{2(\gamma-1)}{5-3\gamma}}, \tag{2.20}$$

where $\upsilon_{r,*}$ is the radial velocity at R_* (i.e., base of the flow).

Similar to the isothermal case, the velocity profiles of polytropic winds depend on the lower boundary conditions normally specified at the lower boundary (i.e., base density and temperature) and the value of γ, which determines the energy deposition in the flow (see e.g., Lamers and Cassinelli 1999).

The polytropic wind model is an improvement to the isothermal one, because it includes spatial variations in the flow temperature. Furthermore, within the polytropic approximation the wind can still expand supersonically, reaching realistic terminal speeds, but now this is achieved by injecting finite energy in the flow. For example, studies showed that a value of γ of 1.05 or 1.1 can reproduce the large-scale properties of the solar wind, meaning that a polytropic relation can approximate the extended coronal heating (e.g., Keppens and Goedbloed 1999; Priest 2014). However, the polytropic model, for realistic solar coronal conditions and a fixed value of γ, still fails to produce the fast solar-wind component with a temperature as low as observed. However, more advanced polytropic models, employing a varying polytropic index with radial distance, can reproduce the observed solar wind (e.g., Cohen et al. 2007; Jacobs and Poedts 2011).

2.3 Theory of Magnetic Rotators

The interactions between the large-scale solar/stellar magnetic field and an outflow had been discussed in several early works (see e.g. Schatzman 1962; Parker 1958, 1963; Pneuman 1966). Weber and Davis (1967) studied the influence of a rotating magnetic field on the Sun and established the concept of magnetic-rotator theory.

2.3.1 The Weber-Davis Model

The Weber-Davis model provides solutions with flow and field components in the equatorial plane [1]. For an equatorial wind, assuming North-South symmetry and axisymmetry (i.e., the vector fields have no dependence on the ϕ coordinate), the magnetic and velocity vectors depend on the radial distance, r, alone and are written as

$$\boldsymbol{B} = B_r(r)\hat{\boldsymbol{r}} + B_\phi(r)\hat{\boldsymbol{\phi}}, \tag{2.21}$$

$$\boldsymbol{v} = v_r(r)\hat{\boldsymbol{r}} + v_\phi(r)\hat{\boldsymbol{\phi}}, \tag{2.22}$$

where $\hat{\boldsymbol{r}}$ and $\hat{\boldsymbol{\phi}}$ are the unit vectors for the radial and azimuthal direction, respectively. Under the assumption of ideal MHD (i.e. infinite conductivity) and steady state, the governing flow equations are the mass continuity equation (2.2), plus the momentum and induction equation given, respectively, by

$$\rho(\boldsymbol{v}\cdot\nabla)\boldsymbol{v} = -\nabla\left(p + \frac{\boldsymbol{B}^2}{8\pi}\right) + \frac{(\boldsymbol{B}\cdot\nabla)\boldsymbol{B}}{4\pi} - \frac{GM_*\rho}{r^2}\hat{\boldsymbol{r}}, \tag{2.23}$$

$$\nabla\times(\boldsymbol{v}\times\boldsymbol{B}) = 0. \tag{2.24}$$

The flow is also taken to obey a polytropic law (2.10) and an ideal gas equation of state (2.4).

Integration of the induction equation (2.24) yields

$$r(v_r B_\phi - v_\phi B_r) = \mathrm{C}, \tag{2.25}$$

where C is the integration constant. The value of C can be evaluated under the following

1. The Weber-Davis model is restricted to axisymmetric, equatorial flows. Yeh (1976) showed that the Weber-Davis wind solution, for a prescribed field geometry, is also valid in regions outside the equator by solving the ideal MHD equations along each field line independently. Sakurai (1985) generalized the Weber-Davis model in two dimensions, still using a split-monopole field geometry. He found that this self-consistent treatment of the structure of the poloidal magnetic field, produces collimated wind solutions (due to a gradient of the magnetic pressure force of B_ϕ) for both slow and fast magnetic rotators. In our simulations (shown in the following chapters), the deflection of the field lines towards the axis of rotation is not obvious, due to the limited size of the computational domain on r coordinate.

approximations. The tangential velocity at the stellar surface, R_*, is $\upsilon_{\phi,*} \simeq \Omega R_*$, where Ω is the stellar angular speed. The flow base (or stellar-surface) radial velocity is small and therefore, $\upsilon_{r,*} \ll \upsilon_{\phi,*}$, where the "*" denotes values at R_*. The field lines are almost radial at the stellar surface, which gives $B_{\phi,*} \ll B_{r,*}$. Thus, $\upsilon_{r,*}B_{\phi,*} \ll \upsilon_{\phi,*}B_{r,*}$ and $\mathrm{C} = -R_*^2 \Omega B_{r,*}$. Maxwell's equation $\nabla \cdot \boldsymbol{B} = 0$, in spherical coordinates and in spherical symmetry, gives

$$r^2 B_r = \text{const.} = R_*^2 B_{r,*} \equiv f_B. \tag{2.26}$$

Equations (2.25) and (2.26) can be combined to provide the ratio of B_ϕ to B_r as a function of r

$$\frac{B_\phi}{B_r} = \frac{\upsilon_\phi - \Omega r}{\upsilon_r}. \tag{2.27}$$

The ϕ-component of the momentum equation (2.23) is

$$\rho \upsilon_r \frac{d}{dr}(r\upsilon_\phi) = \frac{B_r}{4\pi}\frac{d}{dr}(rB_\phi), \tag{2.28}$$

where the quantity $\rho\upsilon_r/B_r$ is constant ($= f_m/f_B$) as a consequence from equations (2.2) and (2.26). Therefore, integration of equation (2.28) gives

$$r\upsilon_\phi - \frac{rB_rB_\phi}{4\pi\rho\upsilon_r} = \text{const.} = L. \tag{2.29}$$

In the above expression, L is a constant of motion, which measures the total specific angular momentum carried away by the magnetized wind. Both terms in equation (2.29) are positive quantities and represent the angular momentum carried in the gas (first term) and the magnetic stresses (second term).

Substituting B_ϕ, given from equation (2.27), in equation (2.29) gives

$$\upsilon_\phi = \Omega r \frac{M_A^2 L/(\Omega r^2) - 1}{M_A^2 - 1}, \tag{2.30}$$

where M_A is the Alfvénic Mach number, defined as the ratio of the radial wind speed to

the radial Alfvén speed, υ_A,

$$M_A = \frac{\upsilon_r}{\upsilon_A} \equiv \frac{\upsilon_r}{B_r/(4\pi\rho)^{1/2}}. \tag{2.31}$$

Equation (2.30) possesses a critical point at $M_A = 1$, when the flow speed, υ_r reaches the local υ_A. This is the Alfvén critical point and occurs at $r = R_A$, where R_A is the wind's Alfvén radius. The wind's tangential speed, υ_ϕ, must be finite in equation (2.30) and therefore, both the numerator and denominator should vanish at R_A.

By setting the numerator of equation (2.30) equal to zero we get

$$L = \Omega R_A^2. \tag{2.32}$$

Equation (2.32) gives the amount of the total angular momentum per mass carried off by the magnetized wind and demonstrates a mechanical equivalent of rigid-body rotation out to the Alfvén radius. In other words, it is as if within R_A, the magnetic stresses force the flow to strictly co-rotate with the star, increasing plasma's angular momentum and the efficiency of angular-momentum loss, and above R_A, the flow conserves its angular momentum. Therefore, the wind Alfvén radius, R_A, represents the mechanical analog of a lever arm, which brakes the stellar rotation. In reality, the wind always sub-rotates at any radial distance from the surface of the stars and υ_ϕ is a well-behaved function of r, which goes smoothly through R_A (see for example discussion in Weber and Davis 1967), but the total specific angular momentum carried by the flow is always equal to ΩR_A^2. The total angular-momentum-loss rate carried away by a spherically symmetric stellar wind (see e.g., Weber and Davis 1967; Belcher and MacGregor 1976) can be written as

$$\tau_w = \frac{dJ}{dt} = \frac{2}{3}\dot{M}_w \Omega_* R_*^2 \left(\frac{R_A}{R_*}\right)^2, \tag{2.33}$$

where the ratio 2/3 comes from the dependence of the torque on the cylindrical radius (i.e., distance from the rotation axis), not the spherical radius. The normalized term R_A/R_* has the meaning of a normalized "lever-arm length" and its exact value determines the amount of the stellar angular momentum loss per time or in other words the efficiency of the torque exerted on the star. Pizzo et al. (1983) used observation from Helios spacecraft

to calculate the location of the solar-wind Alfvén radius. They found that this distance is about $r \approx 12R_\odot$. Later studies suggest that the Alfvén point is located at different radial distances in fast and slow solar-wind streams, giving as minimum values, $12R_\odot$ and $15R_\odot$, for coronal-hole and equatorial-belt streamers, respectively (DeForest et al. 2014).

The radial component of the momentum equation (2.23) is

$$\rho v_r \frac{dv_r}{dr} - \frac{\rho v_\phi^2}{r} = -\frac{dp}{dr} - \frac{B_\phi}{4\pi r}\frac{d}{dr}(rB_\phi) - \frac{GM_*\rho}{r^2}. \tag{2.34}$$

By substituting the expressions for p, ρ, B_ϕ, and v_ϕ (see equations (2.4), (2.10) (2.27), and (2.30), respectively) in the differential equation (2.34), one gets the topology of the solutions in the Weber-Davis wind formulation. In our multidimensional wind simulations (presented in the following chapters), the flow velocity (and in general all the flow variables, i.e. mass density, thermal pressure, magnetic field components, etc.) are computed numerically by the PLUTO code. Therefore, a demonstration of the solution method of equation (2.34) is out of the scope of this introductory chapter due to its long derivation and the complexity that it introduces. However, detailed analysis on the methodology required to solve equation (2.34) and/or the type of the wind solutions obtained from the Weber-Davis model can be found in the original works by Weber and Davis (1967), Hartmann and MacGregor (1982), Johnstone (2017), the review by Sakurai (1990), and the textbooks by Brandt (1970), Heyvaerts (1996), Lamers and Cassinelli (1999), and Priest (2014). In short, physical wind solutions in the Weber-Davis model exhibit different topology compared to the hydrodynamic wind solutions, discussed in the previous sections. The velocity profiles of the Weber-Davis solutions are still transonic and increase monotonically with radial distance, but pass now through three critical points, which represent the distances at which the flow reaches the characteristic speeds of the slow magnetosonic, Alfvén, and fast magnetosonic wave.

Weber and Davis (1967) computed the angular-momentum-loss rate of the Sun due to its magnetized solar wind (see also Parker 1958) and concluded that the time-scale for the Sun to lose its entire angular momentum (assuming a constant torque) is comparable with its main-sequence lifetime ($\sim 10^{10}$ years). In contrast, the solar mass-loss rate is of

the order of $10^{-14}\ M_{\odot}\mathrm{yr}^{-1}$ and therefore, the solar wind is not anticipated to significantly influence Sun's structural evolution.

2.3.2 The Slow and Fast Magnetic Rotator Regime

The radial component of the momentum (2.34) can be integrated to provide the energy constant

$$\epsilon = \frac{1}{2}(\upsilon_r^2 + \upsilon_\phi^2) + \frac{\gamma}{\gamma - 1}\frac{p}{\rho} - \frac{GM_*}{r} - \frac{r\Omega B_r B_\phi}{4\pi\rho\upsilon_r} = \text{const.} \tag{2.35}$$

The first three terms in the energy flux equation (2.35) are the plasma's specific kinetic energy, enthalpy and potential energy, and the fourth term is the magnetic component of the energy input in the flow.

Belcher and MacGregor (1976) showed that for stars, which are fast rotators, the term that dominates in the energy equation (2.35) is the magnetic-energy term. Therefore, they introduced two different regimes in stellar-wind theory: a) the slow magnetic rotator (SMR) regime, for which the flow components on the radial direction can be approximated by Parker's theory; and b) the fast magnetic rotator regime (FMR), for which magnetic effects contribute significantly on the wind acceleration. The FMR regime occurs when the wind terminal speed approaches the Michel velocity (Michel 1969), which is

$$V_M = \left(\frac{\Omega^2 f_B^2}{4\pi f_m}\right)^{1/3}. \tag{2.36}$$

From Parker's theory, the wind speed at infinity, V_P, can be obtained from the energy constant (2.16) and is given as

$$\frac{1}{2}V_P^2 = \frac{c_{s,*}^2}{\gamma - 1} - \frac{1}{2}V_{esc,*}^2 + \frac{1}{2}V_{r,*}^2, \tag{2.37}$$

where $c_{s,*}$, $V_{esc,*}$, $V_{r,*}$ are the sound, escape, and flow speed at the lower boundary. Belcher and MacGregor (1976) pointed out that for SMR, $V_M \ll V_P$, and for FMR, $V_M \gg V_P$. They calculated the Michel velcocity for the current Sun and found to be $\sim 60 - 90$ km s^{-1} $\ll 500$ km s^{-1}, which is approximately the average solar wind speed at Earth's orbit. Thus, the Sun was identified as a SMR. Lastly, they demonstrated that magneto-

centrifugal acceleration increases the flow terminal speed and changes the location of the Alfvén and fast-magnetosonic-wave point in the wind. Stars, which are fast rotators, have their Alfvén point closer to the star and the fast-magnetosonic-wave wave point further outwards. Later studies demonstrated that, for multidimensional flows, magneto-centrifugal effects do not only influence the wind terminal speed, but further affect the poloidal stucture of the flow by generating collimated jet-type wind solutions (e.g., Sakurai 1985; Washimi and Shibata 1993).

2.3.3 Theory of Stationary, Axisymmetric, Ideal MHD flows

In this section we present some of the properties of two-dimensional, steady-state, axisymmetric, ideal MHD flows. Under the assumption of axisymmetry the magnetic and velocity vectors can be decomposed in their poloidal and toroidal components. This is

$$\boldsymbol{B} = \boldsymbol{B_p}(r,\theta) + \boldsymbol{B_\phi}(r,\theta), \tag{2.38}$$

$$\boldsymbol{v} = \boldsymbol{v_p}(r,\theta) + \boldsymbol{v_\phi}(r,\theta), \tag{2.39}$$

where

$$\boldsymbol{B_p} = B_r(r,\theta)\hat{\boldsymbol{r}} + B_\theta(r,\theta)\hat{\boldsymbol{\theta}}, \tag{2.40}$$

$$\boldsymbol{v_p} = v_r(r,\theta)\hat{\boldsymbol{r}} + v_\theta(r,\theta)\hat{\boldsymbol{\theta}}. \tag{2.41}$$

Under the assumption of steady state and ideal MHD, the induction equation (2.24) can be integrated to give

$$\boldsymbol{v} \times \boldsymbol{B} = \nabla f, \tag{2.42}$$

where f is a scalar function of r and θ. Due to axisymmetry, ∇f has no toroidal component and therefore,

$$\boldsymbol{v_p} \times \boldsymbol{B_p} = 0, \tag{2.43}$$

which shows that $\boldsymbol{v_p}$ is parallel to $\boldsymbol{B_p}$. Therefore one can write

$$\rho \boldsymbol{v_p} = \alpha \boldsymbol{B_p}, \tag{2.44}$$

where again α is a scalar function of (r, θ). From the mass continuity equation (2.1) we get

$$\nabla \cdot (\rho \boldsymbol{v}) = \nabla \cdot (\alpha \boldsymbol{B}) = \boldsymbol{B} \cdot \nabla \alpha = 0, \tag{2.45}$$

because the magnetic field is divergence free. In other words, the scalar qunatity α, the mass flux per magnetic flux, is a constant of motion along the field lines.

Combining Maxwell's equation, $\nabla \cdot \boldsymbol{B} = 0$, with the ϕ component of the induction equation (2.24), we obtain the second constant of motion along the field lines, which is

$$\Omega = \frac{1}{r \sin\theta} \left(v_\phi - \frac{v_p}{B_p} B_\phi \right) \quad \text{with} \quad \boldsymbol{B} \cdot \nabla \Omega = 0, \tag{2.46}$$

where Ω is the effective rotation of the field lines. The toroidal component of the momentum equation (2.23) gives the third invariant along the field lines, which is the total specific angular momentum, Λ. We get

$$\Lambda = r \sin\theta \left(v_\phi - B_\phi \frac{B_p}{4\pi \rho v_p} \right) \quad \text{with} \quad \boldsymbol{B} \cdot \nabla \Lambda = 0, \tag{2.47}$$

The next constant of motion is the Bernoulli function and can be obtained by projecting the momentum equation (2.23) on the direction of $\boldsymbol{B_p}$. Then one can show that

$$\epsilon = \frac{v^2}{2} + \frac{\gamma}{\gamma - 1} \frac{p}{\rho} - \frac{GM_*}{r} - v_\phi \Omega r \sin\theta \quad \text{with} \quad \boldsymbol{B} \cdot \nabla \epsilon = 0, \tag{2.48}$$

Using the polytropic law (2.10), the last axisymmteric MHD invariant is the specific en-

tropy, $s = p/\rho^{\gamma}$, because $\boldsymbol{v} \cdot \nabla s = 0$ (i.e., no heat flow into or out of a piece gas as it flows on a given magnetic surface). The latter leads to $\boldsymbol{B} \cdot \nabla s = 0$.

In this work, some of the MHD invariants derived here will be used as boundary conditions for our numerical setup. Furthermore, we will use these scalar quantities to examine the accuracy of our simulations. For a more detailed discussion on stationary, axisymmteric, ideal MHD flows we point to the reader to the following references: Mestel (1961, 1968, 1999), Okamoto (1975), Heinemann and Olbert (1978), Lovelace et al. (1986), Sakurai (1990), and Keppens and Goedbloed (2000).

2.4 Summary

In this chapter, we initially presented the formulation of one-dimensional, hydrodyanmic, thermally-driven winds, using the isothermal and polytropic approximation. For our work, we will consider polytropic winds modified with rotation and magnetic fields. A polytropic flow exhibit a temperature profile that varies spatially with radial distance and therefore mimics an expanding stellar atmopsphere with energy addition from coronal heating. Furthermore, the adopted values of the coronal-base temperature and polytropic index determine the energy input in the flow, and thus these two parameters affect the wind acceleration and velocity profiles.

Next, we discussed the interaction of a one-dimensional wind with a rotating magnetic magnetic. We showed that in magnetized winds, magnetic stresses transmit angular momentum from the star to the plasma, even after the flow has left the stellar surface, enhancing the stellar angular momentum loss. The total specific angular momentum carried away by the wind is, $L = \Omega R_A^2$, where Ω is the stellar-surface rotation rate and R_A is the Alfvén point of the flow. The Alfvén radius can be thought of as a lever arm, which slows down the stellar rotation, and its exact value determines the efficiency of the torque exerted on the stellar surface. Then, we disscussed briefly the magneto-centrifugal acceleration mechanism, which provides additional acceleration in winds from stars that are fast rotators. However, in our studies, we consider only slowly rotating stars. The goal in this work is to investigate and quantify how differences in the flow thermodynamics (i.e., coronal temperature and polytropic index, γ, in the polytropic approximation) affect the

magnetic braking of low-mass stars. We closed this chapter by deriving the invariants of 2D, axisymmetric, steady-state, and ideal MHD flows.

Chapter 3

Magnetic Braking of Sun-like and Low-mass Stars: Dependence on Coronal Temperature

This chapter is presented as it was accepted for publication in the Astrophysical Journal. The appendices of Pantolmos and Matt (2017) are now presented as sections in the main text and exist before the conclusions. This chapter includes the parameter study, which shows the effect of the stellar coronal temperature on the magnetic braking of sun-like and low-mass stars.

Sun-like and low-mass stars possess high temperature coronae and lose mass in the form of stellar winds, driven by thermal pressure and complex magnetohydrodynamic processes. These magnetized outflows probably do not significantly affect the star's structural evolution on the Main Sequence, but they brake the stellar rotation by removing angular momentum, a mechanism known as magnetic braking. Previous studies have shown how the braking torque depends on magnetic field strength and geometry, stellar mass and radius, mass-loss rate, and the rotation rate of the star, assuming a fixed coronal temperature. For this study we explore how different coronal temperatures can influence the stellar torque. We employ 2.5D, axisymmetric, magnetohydrodynamic simulations, computed with the PLUTO code, to obtain steady-state wind solutions from rotating stars

with dipolar magnetic fields. Our parameter study includes 30 simulations with variations in coronal temperature and surface-magnetic-field strength. We consider a Parker-like (i.e., thermal-pressure-driven) wind, and therefore coronal temperature is the key parameter determining the velocity and acceleration profile of the flow. Since the mass loss rates for these types of stars are not well constrained, we determine how torque scales for a vast range of stellar mass loss rates. Hotter winds lead to a faster acceleration, and we show that (for a given magnetic field strength and mass-loss rate) a hotter outflow leads to a weaker torque on the star. We derive new predictive torque formulae for each temperature, which quantifies this effect over a range of possible wind acceleration profiles.

3.1 Introduction

Stellar winds are a very common phenomenon in our universe. For Sun-like and low-mass stars ($M_* \lesssim 1.3 M_\odot$), such outflows are usually in the form of coronal winds (Parker 1958, 1963), due to their origin in the several MK stellar hot coronae. Although the effect of coronal winds on stellar mass during a star's Main-Sequence (MS) life is relatively small, they can influence the environment of surrounding planets (e.g., Lüftinger et al. 2015), and have an enormous impact on stellar rotation by exerting a spin-down torque on the stellar surface (e.g., Schatzman 1962; Weber and Davis 1967). Hence, over the years the angular momentum (or rotational) evolution of cool stars has been the subject of very intensive studies (for a review see Bouvier et al. 2014).

The spin-down of MS cool stars was established observationally from early studies (Kraft 1967; Skumanich 1972) that showed the rotation periods of these types of stars to increase as the stellar age advances. The current picture of the rotational evolution of cool stars is more complicated, and observations (e.g., Barnes 2003, 2010; Irwin and Bouvier 2009; Meibom et al. 2011; Meibom et al. 2015) show that stellar rotation depends on both the mass and age. In addition, the observed trends between magnetic activity (or coronal X-ray emission) and stellar rotation (e.g., Pizzolato et al. 2003; Wright et al. 2011), and the observed evolution of stellar magnetic properties (e.g., Vidotto et al. 2014a; See et al. 2015) suggest that solar- and late-type stars lose mass and angular momentum in the form of magnetized outflows.

Coronal-wind modeling has a long history in the literature, with the use of analytic theory (e.g., Parker 1958; Weber and Davis 1967; Mestel 1968; Heinemann and Olbert 1978; Low and Tsinganos 1986), or iterative methods/numerical simulations (e.g., Pneuman and Kopp 1971; Sakurai 1985; Washimi and Shibata 1993; Keppens and Goedbloed 2000; Cohen et al. 2007; Vidotto et al. 2009). The main source for understanding the nature, the properties and the dynamics of coronal winds comes from direct observations of the solar wind. The solar corona expands into the interplanetary space in the form of a supersonic, magnetized wind that evolves during a solar cycle. Near the solar minimum the solar wind is bimodal with a fast, tenuous, and steady, component emanating from large polar coronal holes and a slower, denser and filamentary component emerging from the top of the helmet streamers originated at the magnetic activity belt (e.g., McComas et al. 2007; McComas et al. 2008). During the solar maximum the solar wind becomes more variable and is more dominated by the slow wind at all latidtudes (e.g., McComas et al. 2003; McComas et al. 2007). The solar wind is a direct consequence of the hot solar corona (with $T > 10^6 K$) and thus the solar-plasma acceleration (for both the fast and slow solar wind) is connected to the coronal heating problem (e.g., De Moortel and Browning 2015). The physical mechanisms responsible for the solar-corona heating are still in debate, but they all require magnetic fields as a key ingredient (see, e.g., Aschwanden 2005; Klimchuk 2015; Velli et al. 2015). The solar magnetic field (a product of the solar dynamo that operates within the convection zone) threads the solar photosphere, expands throughout the solar atmosphere and eventually connects with and energizes the solar wind. The recent advances in solar-wind theory include wave dissipation (via turbulence) and magnetic reconnection as heat sources for the expanding outer solar atmosphere (see, e.g., Ofman 2010; Cranmer 2012; Cranmer et al. 2015; Hansteen and Velli 2012). Scaling-law models (e.g., Wang and Sheeley 1991; Fisk 2003; Schwadron and McComas 2003, 2008) reproduce part of the observed characteristics of the solar wind, although, that approach does not treat the coronal heating/solar-wind acceleration problem in a self-consistent way (see, e.g., Hansteen and Velli 2012). A conclusive answer on what heats the solar corona and what are the physical processes that drive the solar wind does not yet exist. X-ray observations reveal the existence of hot outer atmospheres in low-mass star (e.g., Wright et al. 2011). However, it is still not well understood how coronal heating should vary

among late-type stars with varying masses and rotation rates, and its connection with the observed trends in X-ray emission (see, e.g., Testa et al. 2015). Therefore, it is still an open question of how to apply our knowledge of the solar coronal heating and wind acceleration to other stars. The present work is concerned with characterizing the global torques on stars and how they scale for a variety of stellar properties, while solutions to the coronal-heating problem remain uncertain. Consequently, in this work, we treat many of the coronal processes as "free parameters", including the wind mass loss rates and wind acceleration profiles, which show how the uncertainties in our understanding of stellar coronae will influence our ability to predict angular momentum loss.

In the framework of stellar-torque theory, early works (e.g., Schatzman 1962; Mestel 1984; Mestel and Spruit 1987; Kawaler 1988) have provided analytic prescriptions for the magnetic braking of cool stars, and some more recent works compute the stellar angular momentum losses self-consistently, via multidimensional numerical simulations. For example, studies have quantified how the magnetic braking scales with various stellar parameters (e.g., Matt and Pudritz 2008; Matt et al. 2012a; Cohen and Drake 2014), and others have showed how stellar angular momentum losses depends on different magnetic field geometries (e.g., Garraffo et al. 2015, 2016; Réville et al. 2015a; Finley and Matt 2017). With the new advances in Zeeman-Doppler Imaging (e.g., Donati and Brown 1997; Donati and Landstreet 2009), observers can now extract stellar-surface magnetic field maps that can be used in order to reconstruct the stellar field near the star. Some studies (e.g., Vidotto et al. 2014b; Alvarado-Gómez et al. 2016; Réville et al. 2016a), have used such maps in their wind simulations, in order to provide trends for stellar torques based on realsitic magnetic fields. In general, accurate stellar-torque predictions are one of the critical ingredients for rotational evolution models (e.g., Reiners and Mohanty 2012; Gallet and Bouvier 2013; 2015; Johnstone et al. 2015a; Matt et al. 2015; Amard et al. 2016, See et al. submitted).

Coronal temperatures among MS cool stars significantly vary (e.g., Johnstone et al. 2015b). However, there has not yet been a systematic study of magnetic braking that investigates the key parameters (i.e., stellar coronal temperature and polytropic index), that affect the wind driving (or flow acceleration and velocity). The objective of this study

is to quantify the influence of different flow temperatures on stellar torques. We adopt the approach introduced in Matt and Pudritz (2008). In particular, Matt and Pudritz (2008) found that the effective magnetic lever arm (or Alfvén radius), that determines the efficiency of the braking torque, is a power law in a parmeter Υ (i.e., wind magnetization), that depends on the stellar mass, radius, mass-loss rate, and magnetic field strength. Studies on massive, hot stars (e.g., type O stars, see Ud-Doula et al. 2009), have found similar scalings between the stellar parameters and angular momentum losses, with the main difference being that the wind-driving mechanism is fundamentally different (e.g., Lamers and Cassinelli 1999; Owocki 2009b). Following Matt and Pudritz (2008), a series of studies (Matt et al. 2012a; Réville et al. 2015a; Réville et al. 2016a; Finley and Matt 2017), expanded the previous torque formulation in braking laws that include the dependence of the braking torque on the stellar spin rate and different magnetic field geometries. All these studies (Matt and Pudritz 2008; Matt et al. 2012a; Réville et al. 2015a; Réville et al. 2016a; Finley and Matt 2017) used polytropic, Parker wind models (e.g., Parker 1963; Keppens and Goedbloed 1999; Lamers and Cassinelli 1999), modified by rotation and magnetic fields. However, they kept fixed the flow thermodynamics (i.e., coronal temperature and polytropic index), that determine the wind velocity and acceleration.

The purpose of this paper is to examine, and quantify how variations in coronal temperature (one of the key parameters that influence the wind accelaration) will affect the stellar angular momentum loss, employing 2.5D, ideal MHD, and axisymmetric, simulations. In the following section (§3.2), we provide a brief theoretical discussion on the concept of angular momentum loss due to stellar outflows. In section 3.3, we discuss how our numerical setup is suited to study a wide range of wind acceleration profiles, and describe our parameter space. In section 3.4 we focus on the results of this study, and we show braking laws for different temperatures. In section 3.5, two new torque formulae that are independent of the flow temperature are proposed. In sections 3.6, and 3.7 we discuss some numerical issues in our simulations. Section 3.8 provides an empirical approach to predict stellar torques for any temperature. Section 3.9 contains plots of the complete simulation grid of this parameter study and finally, in section 3.10 the main conclusions of this work are summarized.

3.2 Magnetized outflows and efficiency of angular momentum loss

In general, the total angular momentum rate carried away from a star in a stellar wind can be written as

$$\tau_w = \dot{M}_w \Omega_* < R_A >^2, \tag{3.1}$$

where $\dot{M}_w$ is the integrated stellar mass loss rate due to the wind, Ω_* is the stellar rotation rate and $< R_A >^2$ is the square of a characteristic length scale in the wind. Using a mechanical analogy, $< R_A >$ can be thought of as a "lever arm length" that determines the efficiency of the torque on the star exerted by the plasma efflux. Generically, this efficiency of the angular momentum loss can be expressed as the ratio of this lever arm length to the stellar radius, R_*,

$$\frac{< R_A >}{R_*} \equiv \left(\frac{\tau_w}{\dot{M}_w \Omega_* R_*^2} \right)^{1/2}. \tag{3.2}$$

The precise value for the lengthscale $< R_A >$ depends on the detailed (and multi-dimensional) physics of the wind. As an example, a spherically symmetric, inviscid, hydrodynamical wind would simply carry away the specific angular momentum it has from the stellar surface. Thus the star is subjected to an angular momentum loss that gives $< R_A > /R_* = (2/3)^{1/2}$(e.g., Mestel 1968), which deviates from unity because the torque depends on the distance from the rotation axis (i.e., cylindrical $\varpi = r \sin\theta$), not the spherical radius r.

In a magnetized wind, Lorentz forces transmit angular momentum from the star to the wind, even after it has left the stellar surface, which can significantly increase the effieciency of angular momentum loss. Weber and Davis (1967), see also Schatzman (1962), showed that for a one-dimensional, magnetized flow along the stellar equator, under the assumption of steady-state, ideal MHD, the radius that determines the efficiency of the stellar angular momentum loss is the radial Alfvén radius. This radius is the radial distance, where the wind speed equals the local Alfvén speed (considering only the radial

components of the velocity and magnetic field). In a two or three-dimensional, ideal MHD flow, the value of $< R_A >^2$ is the mass-loss-weighted average of the square of the poloidal Alfvén (cylindrical) radius (Washimi and Shibata 1993).

In our simulations, Ω_* and R_* are specified as input parameters, and we directly compute the resulting values of τ_w and $\dot{M}_w$ in the wind solutions (see below). Thus, following Matt and Pudritz (2008), (and Matt et al. 2012a; Réville et al. 2015a; Réville et al. 2016a; Finley and Matt 2017), we compute the value of $< R_A > /R_*$ using equation (3.2) and refer to this throughout as the "torque-averaged Alfvén radius" or "effective Alfvén radius". From equation (2.32) and the definitions of $\dot{M}_w$, τ_w that are given below (see equations (3.12) and (3.13), respectively), it will become clear that R_A/R_* is equivalent to a mass-loss-weighted average, for any ideal MHD, axisymmetric and steady-state flow (see also discussion Washimi and Shibata 1993; Mestel 1999; Vidotto et al. 2014b; Cohen and Drake 2014). However, we prefer to use the terms "torque-averaged Alfvén radius" and "effective Alfvén radius" for $< R_A > /R_*$, mainly for illustrative purposes, as the exact value of this averaged lever arm depends on the global wind angular-momentum- and mass-loss rate, which are an outcome of the simulations. The simulations that will be presented here are not perfect ideal MHD and steady-state solutions, due to numerical-diffusion effects (see further discussion in sections 3.6 and 3.7 and chapter 4). Note that, defining R_A in this way does not depend on any assumptions about the physics of the angular momentum transfer (e.g., it does not require a steady-state, nor assume ideal MHD conditions); the value $(< R_A > /R_*)^2$ simply represents a dimensionless torque. Also, the scaling laws we derive below for predicting $< R_A >$ are, by definition, the appropriate lengthscale to use in equation (3.1) for computing the global torque.

3.3 Stellar Wind Solutions

3.3.1 Numerical Setup

This study employs ideal MHD and axisymmetric simulations, using the PLUTO code (Mignone et al. 2007) in a 2.5D computational grid (i.e., 2 spatial coordinates with three vector components), in order to obtain steady-state (or quasi-steady-state) stellar wind solutions. PLUTO numerically solves, in the inertial frame of reference, the following set

of ideal MHD conservation laws:

$$\partial_t \rho + \nabla \cdot \rho \boldsymbol{v} = 0, \tag{3.3}$$

$$\partial_t \boldsymbol{m} + \nabla \cdot (\boldsymbol{m}\boldsymbol{v} - \boldsymbol{B}\boldsymbol{B} + \mathbf{I} p_{tot}) = \rho \boldsymbol{g}, \tag{3.4}$$

$$\partial_t E + \nabla \cdot [(E + p_{tot})\boldsymbol{v} - \boldsymbol{B}(\boldsymbol{v} \cdot \boldsymbol{B})] = \boldsymbol{m} \cdot \boldsymbol{g}, \tag{3.5}$$

$$\partial_t \boldsymbol{B} + \nabla \cdot (\boldsymbol{v}\boldsymbol{B} - \boldsymbol{B}\boldsymbol{v}) = 0, \tag{3.6}$$

where $\partial_t \equiv \partial/\partial t$ denotes the time derivative operator, and $\mathbf{I}$ is the identity matrix. The mass density is denoted by ρ, $p_{tot} = p + \boldsymbol{B}^2/2$ is the total pressure, composed of the thermal pressure, p, and the magnetic pressure [1], $\boldsymbol{B}^2/2$. The velocity field is $\boldsymbol{v}$, $\boldsymbol{m} = \rho\boldsymbol{v}$ is the momentum density, $\boldsymbol{B}$ is the magnetic field, and $\boldsymbol{g} = -(GM_*/r^2)\widehat{r}$ represents the gravitational acceleration, where G is Newton's gravitational constant, M_* is the stellar mass, r is the distance to center of the star, and $\widehat{r}$ stands for the radial unit vector. The total energy density is $E = \rho e + \boldsymbol{m}^2/(2\rho) + \boldsymbol{B}^2/2$, where e is the specific internal energy. Finally, we adopt an equation of state for ideal gases, $\rho e = p/(\gamma - 1)$, where γ is the adiabatic exponent.

We use a second-order piecewise linear reconstruction of all the primitive variables $(\rho, \boldsymbol{v}, p, \boldsymbol{B})$ with minmod limiter, and HLL Riemann solver (e.g., Toro 2009) to compute the fluxes in equations (3.3) - (3.6). The induction equation (eq. 3.6) is solved with the constrained transport (CT) method (Balsara and Spicer 1999) in order to ensure that the divergence-free condition for the magnetic field will be maintained in our domain. The computational gird has spherical geometry for the spatial coordinates, and covers $r \in [1, 50]R_*$, where R_* is the stellar radius, and $\theta \in [0, \pi]$, with a total of 256×512 zones. A stretched grid is constructed along $\widehat{r}$ direction. The first grid zone at the stellar surface (i.e., inner boundary where $r/R_* = 1$) has size $\Delta r = 5 \times 10^{-3} R_*$ but increases with r

1. In the PLUTO code the magnetic field is defined with a factor of $1/\sqrt{4\pi}$ included.

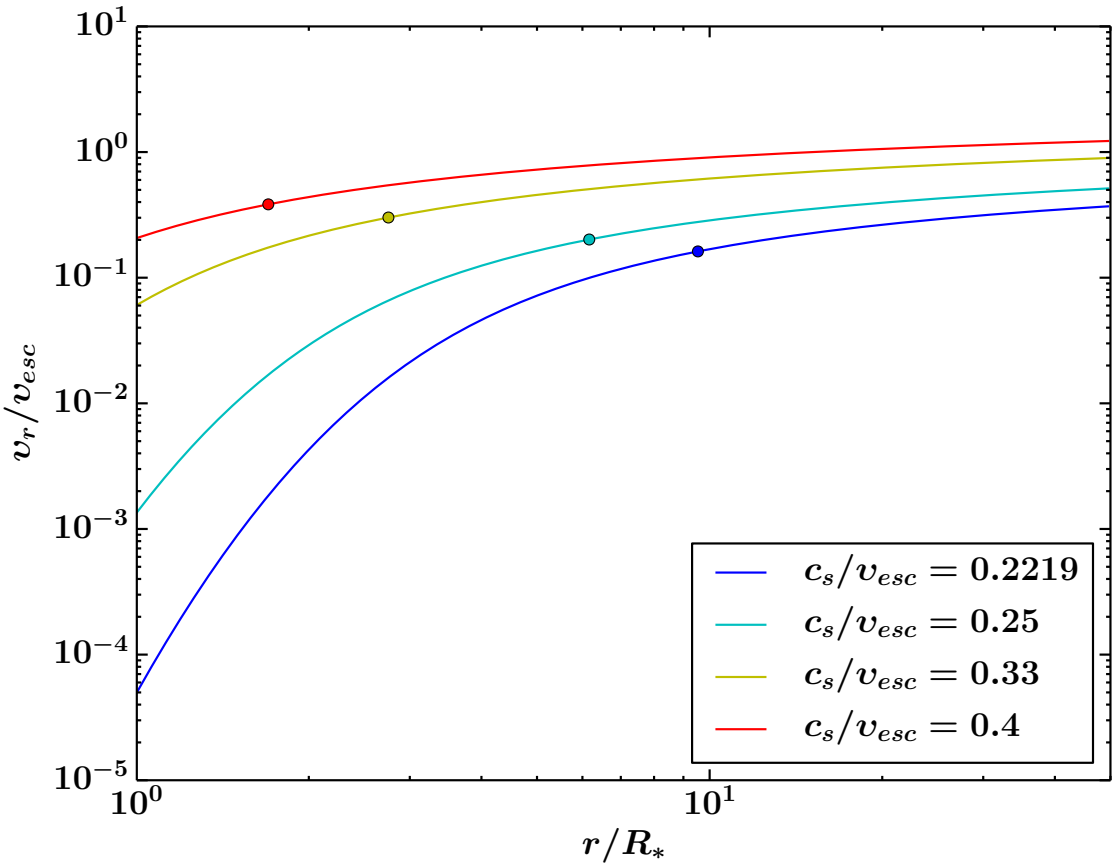

Figure 3.1: Flow velocity versus radial distance for four different temperatures, here parameterized by the ratio of the adiabatic sound speed to the escape speed from the star, for one-dimensional, hydrodynamic winds from non-rotating stars. The above profiles are also used as the initial velocity wind profile in our simulations. The circles correspond to the radial distance at which the flow becomes supersonic. Each temperature produces a unique wind acceleration profile and hotter winds always exhibit higher base and terminal velocities than cooler winds.

such that 256 points reach $50R_*$ (i.e., outer boundary), with the last grid cell having size $\Delta r = 1.015R_*$. The grid is uniform along the $\widehat{\theta}$ direction.

We initialize the whole computational domain with a dipole field, for which the radial, and polar componetnts are given by

$$B_r = 2B_* \left(\frac{R_*}{r}\right)^3 \cos\theta, \tag{3.7}$$

$$B_\theta = B_* \left(\frac{R_*}{r}\right)^3 \sin\theta, \tag{3.8}$$

where B_* is the equatorial surface field strength. We treat the magnetic field using the the "background field splitting" approach (Powell et al. 1999), which sets the dipole field as a time-independent component, and the code calculates the deviation from the initial field. This method provides better numerical accuracy in the treatment of the magnetic field, especially where strong gradients in the magnetic field might otherwise lead to significant numerical diffusion.

We also initialize our grid with a 1D, polytropic, Parker's wind solution shown in Figure 3.1, and we set the density and the thermal pressure based on the mass continuity equation and the polytropic relation ($p_{th} \propto \rho^\gamma$), respectively. Further details can be found in the following subsection (§3.3.2).

For both boundary zones of the θ coordinate we use an "axisymmetric" type of boundary condition, which symmetrizes all the variables across the borders and flips the signs of the ϕ and normal components of the vector fields. The outer boundary condition of r coordinate is set to be "outflow", which sets the gradient of each variable to be zero across the boundary. When the code starts to evolve equations (3.3) - (3.6) in time, the initial state is blown outwards and the steady-state solution, we are interested in, depends only on the inner boundary conditions. Since our wind solutions only depend on the inner boundary, that represents the stellar surface, for these ghost zones we use a more sophisticated boundary condition. We keep fixed at the stellar boundary the values for the thermal pressure and density computed from the one-dimensional polytropic

Parker's wind, we used to initialize our grid. This boundary condition corresponds to a stellar atmosphere in which its density and temperature do not vary in time and exhibit a temperature profile such that $T \propto \rho^{\gamma-1}$. Moreover, this condition ensures that the temperature of the flow does not exhibit a dependence on θ at the stellar boundary. The boundary condition for the poloidal magnetic field is forced to maintain the initial dipole state, since the flow is sub-Alfvénic and magnetic pressure dominates over the thermal and wind's hydrodynamic pressure. For the toroidal magnetic field, we linearly extrapolate the toroidal field values calculated in the computational domain into the ghost zones. For the poloidal velocity, we also linearly extrapolate the computed value of the poloidal velocity into the ghost zones, in order to have a flow velocity that increases monotonically with radius inside the ghost zones. In a steady-state and axisymmetric flow, the toroidal component of the electric field should be zero (e.g., Weber and Davis 1967; Mestel 1968, 1999; Heinemann and Olbert 1978; Lovelace et al. 1986; Sakurai 1990; Zanni and Ferreira 2009) and thus we force the poloidal component of the velocity and magnetic field to be parallel to each other. The rotation is enforced only in the stellar boundary, which we accomplish by setting the boundary condition for the toroidal component of the velocity given by the equation:

$$\upsilon_\phi = \Omega_* r \sin\theta + \frac{\upsilon_p}{B_p} B_\phi, \tag{3.9}$$

in order to satisfy the $\boldsymbol{E} = 0$ condition in a frame rotating with the star (e.g., Weber and Davis 1967; Mestel 1968, 1999; Heinemann and Olbert 1978; Lovelace et al. 1986; Sakurai 1990; Zanni and Ferreira 2009). In equation (3.9), r is the spherical radius and the subscripts p and ϕ stand for the poloidal and toroidal components respectively, of the velocity and magnetic field.

Each simulation is stopped when the solution converges to a steady-state. Some of the obtained numerical solutions are periodic, and we discuss the steadiness, and the peculiarity of these simulations in section 3.6. We further examine the correctness of each wind solution by checking how well the five constants of motion are conserved along the flow streamlines (e.g., Keppens and Goedbloed 2000). The numerical accuracy of our simulations is discussed in more detail in section 3.7.

c_s/v_{esc}	Temperature (MK°) $M_* = 1M_\odot$ $R_* = 1R_\odot$	Temperature (MK°) $M_* = 0.7M_\odot$ $R_* = 0.65R_\odot$	Temperature (MK°) $M_* = 0.5M_\odot$ $R_* = 0.47R_\odot$	Temperature (MK°) $M_* = 0.2M_\odot$ $R_* = 0.22R_\odot$
0.2219	1.30	1.40	1.39	1.20
0.25	1.65	1.77	1.77	1.52
0.33	2.88	3.09	3.08	2.66
0.4	4.23	4.53	4.53	3.90

Table 3.1: Coronal Temperatures of the Parameter Study for Different Stellar Properties.

3.3.2 Parameters of the Study

For pure hydrodynamic polytropic stellar winds the two main physical parameters that determine the wind speed and acceleration are the temperature of the plasma and the polytropic index, γ. In this study we focus on how different coronal temperatures affect the driving of the outflow and the resulting stellar magnetic torque. Below, we present four grids of simulations and on each grid, a different coronal temperature is employed. For each grid of stellar-wind solutions with a fixed coronal temperature, a parametric study on the magnetic field strength is conducted. The following three dimensionless velocities are the main input parameters of our initial setup: the ratio of the adiabatic sound speed, defined at the stellar surface, to the escape speed, c_s/v_{esc}, where $c_s = \sqrt{\gamma p_*/\rho_*}$, ("*" symbol denotes values at R_*), and $v_{esc} = \sqrt{2GM_*/R_*}$; the ratio of the Alfvén speed to the escape speed, v_A/v_{esc}, where $v_A = B_*/\sqrt{4\pi\rho_*}$, B_* is defined at the stellar equator (see also equation (3.7)), and ρ_* is the stellar surface density that is kept fixed throughout the entire study (in simulation units is set to be equal to unity); the stellar spin rate, f, that is the ratio of the stellar equatorial rotation velocity to the break-up speed, where the break-up speed is $v_{kep} = v_{esc}/\sqrt{2}$. The latter one will be held fixed for our study close to the solar value, $f = 0.00393$. The polytropic index γ and the magnetic field geometry are also parameters, but we only vary the dipolar field strengths and we fix $\gamma = 1.05$ (Washimi and Shibata 1993; Matt et al. 2012a; Réville et al. 2015a), which behaves like an adiabatically expanding flow that has energy input as the wind expands, such that $p \propto \rho^{1.05}$.

Case	c_s/v_{esc}	T_* (MK°)[1]	v_A/v_{esc}	Υ	B (G)[2]	$< R_A > /R_*$	Υ_{open}	Φ_{open}/Φ_*	$\bar{V}_{R_A}/v_{esc}$
1	0.2219	1.30	0.0151	2.90	0.216	3.62	283	0.787	0.0567
2	0.2219	1.30	0.0301	11.9	0.437	5.52	1020	0.737	0.128
3	0.2219	1.30	0.0452	27.7	0.667	6.23	1470	0.581	0.146
4	0.2219	1.30	0.0753	79.9	1.13	7.27	2330	0.430	0.17
5	0.2219	1.30	0.105	157	1.59	8.07	3170	0.358	0.187
6	0.2219	1.30	0.301	1240	4.46	11.8	9810	0.224	0.264
7	0.2219	1.30	0.627	5980	9.81	16.5	25600	0.165	0.335
8	0.2219	1.30	0.953	15000	15.5	20.2	44300	0.137	0.374
9	0.2219	1.30	1.51	41200	25.8	25.3	81300	0.112	0.415
10	0.25	1.65	0.21	33.2	0.731	4.71	1170	0.473	0.206
11	0.25	1.65	0.301	69.1	1.05	5.47	1820	0.409	0.236
12	0.25	1.65	0.627	335	2.32	7.83	5070	0.309	0.312
13	0.25	1.65	0.953	899	3.8	9.83	9460	0.258	0.361
14	0.25	1.65	1.51	2720	6.61	12.7	18600	0.208	0.413
15	0.25	1.65	2.5	8990	12.0	16.8	38200	0.164	0.465
16	0.25	1.65	4.14	29100	21.6	22.0	75700	0.128	0.512
17	0.33	2.88	0.953	16.7	0.518	3.27	1300	0.704	0.453
18	0.33	2.88	2.5	173	1.67	5.79	5470	0.448	0.609
19	0.33	2.88	3.01	275	2.11	6.47	7180	0.406	0.639
20	0.33	2.88	4.14	612	3.14	7.86	11400	0.344	0.683
21	0.33	2.88	6.2	1650	5.15	10.1	20700	0.282	0.736
22	0.33	2.88	11	6630	10.3	14.3	45600	0.209	0.802
23	0.33	2.88	17.5	20500	18.2	18.6	85000	0.162	0.845
24	0.4	4.23	4.14	194	1.77	5.68	7900	0.507	0.904
25	0.4	4.23	6.2	505	2.85	7.27	13800	0.416	0.969
26	0.4	4.23	8.6	1090	4.19	8.76	20800	0.348	1.01
27	0.4	4.23	11	1960	5.62	10.2	28800	0.305	1.04
28	0.4	4.23	17.5	5890	9.73	13.0	50800	0.234	1.10
29	0.4	4.23	26	13700	14.9	16.4	90400	0.204	1.14
30	0.4	4.23	50	62700	31.8	22.7	193000	0.140	1.21

[1] According to equation (3.10), with $M_* = 1M_\odot$ and $R_* = 1R_\odot$

[2] According to equation (3.11), with $M_* = 1M_\odot$, $R_* = 1R_\odot$, and $\dot{M}_w = \dot{M}_\odot = 2 \times 10^{-14}\mathrm{yr}^{-1}$

Table 3.2: Simulation Input Parameters and Resulting Global Wind Properties.

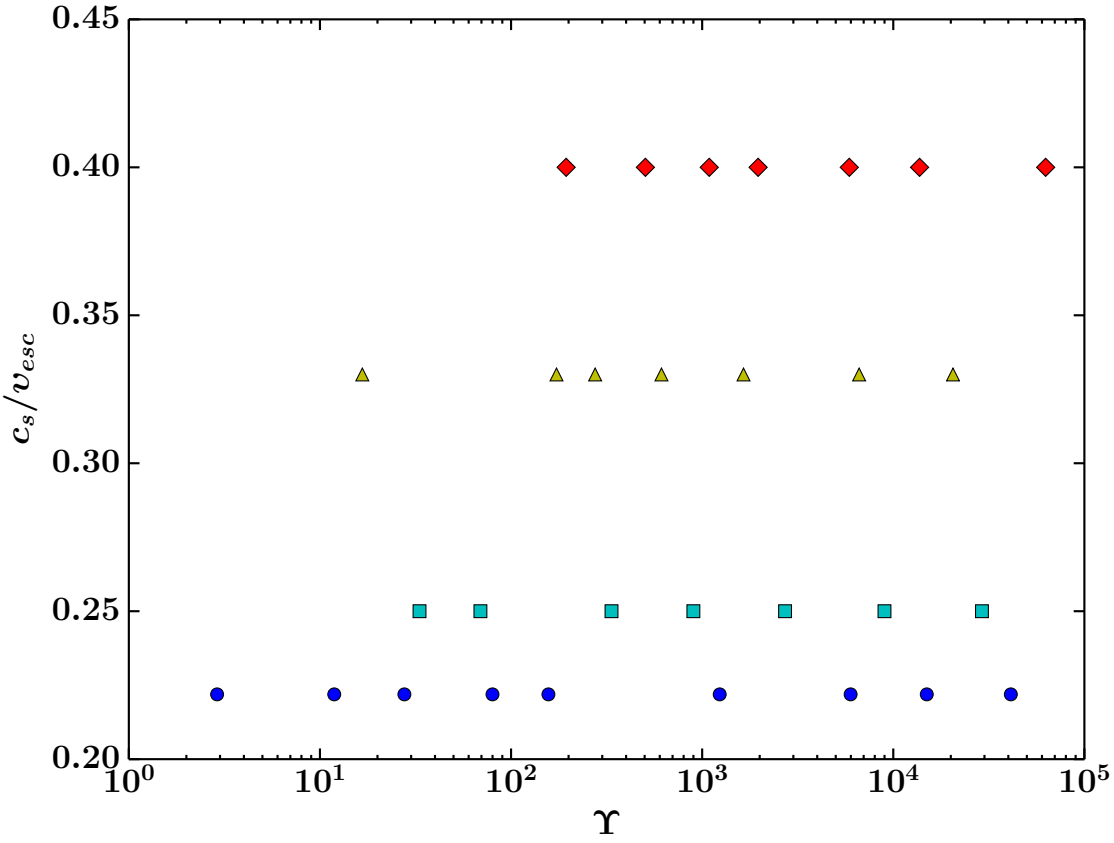

Figure 3.2: Parameter space for the 30 simulations in this study. The vertical axis shows parameter c_s/v_{esc}, which controls the flow temperature. The horizontal axis shows the paremeter Υ, which is the wind magnetization (see eq 3.11), and is associated with the average, stellar-surface magnetic field strength. Circles (blue), squares (cyan), triangles (yellow), and diamonds (red) correspond to simulations with $c_s/v_{esc} = 0..219$, 0.25, 0.33, and 0.4, respectively. Every symbol represents a single case, for which we have a steady-state, wind solution.

A polytropic treatment of the outflow acceleration is suitable for our purpose because we do not attempt to produce stellar wind solutions that will exhibit plasma properties similar to the ones observed in the solar wind such as speed bimodality, contrast in temperature and density between coronal holes and helmet streamers. Regardless, studies have shown that the polytropic approximation can capture the large-scale structure of the solar-corona magnetic field (see, e.g., Mikić et al. 1999; Riley et al. 2006) and produces wind solutions with velocity profiles that agree with the observed solar wind on large scales (see, e.g., Keppens and Goedbloed 1999; Ofman 2004).

Using the ideal-gas equation of state, the stellar coronal temperature can be written in terms of parameter c_s/v_{esc},

$$T_* = \left(\frac{c_s}{v_{esc}}\right)^2 \left(\frac{2GM_*\tilde{\mu}m_p}{\gamma R_* k_B}\right), \tag{3.10}$$

where k_B is the Boltzmann constant, m_p is the proton mass and $\tilde{\mu}$ is the mean atomic weight (i.e., the average mass per particle measured in units of m_p). For a fixed value of c_s/v_{esc} and given stellar parameters, the temperature, given by equation (3.10), depends on the mean atomic weight, $\tilde{\mu}$, that is determined by the chemical composition, and the atomic physics of the stellar atmosphere. For a solar-coronal plasma, $\tilde{\mu} = 0.6$ (e.g., Priest 2014), Table 3.1 translates c_s/v_{esc} in Kelvin, for solar parameters (with $M_\odot = 1.99 \times 10^{33}$g and $R_\odot = 6.96 \times 10^{10}$cm), and for stars at the age of the Sun, with parameters of $M_* = 0.7, 0.5, 0.2M_\odot$ and respectively $R_* = 0.65, 0.47, 0.22R_\odot$, taken from stellar evolution models of Baraffe et al. (1998).

Figure 3.1 shows velocity profiles of polytropic models for different coronal temperatures, represented in the plot by the dimensionless quantity c_s/v_{esc}. Each curve in this plot is the analytic solution of wind speed as a function of radial distance from the stellar surface, and each temperature is indicated by a different color. The plot shows that a hotter wind starts on the stellar surface at a higher speed and also reaches a higher terminal speed. To be more specific, for this range in c_s/v_{esc}, the flow speed varies by 3.5 orders of magnitude at R_*, and by more than a factor of 2 at $50R_*$. Morever, a hotter wind accelerates more rapidly compared to a cooler wind, meaning that, at every radius, the hotter

wind exhibits a higher value of both dv_r/dt and dv_r/dr. Input parameter c_s/v_{esc} varies between 0.2219 and 0.4, a range that was selected to produce reasonable wind velocity profiles for the whole grid of simulations, for a given polytropic index (i.e., $\gamma = 1.05$ in our case). This range ensures that the lowest temperature still results in a high enough flow terminal velocity for the wind to be able to escape star's gravity field. The upper limit for our flow temperature is determined so that it initiates at the stellar corona at subsonic velocities. Our wind solution with $c_s/v_{esc} = 0.4$ starts at the bottom of the flow with an initial speed that is already 50% of the sound speed, defined at the inner boundary (see fig. 3.1), and the wind becomes supersonic at $r = 1.7R_*$. Higher temperatures will result in outflows with unrealistically high base velocities (i.e., almost supersonic flow at the inner boundary). Although the polytropic wind formalism includes simplified physics that do not incorporate all relevant coronal processes that drive such outflows, Figure 3.1 shows that the range of winds we consider in our study covers a wide range of wind acceleration profiles, which may encompass the range of velocities encountered in real stellar winds under various coronal conditions.

Table 3.2 presents the parameters varied (2^{nd} and 3^{rd} columns) for all the simulated wind cases in the study. The magnetization of the wind is computed using the formula introduced in Matt and Pudritz (2008),

$$\Upsilon \equiv \frac{B_*^2 R_*^2}{\dot{M}_w v_{esc}}, \tag{3.11}$$

and the quantity Υ can be regarded as the ratio of the magnetic field energy to the kinetic energy of the flow, or as representing the interplay between the Lorentz forces and the inertia of the wind (ud-Doula and Owocki 2002). In equation (3.11), $\dot{M}_w$ is extracted directly from the simulations, and, for a given surface density, depends on the wind-driving physics, the magnetic field structure/configuration, and the numercial setup (for further discussion see Matt et al. 2012a, and subsection 3.4.1). Therefore we choose to present Υ as the second independent variable of the study, even though v_A/v_{esc} is the input parameter that controls the magnetic field strength. All the values of Υ are listed in the 4^{th} column in table 3.2. The parameter space that has been explored during the entire study is visualized in Figure 3.2, and each simulation is one symbol in this plot. Different

symbols and their corresponding colors repesent cases with different temperartures, and overall, we covered 3 to 4 orders of magnitude in wind magnetization for each temperature. Lastly, the value of B_* can be computed from Υ, for given stellar parameters and $\dot{M}_w$. For this demonstration, we adopt again solar values ($M_\odot$ and $R_\odot$ are given above). In addition, the solar mass-loss rate, during the solar minimum, is $\dot{M}_\odot = 2 \times 10^{-14} M_\odot \mathrm{yr}^{-1}$ (see e.g., Wang 1998). The values of B_* (i.e., the equatorial value of the surface dipolar field strength) are given in the 6^{th} column of table 3.2. We should mention that B_* can also be evaluated from the parameter $\upsilon_A/\upsilon_{esc}$ by adopting a value for the surface density, ρ_*. However, we prefer to use the first approach because the wind mass-loss rate is a global stellar parameter and furthermore, can be measured for other stars. (e.g., Wood et al. 2015).

3.3.3 Wind Velocity Profiles

At the start of a simulation, the presence of rotation and magnetic field modifies the initial, spherical symmetric flow, but after some time of evolution the solution relaxes to a steady-state. In order to highlight the influence of the gas temperature on the wind speed in our 2.5D MHD simulations, Figure 3.3 shows the flow poloidal velocity as a color scale on a subset of our domain for two steady-sate wind solutions. Both cases shown have the same order of magnitude in parameter Υ. The sonic surface is notated by R_s (dashed line) and the Alfvénic surface by R_A (dot-dashed line). Open field lines, that correspond to wind streamlines, are also shown. A higher coronal temperature increases the velocity of the flow (bottom panel), and as a result the sonic surface is closer to the stellar surface. The location of the Alfvén surface also comes closer to the star, and this is due to a hotter and faster wind, and also to a slightly lower magnetization of that case (i.e., case 13 with $\Upsilon = 899$ and $< R_A >= 9.83 R_*$) relative to top panel case (i.e., case 6 $\Upsilon = 1240$ and $< R_A >= 11.8 R_*$).

To show how the wind velocity profile varies with latitude, figure 3.4 illustrates the poloidal speed versus radial distance, of the plasma flowing along the streamlines of the two cases shown in Figure 3.3. Each velocity law in Figure 3.4 is individually colored, and matches the colors of the open-field lines plotted in Figure 3.3. The streamlines were chosen to be at various latitudes at $50 R_*$. The plot comprises two groups of lines, one for

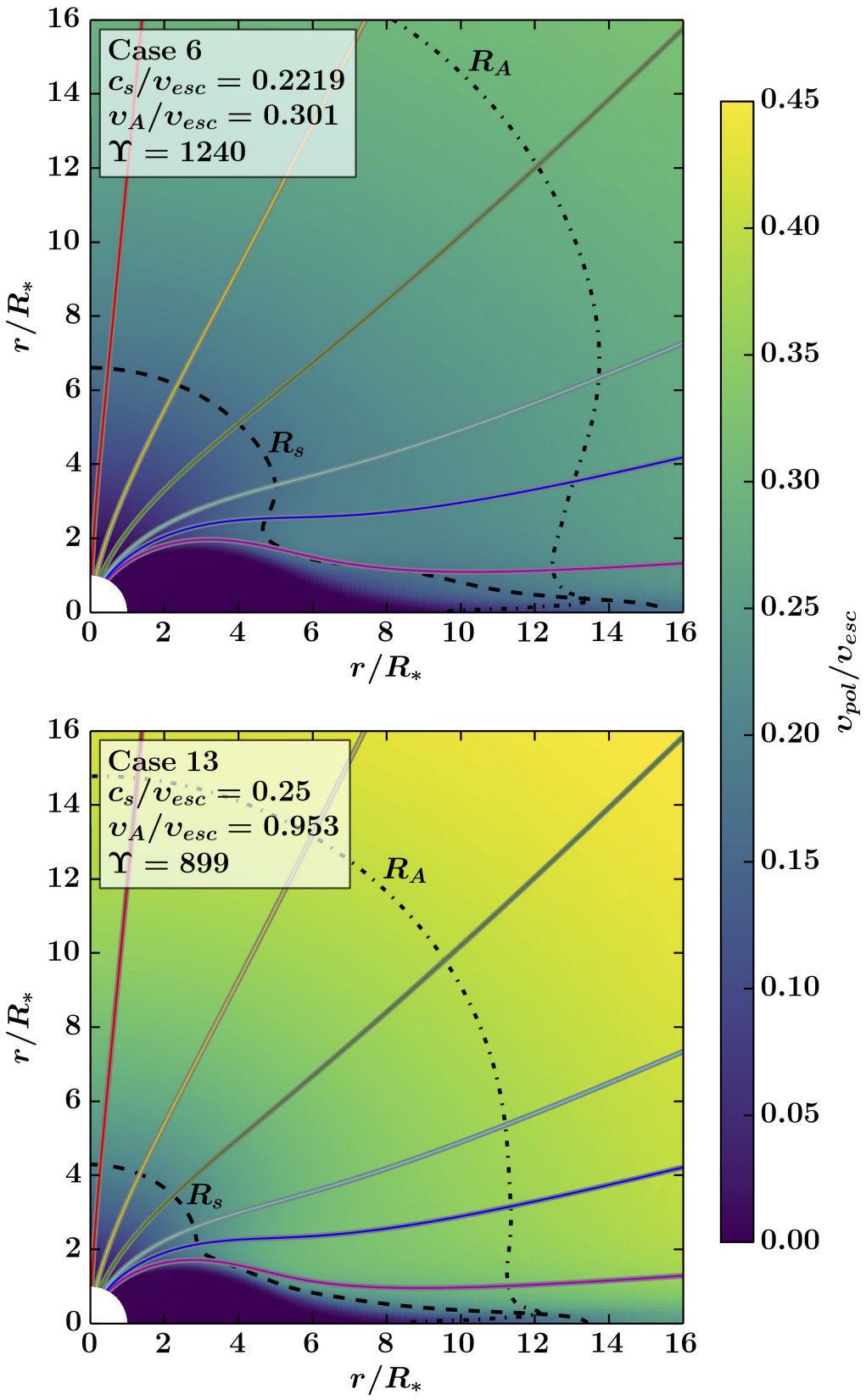

Figure 3.3: Poloidal velocity (color scale) with magnetic field lines, for two steady-state wind solutions of this study that demonstrate the two-dimensional structure of the wind and the effect of the temperature on flows with similar magnetization (parameter Υ) values. The dashed lines depict the sonic surface and the dotted lines depicts the Alfvénic surface. Each field line is plotted with a different color to indicate the paths along the flow open streamers, plotted in Figure 3.4. The images show only the northern stellar hemisphere and an inner portion of the whole computational domain.

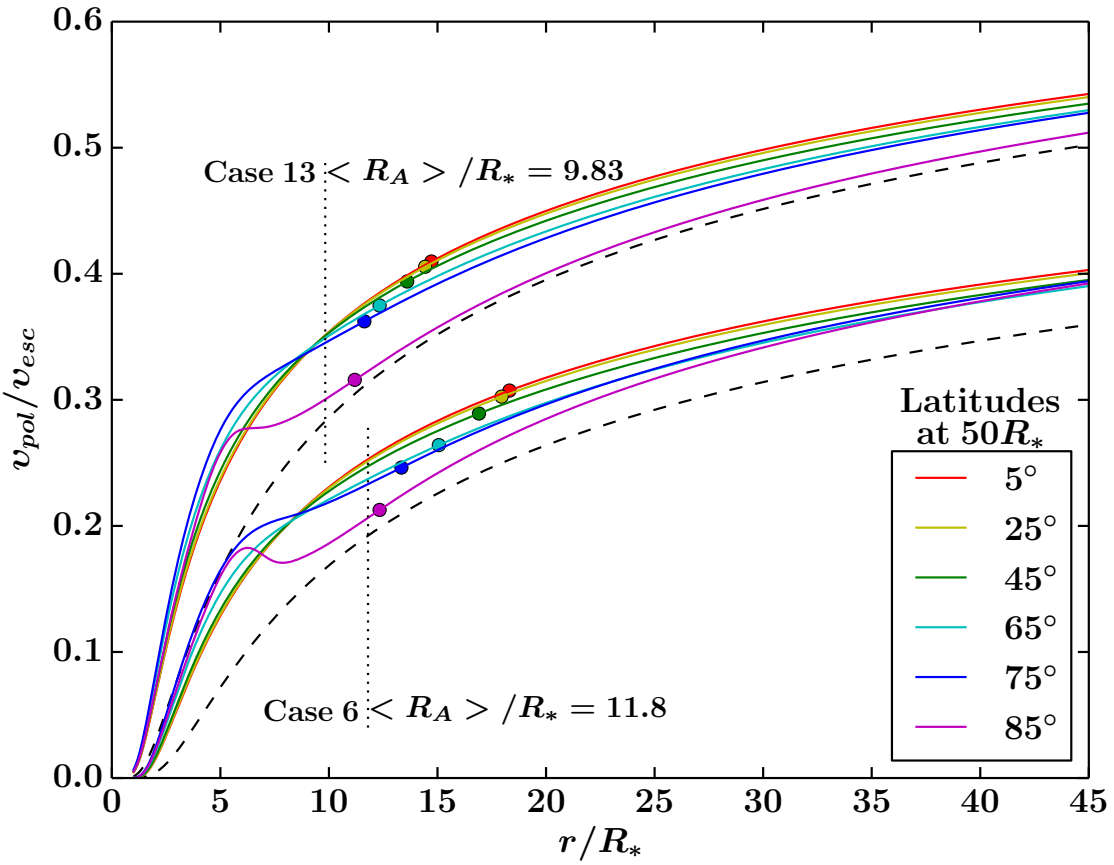

Figure 3.4: Wind speed profiles along open field lines at different latitudes, as a function of radial distance, for the cases showed in Figure 3.3. Each line color correlates with the plotted field lines in Figure 3.3. For comparison, the dashed lines represent the velocity profiles of pure, one-dimensional hydrodynamic winds. Each circle on a plotted line shows the location of the spherical Alfvén radius. The dotted lines show the torque-averaged Alfvén radius or magnetic lever-arm of the magnetized outflow.

each case, and the upper set correspond to the hotter wind (i.e., case 13). Once more, it is clear that the hotter wind accelerates more rapidly and is faster everywhere. An interesting feature shown in Figure 3.4 is that each field line produces a unique velocity profile. This behavior is attributed to the different geometrical expansion of flux tubes near the pole and close to the equator, something that originally was pointed out in Pneuman and Kopp (1971). Since all of our models are in the slow-magnetic-rotator regime (Belcher and MacGregor 1976), magneto-centrifugal effects should be negligible. In order to verify this, we repeated representative cases (not shown) from our parameter space in a pure 2D computational box (i.e., neglecting rotation). We found that in the absence of rotation, wind speed profiles do not change by more than 2% compared with simulated cases from rotating stars. Therefore, the fact that the 2D wind speed profiles are always faster compared to their 1D hydrodynamic counterparts (black dashed lines) occurs because of the overall, faster-than-r^2 divergence (i.e., superradial expansion) of the global flux-tube geometry that channels the flow (e.g., Pneuman 1966; Kopp and Holzer 1976; Réville et al. 2016b). The circles in Figure 3.4 repsresents the location of the local Alfvén radius, the radial distance at which the flow along each field line reaches the local poloidal Alfvén speed. On each field line of the two sets shown in Figure 3.4, going from the stellar pole to the equator, the local spherical Alfvén radius decreases as a consequence of the different and distinctive expansion of the crossectional area on each individual flux tube, which determines the exact profiles of the flow density and velocity, and the poloidal magnetic field strength, (see also discussion in Pneuman and Kopp 1971). At the stellar equator, the Alfvénic point is located just above the cusp or neutral point of the helmet streamer (closed magnetic loops), and thus, determines the transition region from sub-Alfvenic to super-Alfvenic flows for streamers adjacent to the last closed field line (Pneuman and Kopp 1971, see also Figure 3.3).

Finally, the black dotted vertical lines depict the size of the effective Alfvén radius. The local R_A in each streamline, is always larger compared to $< R_A >$, because the latter represents a mean value of the cylindrial Alfvén radius. Comparing the two cases, simulation 13 has a smaller effective lever arm, due to both a higher coronal temperature and a smaller Υ value and this yields a less efficient braking torque on the star.

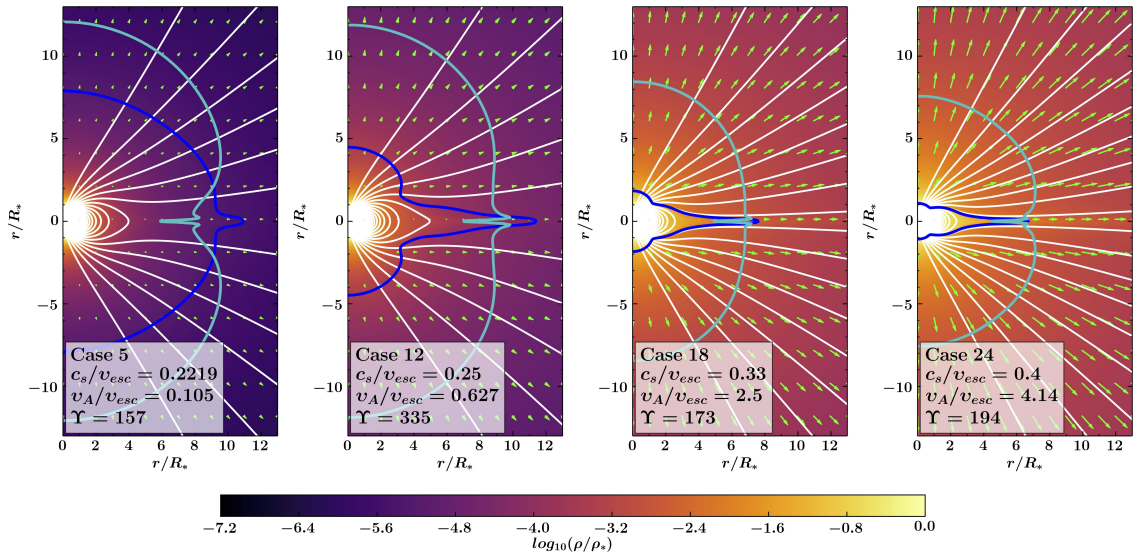

Figure 3.5: Colormaps of logarithmic density, magnetic field lines, and velocity vectors, in the inner region of four simulations with similar magnetization, Υ, but varying wind temperature (characterized by c_s/v_{esc}). The blue and cyan lines show the location of the sonic and the Alfvénic surface, respectively. A higher surface plasma temperature, for about the same value of Υ, results in a denser wind and the two critical surfaces being closer to the star.

Furthermore we observed that, for each set of simulations with a fixed value of c_s/v_{esc} (and $\gamma = 1.05$), an increase on the surface field strength (or parameter Υ) produces a wind solution that is faster everywhere in the computational domain (by $\sim 10\%$). This feature is also understood as an effect of the different geometrical expansion of the flux-tube cross section on each solution. The exact geometrical shape of the flow flux tube is determined by the cross-field force balance between the Lorentz forces, gradient of the thermal pressure force, gravity and inertia forces of the flow. In solutions with higher values of the wind magnetization, Υ, the flow expands super-radially over a longer distance (since the radius where the field obtains a radial configuration increases; see also Figure 3.12 and discussion in section 3.5.3), which leads to a more efficient acceleration of the plasma and a higher speed at the base of the wind (see also e.g., Pneuman 1966; Pneuman and Kopp 1971; Kopp and Holzer 1976).

3.4 Global Stellar Wind Properties

3.4.1 Mass and Angular Momentum Outflow Rates

Figure 3.5 displays color scale plots of logarithmic density with velocity vectors and magnetic field lines (white lines), for 4 steady-state wind solutions of our study. Each case in

figure 3.5 has the same order of magnitude (and about the same value) in magnetization, but a different plasma temperature. Qualitatively we identify that hotter winds lead to both a smaller sonic surface (blue line) and alfvénic surface (cyan line), as a consequence of being faster everywhere in the grid.

The global outflow rates of mass, $\dot{M}_w$, and angular momentum, τ_w, are numerically computed for each steady-state wind solution of the study, by using

$$\dot{M}_w = \oint_S \rho \boldsymbol{v} \cdot d\boldsymbol{S}, \tag{3.12}$$

$$\tau_w = \oint_S \Lambda \rho \boldsymbol{v} \cdot d\boldsymbol{S}, \tag{3.13}$$

where the integration occurs over any spherical surface that encloses the star, within our computational domain, and

$$\Lambda = r \sin\theta \left(\upsilon_\phi - B_\phi \frac{B_p}{4\pi\rho\upsilon_p} \right). \tag{3.14}$$

In the ideal MHD regime, Λ gives the specific angular momentum carried away by the wind along a streamline, and is a constant of motion for an axisymmetric, steady-state flow. In practice, we calculate both rates as functions of spherical radius r, and use the median values obtained from all the integrated $\dot{M}_w(r)$ and $\tau_w(r)$ over spherical shells above $10R_*$ as global $\dot{M}_w$ and τ_w. This method avoids numerical diffusion effects that might cause non conservation of mass and angular momentum flux close to the stellar boundary. To be more specific, we noticed that the numerical diffusion produced by the scheme used in this study (consequence of the choices on the Riemann solver and flux limiter) affects our simulations. This particular scheme produces solutions in which $\dot{M}_w$ and τ_w are not constant as functions of r (i.e., non conservation of mass and angular momentum) at the first few stellar radii. However, the method described above provides the global values of $\dot{M}_w$ and τ_w from the region in the computational domain, where numerical-diffusion effects are less important. We further discuss this feature in chapter 4 (see §4.3.2) and furthermore, in that chapter we present a new improved setup for ideal MHD, axisymmetric, and steady-state stellar-wind simulations that does not produce this kind of

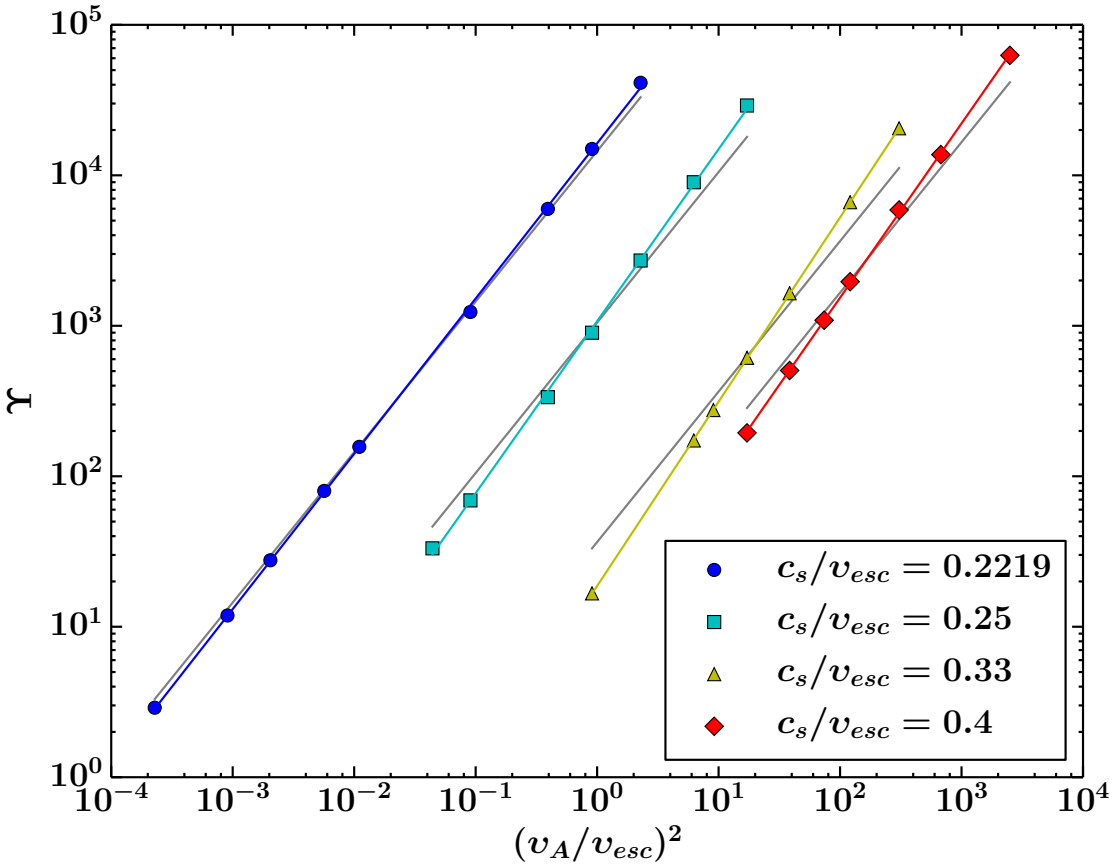

Figure 3.6: Wind magnetization, Υ, versus square of input parameter v_A/v_{esc}. Colors and symbols have the same meaning as in Figure 3.2. In our simulations, $\Upsilon \propto (v_A/v_{esc})^2/\dot{M}_w$, and for a given value of v_A/v_{esc}, a hotter wind has have a much higher mass loss rate. Grey scaling laws have a slope of unity. For a given coronal temperature, each scaling law has a slope steeper that unity, indicating that $\dot{M}_w$ decreases weakly with an increasing v_A/v_{esc}.

numerical features. We then determine the torque-averaged Alfvén radius, $< R_A > /R_*$, from equation (3.2), and these are listed in 5^{th} column of Table 3.2.

Another way to illustrate the range of the parameter space is to express Υ in terms of the input parameter v_A/v_{esc}. By manipulating equation (3.11), one can derive that $\Upsilon \propto (v_A/v_{esc})^2/\dot{M}_w$, (i.e., Υ depends on v_A/v_{esc}, that controls the surface magnetic field strength, but also is inversely proportional to the stellar mass loss rate, which is an output of the simulations). Figure 3.6 shows that the four different temperatures of our models follow four different scaling laws of Υ versus the square of v_A/v_{esc}. An increase in c_s/v_{esc} singnificantly affects the stellar mass-loss rates by increasing the speed at the base of the wind. As a result Υ decreases and therefore, we use a different range in field strengths (i.e., range in v_A/v_{esc}, see also the third column in Table 3.2) for each grid of stellar-wind

solutions with a fixed coronal temperature. This way, we are able to achieve about the same range in the wind magnetization, Υ, for all the four sets of simulations. By doing this, we avoid simulations with a small value of $\upsilon_A/\upsilon_{esc}$, and as a consequence a small value of Υ, since for such cases the Alfvén surface is very close to the stellar surface. There is no physical reason for not considering cases with wind magnetization above 10^5, but these simulations start to become numerically very challenging, due to smaller numerical time-steps and large numerical errors (for further details on the accuracy of the numerical solutions see section 3.7).

The grey lines in Figure 3.6 correspond to scaling laws with slopes of unity, and show how the parameter Υ would depend on $\upsilon_A/\upsilon_{esc}$, if the stellar mass loss rate was constant for a grid of simulations with a given coronal temperature, and thus independent of stellar surface magnetic field strength. The fact that we find steeper power-laws, (the slopes are respectively 1.03, 1.14, 1.22, and 1.16 for $c_s/\upsilon_{esc} = 0.2219, 0.25, 0.33, 0.4$), indicates that the mass loss rates actually decrease with increased field strengths. This feature can be physically explained by an interplay between two competing effects. A stronger field leads to higher flow injection speed at the inner boundary and in general to a slightly faster wind at all r, but also to a smaller area on the stellar surface carrying mass flow. The latter can be explained due to the fact that in cases with a fixed coronal temperature, a higher field strength increases the size of the dead zone and therefore, the area that is occupied by the stellar wind decreases (see for example Figure 3.16 in section 3.9). The fact that a higher field strength, for fixed thermodynamics at the base of the flow, also leads to a faster wind, is a geomteric effect of the flux tube expansion (discussed in section 3.3.3). Figure 3.6 indicates that the net result is a slightly decreasing $\dot{M}_w$. A similar trend was also seen in Réville et al. (2015a). Nevertheless, we should be cautious in interpreting the scaling laws in figure 3.6 as realistic stellar mass-loss indicators, since polytropic wind models lack the exact physics that drive outflows from solar- and late-type stars. Early studies in the solar wind (Leer and Holzer 1980) showed that where the energy is added in the flow has a big influence on the resulting solar mass loss rate. Moreover latest theoretical models (Cranmer and Saar 2011; Suzuki et al. 2013), suggest that a realistic treatment of coronal heating is needed for accurate predictions on stellar mass loss rates from cool stars. Therefore, the scaling laws between Υ and $\upsilon_A/\upsilon_{esc}$ can be interpreted as a part of

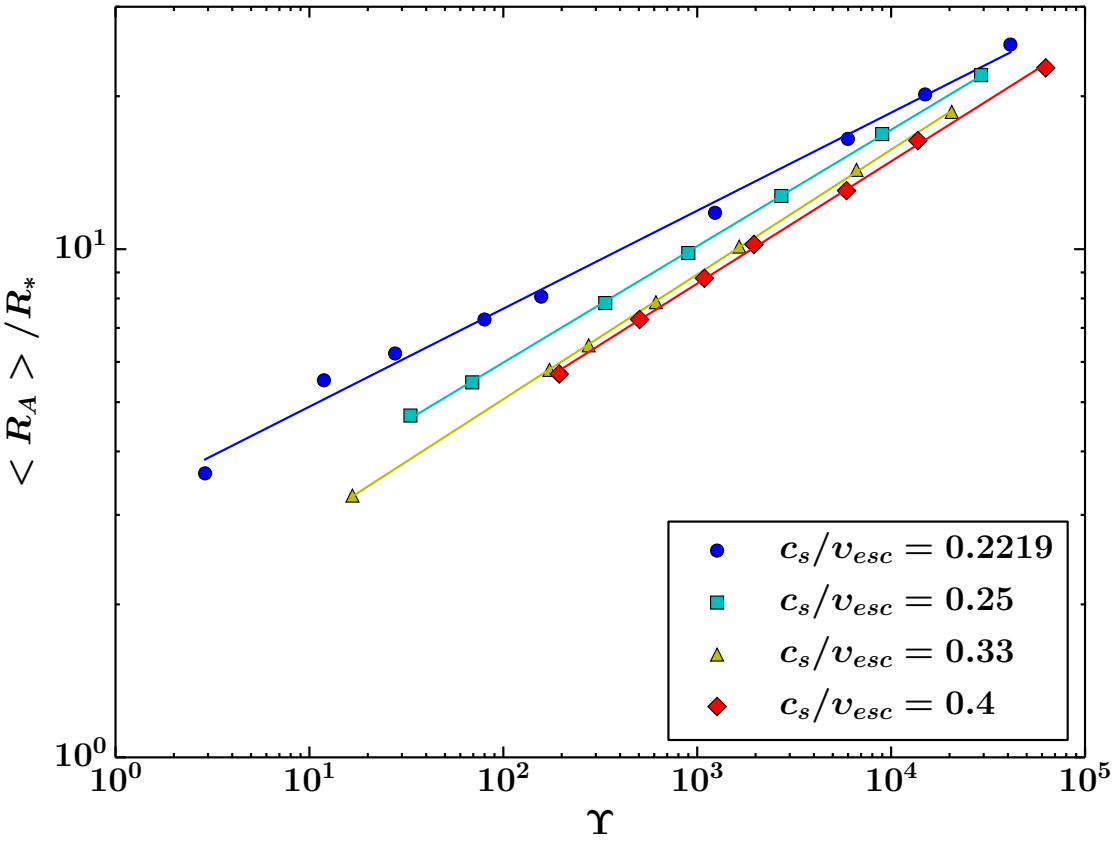

Figure 3.7: The dependence of the effective Alfvén radius, $< R_A > /R_*$, on Υ for all the cases of the parameter study. The colors/symbols have the same meaning as in Figure 3.2. Four simple power laws of $< R_A > /R_*$ on parameter Υ are shown, and each one corresponds to a different value of c_s/v_{esc}. For a given Υ, the magnetic lever arm (i.e., $< R_A > /R_*$) of the wind decreases, with an increasing coronal temperature, and as a consequence the torque exerted on the star becomes less efficient.

the generic phenomenology in our simulations, and should not be regarded as trends that give accurate predictions on mass loss rates in solar- and late-type stars. Still our formulae shall provide the exerted magnetic torque for any given $\dot{M}_w$, extracted from observations (e.g., Wood et al. 2002; Wood et al. 2014) or modeling (e.g., Holzwarth and Jardine 2007; Cranmer and Saar 2011; Suzuki et al. 2013).

3.4.2 Scaling Laws Between Alfvén Radius and Υ

The dependence of the effective Alfvén radius, $< R_A > /R_*$ on wind magnetization, Υ, for all the numerical solutions of the study is depicted in Figure 3.7. Each point in Figure 3.7 corresponds to a single simulation, and the color and symbols have the same meaning as in Figure 3.6. In order to fit the simulation data, we use the formulation introduced in

Matt and Pudritz (2008), that scales $< R_A > /R_*$ as a power law in Υ,

$$\frac{< R_A >}{R_*} = K_s \Upsilon^{m_s}, \tag{3.15}$$

where K_s and m_s are dimensionless fitting constants and equation (3.15) determines the effective Alfvén radius, $< R_A > /R_*$, in terms of the magnetic field strength on the stellar surface, for given $\dot{M}_w$, M_*, and R_*. Four different fitting laws are shown in Figure 3.7, and the values of K_s and m_s for every fit are given in 2^{nd} and 3^{rd} column of Table 3.3.

Each value of c_s/v_{esc} gives a simple power law of the torque-averaged Alfvén radius on Υ for various surface magnetic field strengths. However the fit parameters are different with each coronal temperature. The power law for $c_s/v_{esc} = 0.2219$ is shallower, (see also Table 3.3), compared with previous parameter studies (Matt et al. 2012a; Réville et al. 2015a), and can be understood as an effect due to differences in the numerical setup between the studies (e.g., geometry of the problem, numerical scheme, different approach on boundary conditions), indicative of systematic errors. Réville et al. (2015a) demonstrated different power laws resulted from different field geometries. It was also shown that the complexity of the magnetic field does not significantly influence the wind acceleration. For this study only dipolar fields are considered, but by varying the gas temperature, we actually change the acceleration of the flow. As a consequence the wind speed also changes, for simulations with different values of c_s/v_{esc}, and that physically explains the four power laws in Figure 3.7. In conclusion, hotter winds are faster, and thus, the Alfvén surface comes closer to the star, the size of the lever arm or the effective Alfvén radius decreases, and therefore the magnetic braking torque that is exerted on the star becomes weaker.

c_s/v_{esc}	K_s	m_s	$1/(4+q)$	K_o	m_o	$1/(2+q)$	K_q	q
0.2219	3.1 ± 0.1	0.193 ± 0.005	0.202 ± 0.004	0.51 ± 0.01	0.343 ± 0.003	0.34 ± 0.01	0.023 ± 0.005	0.94 ± 0.09
0.25	2.08 ± 0.02	0.229 ± 0.001	0.218 ± 0.002	0.34 ± 0.01	0.370 ± 0.004	0.386 ± 0.006	0.088 ± 0.009	0.59 ± 0.04
0.33	1.64 ± 0.01	0.246 ± 0.001	0.230 ± 0.002	0.160 ± 0.007	0.418 ± 0.004	0.426 ± 0.006	0.32 ± 0.02	0.35 ± 0.03
0.4	1.63 ± 0.04	0.240 ± 0.003	0.2378 ± 0.0005	0.118 ± 0.006	0.433 ± 0.005	0.454 ± 0.002	0.64 ± 0.01	0.205 ± 0.009
0.2219[1]	2.49	0.2177	-	-	-	-	-	-
0.2219[2]	2.0 ± 0.1	0.235 ± 0.007	0.21	0.65 ± 0.05	0.31 ± 0.02	0.37	-	0.7

[1] Matt et al. (2012a)
[2] Réville et al. (2015a) and Réville et al. (2016a)

Table 3.3: Fitting Constants For Equations (3.15), (3.18), and (3.28) in Figures 3.7, 3.8, and 3.10 of the Parameter Study.

3.4.3 Scaling Laws Using the Amount of Open Magnetic Flux

In Réville et al. (2015a) an alternative formulation for the torque-averaged Alfvén radius was introduced, that scales $< R_A > /R_*$ as a power law in a new Υ-like parameter that depends on the amount of open magnetic flux, (see also Washimi and Shibata 1993). In general, the unsigned magnetic flux of the stellar magnetic field, as a function of spherical radius r, can be evaluated as,

$$\Phi(r) = \oint_S |\boldsymbol{B} \cdot d\boldsymbol{S}|, \tag{3.16}$$

where the integration is performed over spherical surfaces that enclose that star. For a given field geometry, dipole in our case, magnetic flux initially drops as $1/r$, but there is a regime in which the thermal pressure and the inertia of the wind dominates over the magnetic stresses, the field completely opens and the magnitude of the magnetic flux becomes constant (i.e., open magnetic flux), see for example figure 5 in Réville et al. (2015a).

Following Réville et al. (2015a), the new Υ-like parameter, is defined as,

$$\Upsilon_{open} \equiv \frac{\Phi_{open}^2}{R_*^2 \dot{M}_w v_{esc}}, \tag{3.17}$$

where Φ_{open} is the open magnetic flux that is directly computed from the numerical simulations by equation (3.16). We use as Φ_{open}, for a given wind solution, the median value of $\Phi(r)$ above the corresponding $< R_A > /R_*$ of that solution, where we have identified that magnetic flux is constant. The 6^{th} column in Table 3.2 lists all the values of Υ_{open}. The 7^{th} column in Table 3.2 contains all the values of the fractional open flux (i.e., Φ_{open} normalized to the surface unsigned magnetic flux, Φ_*), which can be written as $\Phi_{open}/\Phi_* = (\Upsilon_{open}/\Upsilon)^{1/2}/(4\pi)$.

The value of $< R_A > /R_*$ versus parameter Υ_{open}, for the entire study, is presented in Figure 3.8. Similarly to equation (3.15), a function in the form of

$$< R_A > /R_* = K_o \Upsilon_{open}^{m_o} \tag{3.18}$$

fits tha data, and again K_o and m_o represent dimensionless fitting constants and the quantity $< R_A > /R_*$ is determined here in terms of the open magnetic flux. Four power laws are shown in Figure 3.8, and the 5^{th} and 6^{th} column in Table 3.3 lists the values of the fitting constants for each scaling law. The figure demonstrates, how the effective Alfvén radius scales as a simple braking law with parameter Υ_{open}, for every value of c_s/v_{esc}. Furthermore, Figure 3.8 illustrates and qunatifies how the temperature of the flow, which determines the wind velocity and acceleration profile, affects the magnetic braking of low-mass stars (see also, Weber and Davis 1967; Parker 1963; Mestel and Spruit 1987). For the flow acceleration profiles studied here, $< R_A > /R_*$ varies by about a factor 2, for a given value of Υ_{open}. Réville et al. (2015a) showed that all the wind solutions in their study followed one unique power law, demonstrating that the $< R_A > /R_*$-versus-Υ_{open} scaling was independent of the field geometry, but they assumed a fixed stellar coronal temperature. The fact that our power law, for $c_s/v_{esc} = 0.2219$, is steeper (see also Table 3.3), compared to the single braking law found in Réville et al. (2015a), might be explained as an effect due to different choices in the numerical setups of the two studies, as discussed in the previous subsection. An influence on the braking laws, due to a different coronal temperature has also been observed in Réville et al. (2016a). In conclusion, the temperature of the flow affects the size of the magnetic lever-arm (i.e., $< R_A > /R_*$), and the efficiency of magnetic braking.

3.5 Magnetic braking laws for known wind acceleration profile

3.5.1 Semi-analytic Model for Alfvén Radius versus Υ_{open}

We showed above that the flow temperature and the resulting wind acceleration can influence the efficiency of the braking toque. For this section, our objective is to provide a more generic braking law that will take this effect into account.

In order to mathematically express the dependence of the braking laws on the acceleration profile of the flow, we will employ similar one-dimensional analysis that was used in earlier works (e.g Kawaler 1988; Tout and Pringle 1992; Matt and Pudritz 2008;

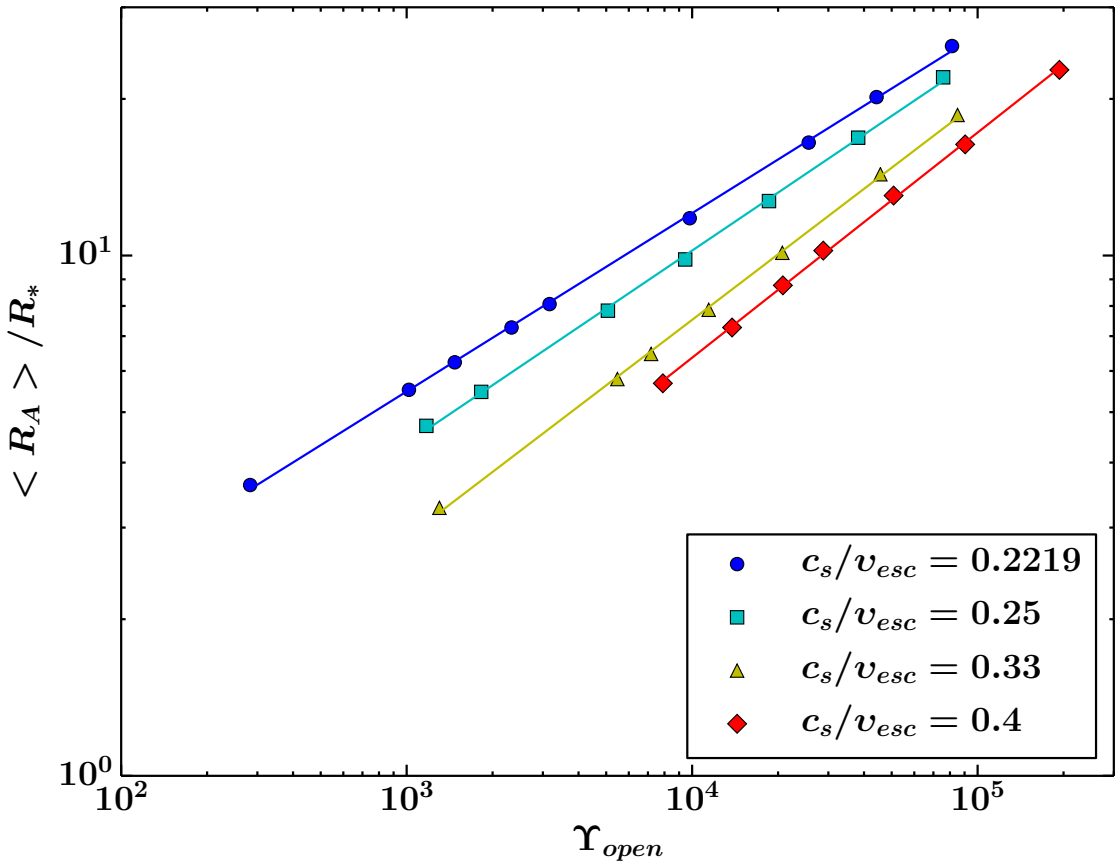

Figure 3.8: Effective Alfvén radius, $< R_A > /R_*$, versus the parameter Υ_{open} (eq. 3.18) for all the simulations of the study. Colors/symbols are the same as in figure 3.2. Four different fitting laws are shown, one for each set of wind solutions with a given value of c_s/v_{esc}. An increase in the temperature of the flow, for winds with the same value of Υ_{open}, results in a decrease of the size of $< R_A > /R_*$ and the efficiency of the braking torque.

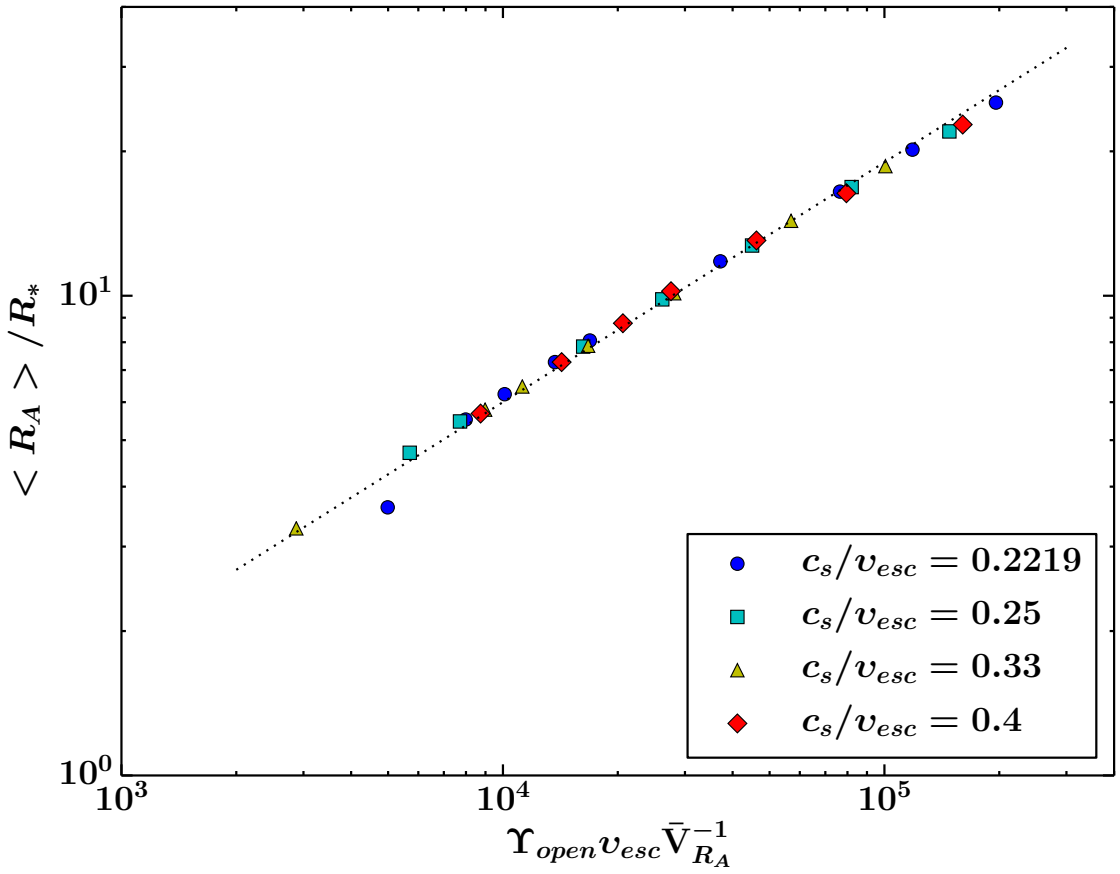

Figure 3.9: Effective Alfvén radius, $< R_A > /R_*$, versus the quantity $\Upsilon_{open} v_{esc} \bar{V}_{R_A}^{-1}$ for all the simulation data. Colors/symbols have the same meaning as in Figure 3.2. All the data points collapse in a single braking law, compared to Figure 3.8. The slope (or power-law index) of the dotted line is fixed to 1/2, and fits the data according to equation (3.26).

Réville et al. 2015a). Note that, the wind solutions of this study are multidimensional and the one-dimensional analysis, presented here, will show the dependence of $< R_A > /R_*$ on the global parameters of the simulations (e.g., coronal temperature, field strength and geometry). However, the scaling laws for $< R_A > /R_*$, which are derived below, should not be directly used to represent the data (e.g., in Figures 3.7, 3.8, 3.9, and 3.11) as they do not consider two-dimensional effects (e.g., latitudinal variations). Thus, we fit the simulation data with fitting functions that are based on these scaling laws. For a one-dimensional, MHD flow, along a magnetic flux tube, the wind velocity at the Alfvén radius, by definition, is equal to the local Afvén speed. This is

$$\upsilon^2(R_A) = \upsilon_A^2 = \frac{B_A^2}{4\pi\rho_A}, \tag{3.19}$$

where B_A and ρ_A are the local magnetic field and density respectively, at the Alfvén surface. In order to evaluate B_A at R_A, one must specify how the magnetic field strength depends on radius. Hence, for this work, we adopt a prescription similar to Mestel and Spruit (1987), see also Mestel (1999), in which the magnetic field is approximated as having two regions. The inner region exists from the stellar surface out to the "open-field" radius, R_o, in which the field is a single power law in radius,

$$B(r \leq R_o) = B_* \left(\frac{R_*}{r}\right)^{l+2}, \tag{3.20}$$

with $l = 1$ for a dipole. The outer region lies above R_o in which the field decreases as a monopole, (i.e., $l = 0$),

$$B(r \geq R_o) = B_o \left(\frac{R_o}{r}\right)^2, \tag{3.21}$$

where B_o denotes $B(R_o)$, given by equation (3.20). We also assume that the flow is the same along every field line (i.e., all values are only a function of radius and not latitude) and in a steady-state.

This treatment for the stellar magnetic field is a simple approximation for the real magnetic field configurations in a wind, where near the star, the field closely resembles the potential field, and further out, it is stretched to a nearly radial configuration by the flow

(see for example Figure 3.5). For a detailed comparison of the magnetic field in a wind simulation with a potential and radial field, see Réville et al. (2015b).

In all our simulations the Alfvén surface is located at the open-field region, and therefore, we assume that the condition $R_A > R_o$ holds for all our cases as if they were 1D flows. Then, by combining equations (3.20) and (3.21), the magnetic field strength at R_A can now be written

$$B_A = B_o \left(\frac{R_o}{R_A}\right)^2 = B_* \left(\frac{R_*}{R_o}\right)^{l+2} \left(\frac{R_o}{R_A}\right)^2. \tag{3.22}$$

Since magnetic flux is conserved, it can be written at the Alfvén radius as

$$\Phi_A = 4\pi R_A^2 B_A = 4\pi R_o^2 B_o = \Phi_{open}, \tag{3.23}$$

which equals the total open flux in the wind. By combining equations (3.17), (3.19), and (3.23), we get

$$\left(\frac{R_A}{R_*}\right)^2 = \frac{1}{(4\pi)^2} \Upsilon_{open} \frac{\upsilon_{esc}}{\upsilon(R_A)}, \tag{3.24}$$

where we have used $\dot{M}_w = 4\pi \rho_A R_A^2 \upsilon(R_A)$, for a spherical symmetric flow in the open-field region.

Since our wind solutions are multi-dimensional, we can associate the terms R_A/R_* and $\upsilon(R_A)$ in equation (3.24) with the torque-averaged Alfvén radius, $< R_A > /R_*$ and $\bar{\mathrm{V}}_{R_A}$, where $\bar{\mathrm{V}}_{R_A}$ represents the average wind speed at the Alfvén surface. We define

$$\bar{\mathrm{V}}_{R_A} \equiv \frac{\sum_i^N \upsilon[(R_A)_i, \theta_i],}{N}, \tag{3.25}$$

where the sum is over each discretized grid point i along the Alfvén surface. $\bar{\mathrm{V}}_{R_A}$ is computed individually for each case in the study, and the values are listed in the 8^{th} column in Table 3.2.

Following equation (3.24), we plot $< R_A > /R_*$ versus the new quantity, $\Upsilon_{open} \upsilon_{esc} \bar{\mathrm{V}}_{R_A}^{-1}$,

as depicted in Figure 3.9, and fit the data to the function

$$\frac{< R_A >}{R_*} = K_c \left(\Upsilon_{open} \frac{\upsilon_{esc}}{\bar{\mathrm{V}}_{R_A}} \right)^{1/2}, \tag{3.26}$$

where again K_c is introduced as a dimesionless fitting constant and its value should only deviate from $1/(4\pi)$ due to 2D effects, neglected in equation (3.24). The best-fit value for K_c gives

$$K_c = 0.7540 \left(\frac{1}{4\pi} \right) \pm 0.0004. \tag{3.27}$$

By including in our torque formalism, the dimensionless term $\upsilon_{esc}/\bar{\mathrm{V}}_{R_A}$, that contains all the information regarding the velocity and acceleration profile of the outflow, all the data points in Figure 3.9 collapse in one single and precise power-law. Hence, equation (3.26) estimates the effective Alfvén radius of any wind, as long as Υ_{open} is known and $\bar{\mathrm{V}}_{R_A}$ can be predicted.

3.5.2 Power-law Approximation for Wind Velocity at the Alfvén Radius, $\bar{\mathrm{V}}_{R_A}$

Equation (3.26) can naturally explain the simple power laws in Figure 3.8, if wind speed, $\bar{\mathrm{V}}_{R_A}$, is also a power-law in $< R_A > /R_*$ but with a scaling that varies for each temperature. To verify this, we plot $\bar{\mathrm{V}}_{R_A}$ versus the torque-averaged Alfvén radius, $< R_A > /R_*$, for all the simulations in Figure 3.10. For comparison, the velocity profiles of the polytropic, Parker wind models, shown in Figure 3.1, are also plotted. We fit a power-law function to the data, given by

$$\frac{\bar{\mathrm{V}}_{R_A}}{\upsilon_{esc}} = K_q \left(\frac{< R_A >}{R_*} \right)^q \tag{3.28}$$

where K_q and q are both dimensionless fitting constants, related to the acceleration profile of the wind. Each temperature gives us a separate pair of K_q and q, tabulated in the 8^{th} and 9^{th} column of Table 3.3, respectively. The value of q, found in Réville et al. (2015a), is also given in Table 3.3.

It is clear that equation (3.28) is valid as a first order approximation, despite the

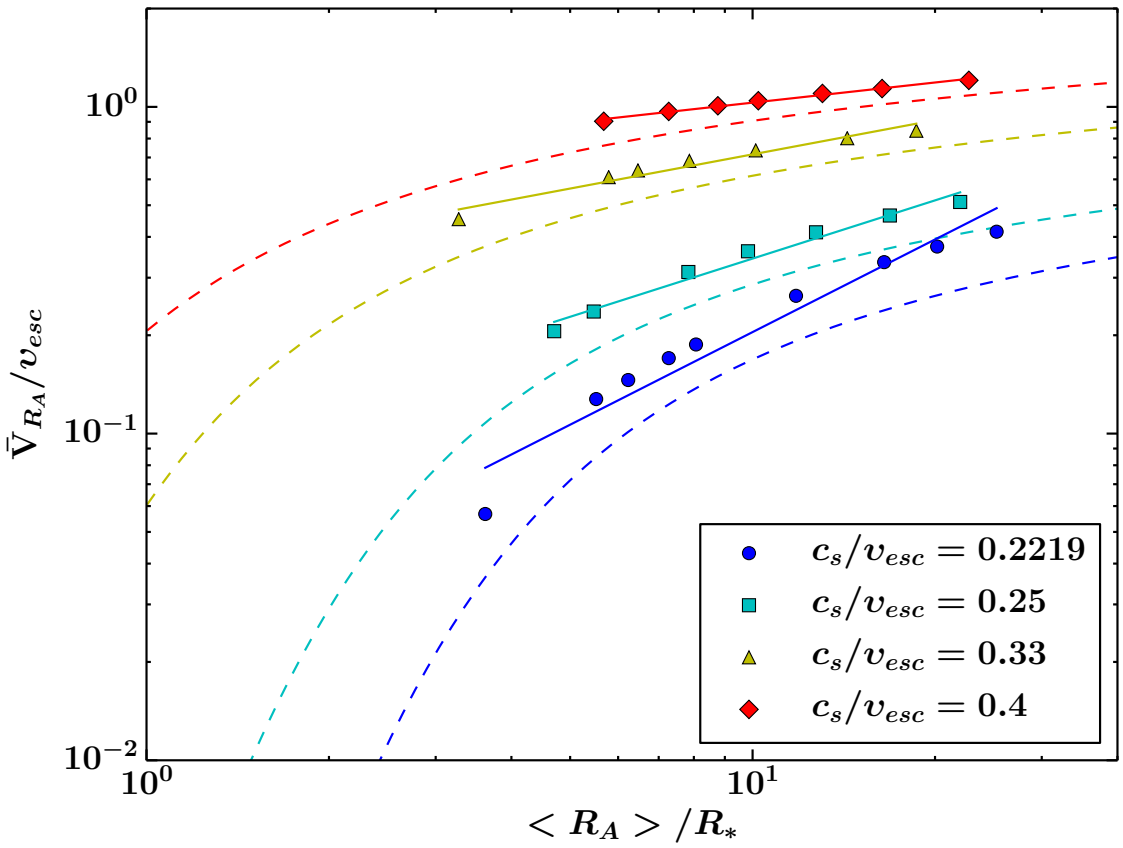

Figure 3.10: Average flow speed at the Alfvén surface, $\bar{V}_{R_A}$, versus $< R_A > /R_*$ for all the simulated cases of the study. Colors/symbols are the same as in Figure 3.2. Each point in this plot represents the average wind speed at the Alfvén radius of a single wind solution (eq. 3.25). The solid lines represent the equation (3.28) with fit parameters listed in Table 3.3. For comparison, the dashed lines show the normalized radial velocity, v_r/v_{esc}, as a function of r/R_*, of the 1D, hydrodynamic, winds illustrated in Figure 3.1.

fact that the simulated winds do not follow a perfect power law (solid lines in Figure 3.10) and the behavior of $\bar{\mathrm{V}}_{R_A}$, as a function of $< R_A > /R_*$, exhibit a similar shape to 1D, hydrodynamic winds of the same value of c_s/v_{esc} (dashed lines in fig. 3.10). Perhaps, for even more precise stellar-torque formulae, a different velocity law could be applied (e.g., modified beta-law, see for example Lamers and Cassinelli (1999)). Nonetheless, over a small range of radii, these trends can be approximated by a power law, and that approximate fit, explains the power-law behavior in figure 3.8. In addition, working with equation (3.28), one can analytically solve equation (3.26) for $< R_A > /R_*$, (see below).

Another interesting trend in Figure 3.10 is that the plotted data points are noticeably above the hydrodynamic wind velocity profiles. This can be understood as an effect due to both, the differences in the geometry of the two flows (see e.g., figure 3 in Pneuman 1966, and further discussion in section 3.3.3) and the specific way the averaging and the scaling was done in equation (3.28). Figure 3.10 also indicates why the braking laws in figures 3.7 and 3.8 start to converge, for higher coronal temperatures (e.g., the yellow and red lines with $c_s/v_{esc} = 0.33, 0.4$). Hotter flows enter the regime where the wind speed starts to saturate to wind terminal speed (i.e., speed at infinity), in a shorter radial distance compared to cooler winds. Hence, outflows that approach an almost constant speed, suggest a q that asymptotes to zero. Lastly, we found two empirical functions, which predict fitting constants K_q and q over any continuous range of values of c_s/v_{esc}. These functions are,

$$K_q = 1.36[5.87(c_s/v_{esc})^2 - 1.18(c_s/v_{esc})], \tag{3.29}$$

$$q = 0.932[0.000979(c_s/v_{esc})^{-4.51} + 0.553(c_s/v_{esc})]. \tag{3.30}$$

The method and the derivation of equations (3.29) and (3.30) exist in section 3.8.

By combining equations (3.26) and (3.28), we obtain

$$\frac{< R_A >}{R_*} = \left(\frac{K_c^2}{K_q}\Upsilon_{open}\right)^{1/(2+q)}. \tag{3.31}$$

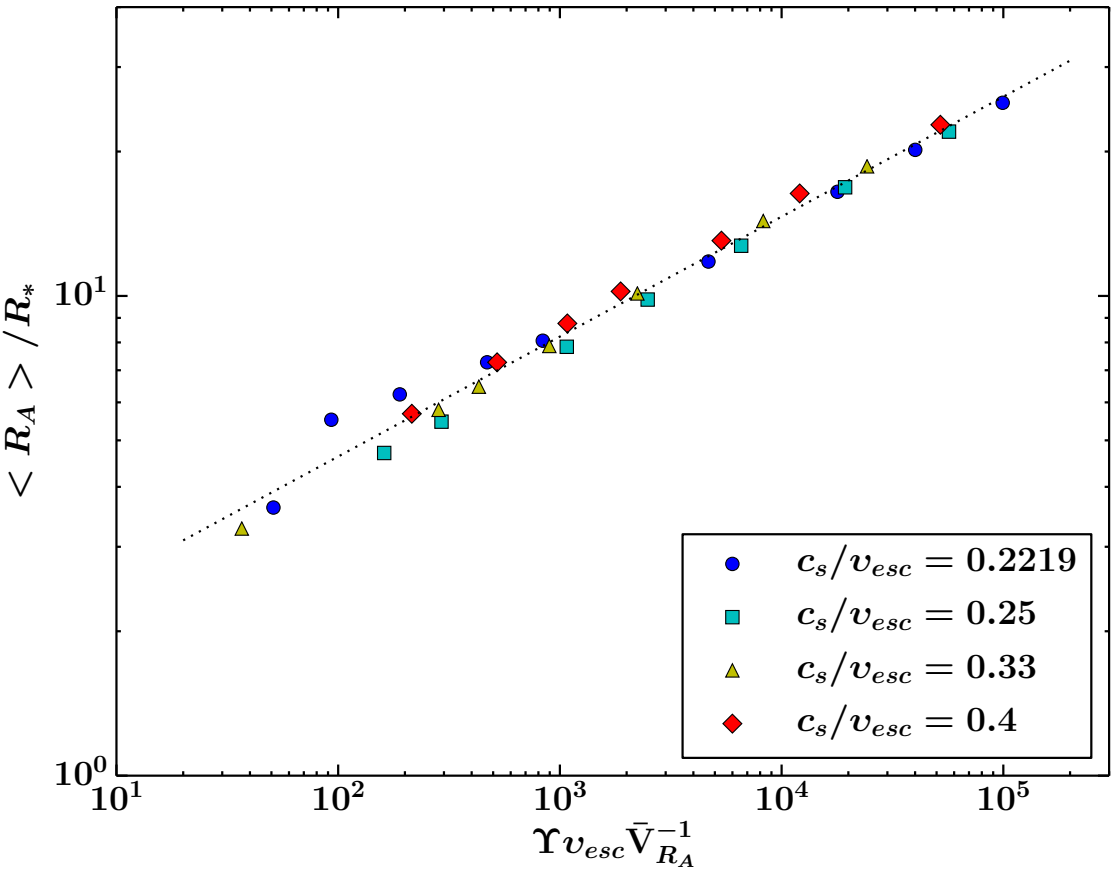

Figure 3.11: $< R_A > /R_*$ versus the quantity $\Upsilon v_{esc} \bar{V}_{R_A}^{-1}$ for all the simulations. Colors/symbols have the same meaning as in Figure 3.2. All the data points are fitted by a single coefficient K_l, and the fitting line (dotted line) has a slope (or power-law index) of 1/4, according to equation (3.34). The small spread of the data points, observed in this braking law is primarily due to variations in the ratio of the Alfvén radius to the open-field radius (see also eq. 3.32 and Figure 3.12).

An interesting characteristic of equation (3.31) is that it explains the fitting constants of equation (3.18) in terms of other fitting constants, and consists of an analytic expression for the effective Alfvén radius. This formalism is independent of the temperature of the flow (but requires a known wind acceleration profile), the geometry of the magnetic field, and predicts the torque exerted on the star for any value of Υ_{open}, for a given rotation rate (in the slow-rotator regime) and polytropic index ($\gamma = 1.05$ in this study). Comparing equations (3.18) and (3.31), we identify that $K_o \sim (K_c^2 K_q^{-1})^{1/(2+q)}$ and $m_o \sim 1/(2+q)$. The predicted values of m_o for each temperature, are listed in the 7^{th} column in Table 3.3. Clearly m_o and K_o stongly depend on the accelaration profile of the wind, here parametrized with K_q and q.

3.5.3 Semi-analytic Model for Alfvén Radius versus Υ

The formalism given by equation (3.26) provides an excellent fit, in terms of predicting the torque-averaged Alfvén radius from parameter Υ_{open}, for a given wind acceleration. However, in real wind cases, the amount of open magnetic flux is a quantity that is not observable, and can only be predicted (e.g., Vidotto et al. 2014b; Réville et al. 2015b; See et al. 2017). Therefore, in this section, we aim at extracting trends for the braking torque based on Υ, which depends on the surface magnetic field strength (or surface magnetic flux).

Such trends can be obtained analytically, by combining equations (3.22), (3.23), (3.24), and also by using the definition for Υ, (see equation (3.11)), which yields

$$\left(\frac{R_A}{R_*}\right)^{2l+2}\left(\frac{R_o}{R_A}\right)^{2l} = \Upsilon\frac{\upsilon_{esc}}{\upsilon(R_A)}. \tag{3.32}$$

Figure 3.11 shows the effective Alfvén radius versus the Υ-based quantity, $\Upsilon\upsilon_{esc}\bar{\mathrm{V}}_{R_A}^{-1}$, as it is suggested by equation (3.32). Once more, all the details regarding the acceleration of the flow have been contained in the dimensionless term, $\upsilon_{esc}/\bar{\mathrm{V}}_{R_A}$, and as a result all the simulations lie close to a single power law. The latter suggests that the ratio R_o/R_A, in equation (3.32), can be assumed to have a constant value for all the simulations of this study. Thus, equation (3.32) can solved for R_A/R_* and we get

$$\frac{R_A}{R_*} \propto \left(\Upsilon\frac{\upsilon_{esc}}{\upsilon(R_A)}\right)^{1/(2l+2)}. \tag{3.33}$$

The power $1/(2l+2)$ in equation (3.33) only depends on the geometry of the field (or l). Hence, the scaling law (3.33) should apply to more complex single field geometries (e.g., quadrupole, octupole) as well, but for our case, with a dipole field ($l = 1$), the slope, of the single line formed by the data points in Figure 3.11, is equal to 1/4. Following this simplified analysis, we fit the data in Figure 3.11 with

$$\frac{< R_A >}{R_*} = K_l\left(\Upsilon\frac{\upsilon_{esc}}{\bar{\mathrm{V}}_{R_A}}\right)^{1/4}, \tag{3.34}$$

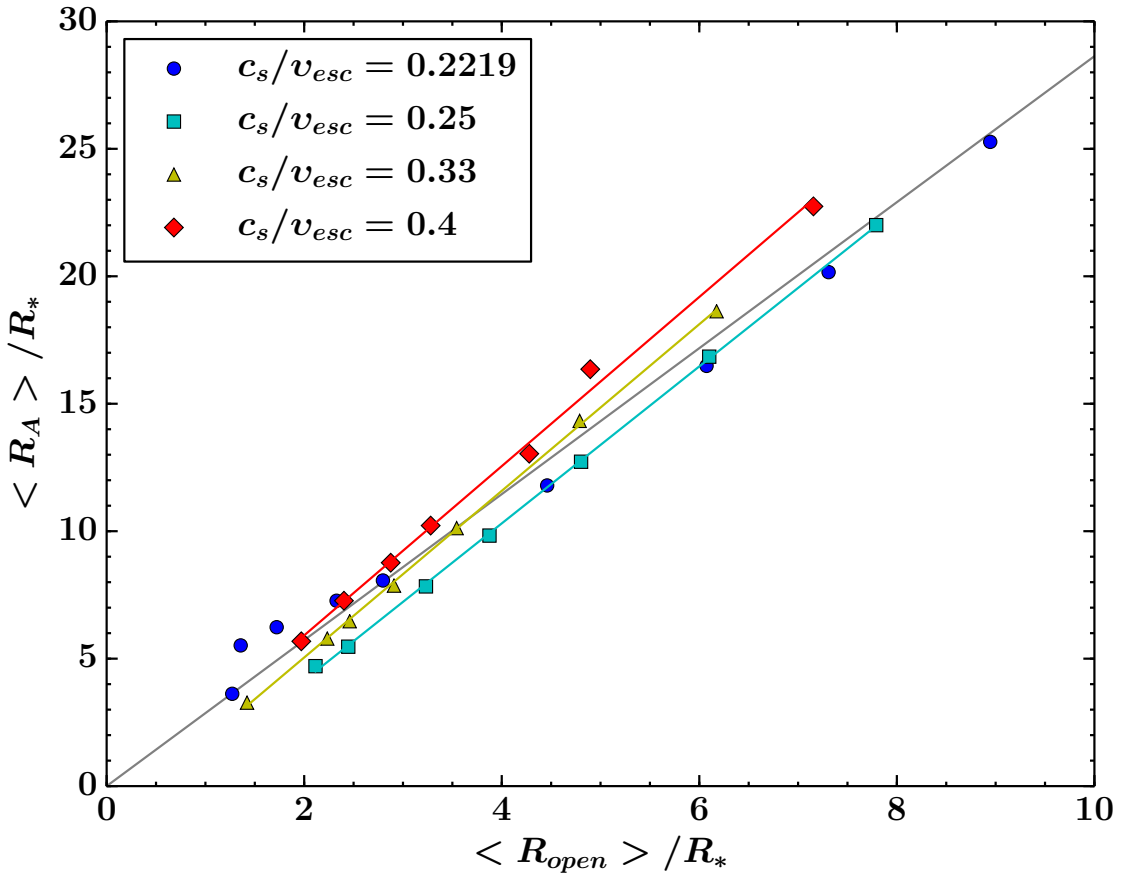

Figure 3.12: Torque-averaged Alfvén radius, $< R_A > /R_*$, versus the normalized open-field radius, $< R_o > /R_*$. Color/symbols are the same as in Figure 3.2. The grey line shows a linear function that represents all the data, and gives $< R_A > / < R_o >= 2.86$. Cyan, yellow, and red solid lines depict linear functions as well, as an example, to show how $< R_A > / < R_o >$ systematically varies for each temperature.

and K_l is introduced as the only fitting constant. The best-fit value of K_l is

$$K_l = 1.46 \pm 0.02. \tag{3.35}$$

Fitting constant K_l includes any factors, due to the multidimensionality of our simulations, and most important, the comparison between equations (3.32) and (3.34) suggests that K_l also includes the dimensionless ratio of the Alfvén radius to the open-field radius of the wind, R_A/R_o. Furthermore, the fact that all the data points do not precisely lie along the single power law in Figure 3.11, implies that the term R_A/R_o is not constant for all the simulations and exhibits a dependence on the flow temperature.

A coherent way to estimate the open-field radius (i.e., the radial distance in which

the wind's thermal and ram pressure overpower the magnetic field pressure, and as a result the unsigned magnetic flux becomes constant as a function of radial distance) for all our simulations, is to define $< R_o > /R_*$ as

$$\left(\frac{< R_o >}{R_*}\right)^l \equiv \frac{\Phi_*}{\Phi_{open}}. \tag{3.36}$$

In other words, equation (3.36) gives the radial distance in which the function, $\Phi(r)/\Phi_* = (R_*/r)^l$, intersects the line, $\Phi(r)/\Phi_* = \Phi_{open}/\Phi_* = \text{const.}$, and applies for any given single magnetic field geometry.

In Figure 3.12, we present the normalized open-field radius, $< R_o > /R_*$, versus the torque-averaged Alfvén radius, $< R_A > /R_*$, and the plot shows that all the simulations have approximately the same ratio, $< R_A > / < R_o >$. This feature explains why equation (3.34) successfully represents the data. Assuming a linear scaling between $< R_A >$ and $< R_o >$, yields $< R_A > / < R_o > \approx 2.86$. A closer inspection reveals a range in $< R_A > / < R_o >$ between 2.23 and 4.07, that will produce a scatter in Figure 3.11 only as the square root of this ratio, with the most extreme deviation from the linear function (grey line) to be 20%. In fact, $< R_A > / < R_o >$ systematically changes, which explains the systematic scatter in Figure 3.11 as due to small differences in $< R_A > / < R_o >$ for each temperature. The general trend in Figure 3.12, is that $< R_A > / < R_o >$ increases for an increasing flow temperature (see solid cyan, yellow, and red lines), though that is not the case for simulations with $c_s/v_{esc} = 0.2219$, for which the data points exhibit a peculiar behavior. Lastly, $< R_A > / < R_o >$ should exhibit a dependence on the geometry of the field, and in particular, the expected trend is that for an increasing complexity in the field geometry, this ratio reduces because the magnetic field strength decays faster with radial distance (see e.g., Réville et al. 2015a; Finley and Matt 2017).

Equation (3.34) can be further expanded by substituting $\bar{\mathrm{V}}_{R_A}$ with the velocity law, given by equation (3.28), which yields

$$\frac{< R_A >}{R_*} = \left(\frac{K_l^4}{K_q}\Upsilon\right)^{1/(4+q)}. \tag{3.37}$$

Equation (3.37) explains the fitting constants of equation (3.15) in terms of other fitting

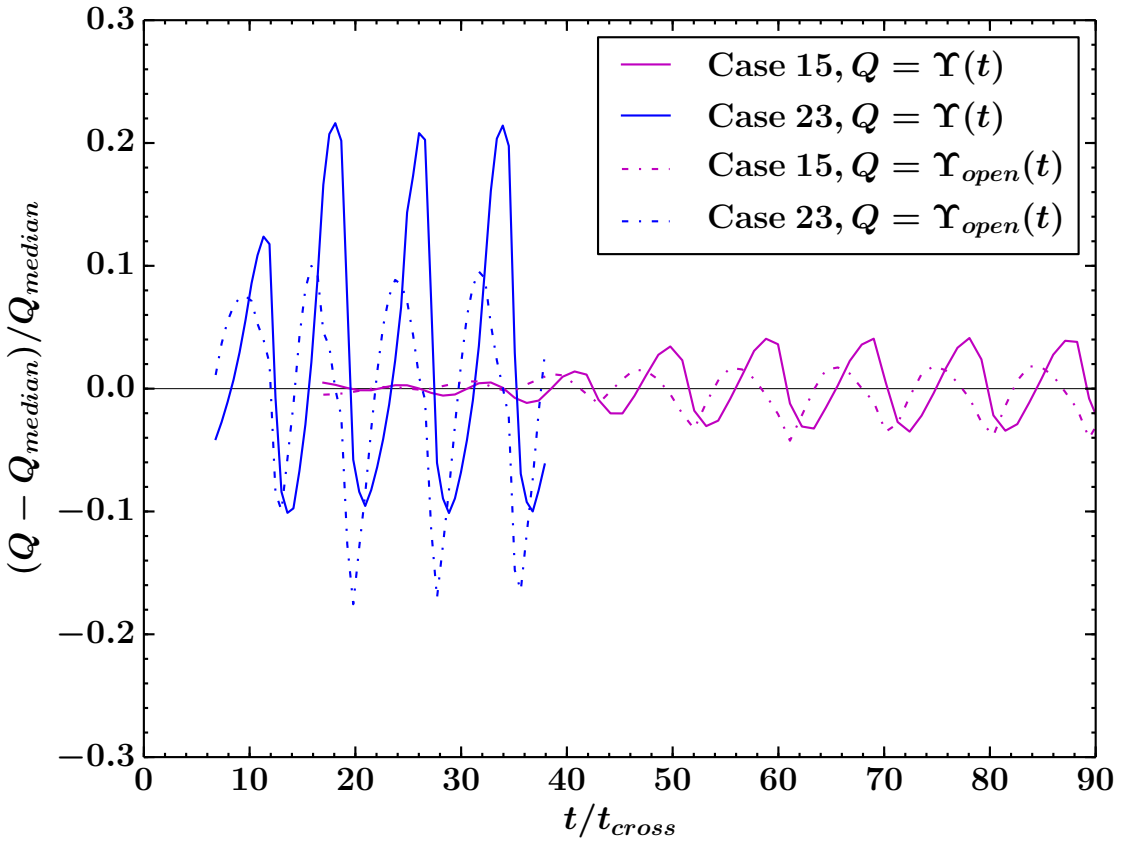

Figure 3.13: Variations of $\Upsilon(t)$ and $\Upsilon_{open}(t)$ relative to median values of Υ and Υ_{open}, respectively, versus number of crossing times t/t_{cross}. Two cases are shown, represented by the magenta lines (case 15) and the blue lines (case 23). The solid lines show the variations in parameter Υ and the dotted-dashed lines show the variations Υ_{open}, respectively.

constants, and represents an analytic formula of the torque-averaged Alfvén radius for any value of parameter Υ, for any known wind acceleration profile (known values of K_q and q), for a dipolar field geometry, for a star that is a slow rotator, and for $\gamma = 1.05$.

Finally, equation (3.37) can work as a proxy in order to extract predictions for the values of K_s and m_s (see eq. 3.15), that determine the simple power laws in Figure 3.7. It is expected that $K_s \sim (K_l^4/K_q)^{1/(4+q)}$ and $m_s \sim 1/(4+q)$, see for example the 4^{th} column in Table 3.3, for the predicted values of m_s, for each flow temperature. Undoubtedly, the reason for the differences in the four different power laws in figure 3.7, is related to the acceleration of the flow, which depends on the stellar coronal temperature.

3.6 Periodic wind solutions

Each simulation is stopped when the solution relaxes to a steady state. About half of our wind solutions show a steady nature to some tolerance (see below), and the rest are periodic (or quasi-steady state) due to magnetic reconnections (due to numerical diffusion) at the neutral point (or cusp) located at the equatorial region of each simulation. As a consequence, a perfect steady-state solution cannot be obtained. Similar features has been noted by Washimi and Shibata (1993), who found that the neutral point has a non-steady behavior.

Due to this non-stationary nature of the equatorial region in some of our simulations, the fluxes passing through spherical surfaces, within our computational domain, are not constant in radius and time. As a result, parameters Υ, Υ_{open}, and the effective Alfvén radius, $< R_A > /R_*$, show a dependence in both radius and time (whereas they should be constant for an ideal and steady-state MHD wind). However, the fluctuations of $\dot{M}_w$, τ_w, and Φ_{open}, are well behaved and oscillatory, and the amplitude of the oscillations is constant in both r and t. In order to derive single values for $\dot{M}_w$, τ_w, and Φ_{open}, we used their median values in both r (as dicsussed in §3.4.1), and t, where the value of a quantity was taken to be its median value after the initial transient phase of the simulation (i.e., typically after $\sim$ 10 crossing times). These global values of $\dot{M}_w$, τ_w and Φ_{open}, are then used to calculate Υ, Υ_{open}, and $< R_A > R_*$, for each case.

The relative errors of the time-varying $\Upsilon(t)$ and $\Upsilon_{open}(t)$ to the global values of Υ and Υ_{open} are shown in Figure 3.13, as a function of number of wind crossing times, t/t_{cross}, (where $t_{cross} = 50R_*/v_{esc}$). The relative error of a given quantity to its median value is taken to be $(Q - Q_{median})/Q_{median}$, where Q is Υ or Υ_{open}. Two cases are presented [i.e., case 15 (23) has the magenta (blue) line]. The solid lines correspond to the relative errors in $\Upsilon(t)$, and the dotted-dashed lines show the relative errors in $\Upsilon_{open}(t)$. From Figure 3.13 it is clear, that $\Upsilon(t)$ and $\Upsilon_{open}(t)$ fluctuate in time, and furthermore are well-behaved functions of t. The variations in $< R_A > /R_*$ are smaller in magnitude, compared to the variations seen in Υ and Υ_{open}, for a given wind solution. For example, case 23, shown in Figure 3.13, exhibit variations in $< R_A > /R_*$ of about 2% (compared to the range of variations in Υ shown in the figure).

Overall, for this study of 30 wind solutions, we obtained 16 steady-state wind solutions, meaning that the fluctuations in quantity Υ, are not noticeable or less than 2%. 7 wind solutions show variations in the range between 2% and 10%, and in 7 simulations the variations in $\Upsilon(t)$ are between 10% and 30%. Additionally, we did not see any systematic difference in the trends shown in this study between the steady and periodic cases.

3.7 Accuracy of the Numerical Solutions

For ideal, axisymmetric, and steady-state, MHD outflows, there are five scalar quantitities (i.e., derivative of the stream function or mass flux per magnetic flux, Bernoulli or energy function, entropy, specific angular momentum on a given stream function, effective rotation rate of the field lines) that are constants of motion along each field line (e.g., Heinemann and Olbert 1978; Lovelace et al. 1986; Mestel 1999; Ustyugova et al. 1999; Keppens and Goedbloed 2000). In order to examine the accuracy of each of our numerical solutions, we check that each of the above quantities are conserved within some tolerance. As shown by Zanni and Ferreira (2009) a difficult quantity to conserve, and critical in order to measure accurate stellar torques, is the effective rotation rate of the field lines, Ω_{eff}. Solving equation (3.9) for Ω_*, the effective rotation of the field lines is defined as

$$\Omega_{eff}(\Psi) \equiv \frac{1}{r\sin\theta}\left(v_\phi - \frac{v_p}{B_p}B_\phi\right), \tag{3.38}$$

where Ψ is the magnetic stream function, given in spherical coordinates as $\Psi = r\sin\theta A$, where r is the spherical radius, A is the scalar magnetic field potential (i.e., $\mathbf{B}_p = \nabla \times A\hat{\phi}$). Each field line has a unique value of Ψ. Since the stream function is a function of a scalar potential, Ψ can be determined everywhere by specifying its value at a single point. We choose that Ψ is zero at the pole, on the stellar surface (i.e., $\Psi = 0$ for $\theta = 0$ and $r = R_*$), and as a result the first polar field line will have a Ψ-value of zero.

In the ideal MHD regime, for any axisymmetric and steady-state wind solution, equation (3.9) should hold throughout the numerical domain, and the plasma, which flows along the field lines, should rotate such that the ratio Ω_{eff}/Ω_* is equal to unity. Any deviations from the value of unity occur due to numerical diffusion and non-stationary wind

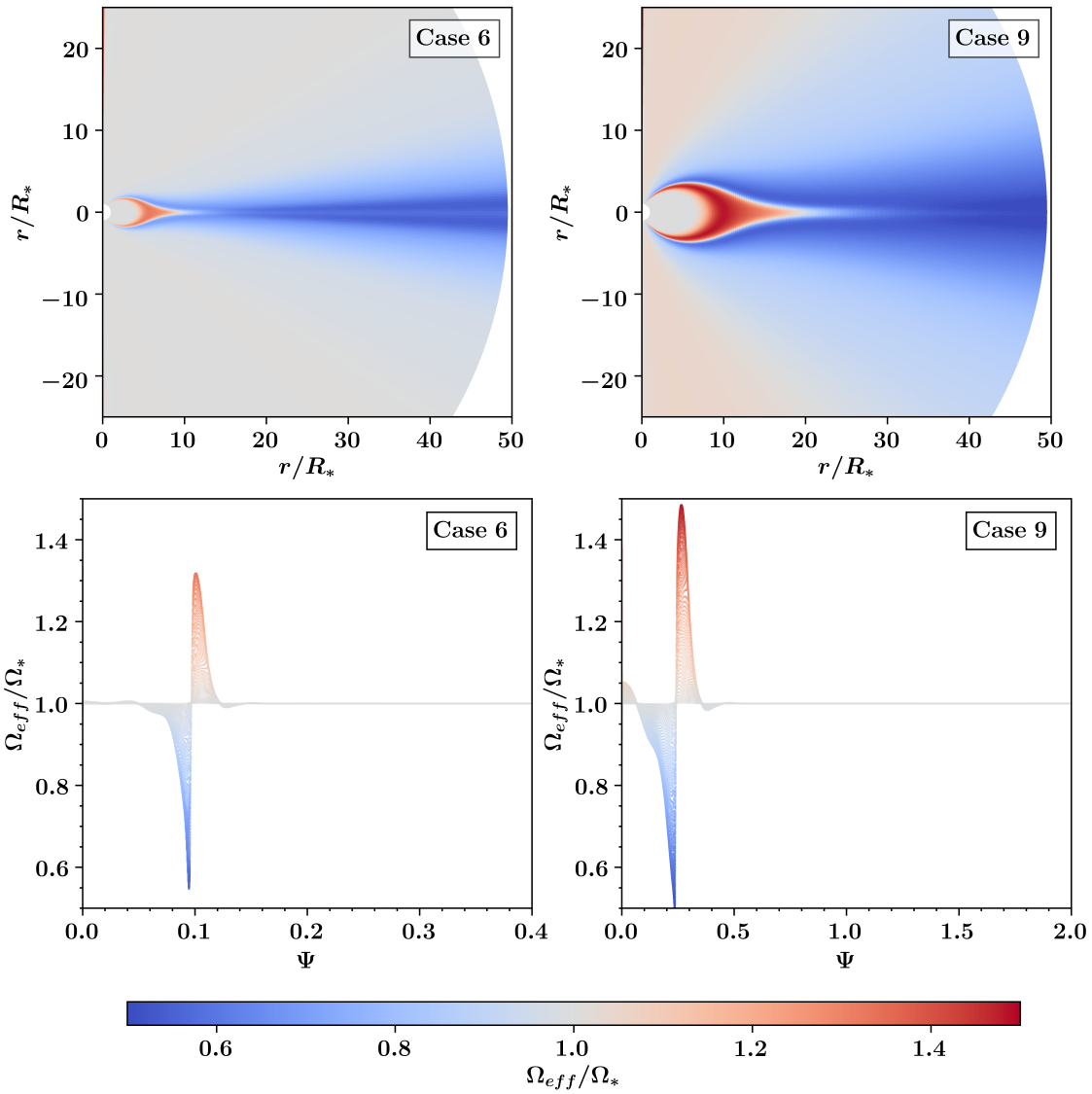

Figure 3.14: Normalized effective rotation of field lines for two cases of the study. In the top panels, Ω_{eff}/Ω_* is visualized as a 2D color-scale map. In the bottom panels, Ω_{eff}/Ω_* is plotted versus the magnetic stream function Ψ. In the bottom plots, each plotted point represents a grid cell in the computational grid and each field line is associated with a unique value of Ψ. The color scale is the same for each plot. By design, the polar fieldline has a value of $\Psi = 0$. The open-field region has a Ψ that varies between 0 and 0.1 for case 6 (bottom left panel), and between 0 and 0.25 for case 9 (bottom right panel).

solutions. One of the crucial ingredients to achieve correct rotation for the matter around the star are the boundary conditions on υ_ϕ and B_ϕ, imposed on the inner boundary (i.e., stellar surface) of the computational domain, as pointed out in Zanni and Ferreira (2009). For our simulations, the toroidal speed of the plasma is enforced in the stellar boundary via equation (3.9) and B_ϕ is linearly extrapolated (i.e., $\partial B_\phi/\partial r = \text{const.}$) into the ghost zones, a boundary condition that works well for the current stellar-wind numerical setup (for a more detailed discussion on different boundary conditions on B_ϕ see also Zanni and Ferreira 2009).

In Figure 3.14, the behavior of the normalized effective rotation rate is presented as a 2D-color-scale plot (top panels), and in a Ω_{eff}/Ω_*-versus-Ψ plot (bottom panels), for two numerical wind solutions of the study. The two cases shown are, one that is typical (case 6), and one (case 9) that exhibits among the largest errors in the conservation of Ω_{eff}. In the top panels of Figure 3.14, the regions in the plots coloured with grey correspond to an Ω_{eff}/Ω_* that is equal to unity. The blue and red regions correspond to $\Omega_{eff}/\Omega_* < 1$ and $\Omega_{eff}/\Omega_* > 1$, respectively. For example, in case 6, we identify that Ω_{eff}/Ω_* is not conserved along field lines located at mid-latitudes, adjacent to the dead zone, where steep gradients of υ_{pol} and B_ϕ enhance the numerical diffusion. To be more specific, as it was mentioned above, in any perfect ideal MHD, axisymmetric, and steady-state solution, the outflow (with $\upsilon_p \neq 0$ and $B_\phi \neq 0$) should always subrotate, due to the magnetic term (second term) on the right-hand side of equation (3.9), and the static dead zone (with $\upsilon_p = 0$, which also leads to $B_\phi = 0$) should corotate with the star. For such a solution the rotational speed of the plasma, Ω_{eff} (see equation (3.38)), normalized to the stellar rotation speed Ω_*, should always be equal to unity, and the points in the bottom panels of Figure 3.14 should lie on a line $\Omega_{eff}(\Psi)/\Omega_* = 1$. Therefore, the behavior of Ω_{eff}/Ω_* in Figure 3.14 can be understood as a consequence of the accuracy of the numerical scheme (see e.g., Keppens and Goedbloed 2000), which determines the amount of numerical diffusion introduced in the simulations. This scheme produces a smoother (or flatter) transition region between the wind region and the dead zone. As a result some outflow field lines adjacent to the dead zone rotate slower, compared to the expected rotation rate of the field lines in the wind region given by equation (3.38) and thus, $\Omega_{eff}/\Omega_* < 1$. Furthermore, some field lines inside the dead zone rotate faster (i.e.,

$\Omega_{eff}/\Omega_* > 1$) and the dead zone does not perfectly corotate with the star. A measure of how Ω_{eff}/Ω_* deviates from unity, for these two simulations, is given in the bottom panels of Figure 3.14. Each point in the bottom panels represent a grid cell, within our domain, and every value of Ψ corresponds to a different field line. Values of Ψ from 0 to about 0.1 (case 6), and from 0 to about 0.25 (case 9) correspond to open field lines, in which the wind flows outwards, and the rest of Ψ values represent closed magnetic loops. For case 6, we observe that some open field lines sub-rotate (up to 40%), and some closed field lines over-rotate (up to 30%). A comparison of Ω_{eff}/Ω_* between the two cases reveals that the errors for case 9 (and cases with a high wind magnetization) are shifted to the left because such simulations produce less fractional open flux. For these cases the dead zones are more extended, cover most of the stellar surface, and as a result most of the open-field lines are influenced by numerical errors. This can be easily seen in top right panel in which the grey-shaded regions significantly decrease compared to typical cases with median or low values of Υ (top left panel). Futhermore, the amplitude of the errors becomes bigger in case 9, (see bottom left and right panel) as a consequence of a wind that is more magnetized and due to this faster (i.e., even steeper gradients of υ_{pol} and B_ϕ). In other words, numerical errors are more significant in simulations with high wind magnetization.

One way to reduce these non-ideal features is to increase the resolution of the computational domain. For example, our resolution studies (not shown) indicate that by doubling the number of cells in the θ direction, numerical errors in Ω_{eff}/Ω_* decrease, but the torque-averaged $< R_A > /R_*$, for most cases increase only by a few precent. Bigger differences in the values of $< R_A > /R_*$, due to a higher grid resolution, are observed in simulations with Υ above 10^4, but even for these cases $< R_A > /R_*$ does not increase by more than 10%. These systematic errors suggest that a more accurate numerical treatment would lead to slightly steeper power laws in the trends shown in Figures 3.7 - 3.9 and 3.11.

3.8 Towards Predicting Torque for any Temperature

In this section we present empirical relations that predict the fitting constants K_q, q, used to prescribe the wind speed at the Alfvén radius (see eq. 3.28), as functions of the

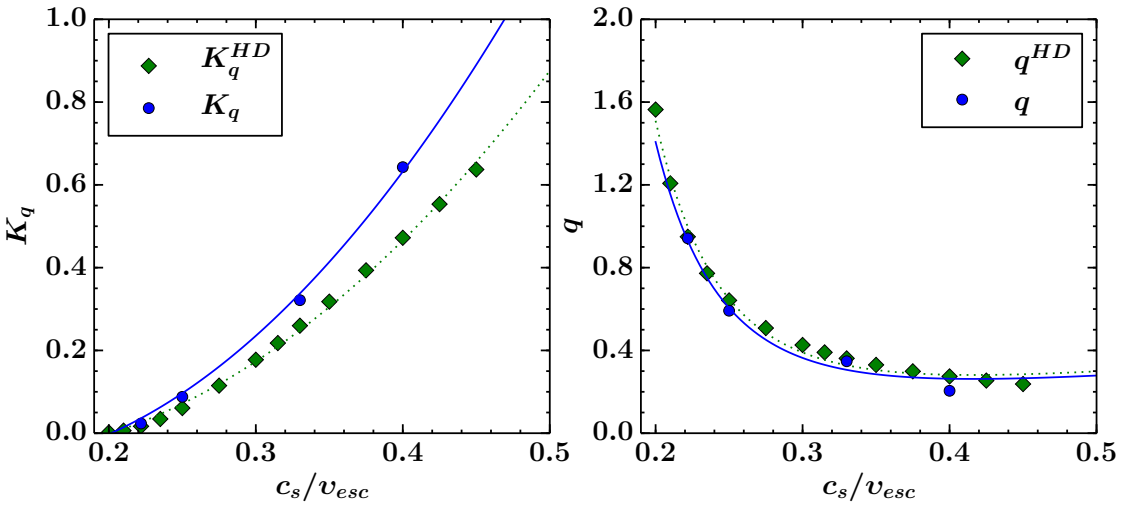

Figure 3.15: Fitting constants K_q (left panel), q (right panel) of equation (3.28) versus parameter c_s/v_{esc}. The blue circles correspond to the values of K_q and q from the velocity laws presented in Figure 3.10. The green diamonds correspond to the fitting constants K_q^{HD} and q^{HD}, which have been obtained from 1D, HD wind speed profiles. The dotted lines fit the green data points, according to equations (3.39) and (3.40). The blue solid lines show the fitting functions (eq. 3.41 and 3.42) for K_q and q, respectively.

input parameter c_s/v_{esc}. K_q and q are needed in order to estimate the torque-averaged Alfvén radius (see eqs. 3.31, 3.37), and since our study investigated only four different flow temperatures, and their corresponing wind acceleration profiles, our aim is to provide a practical method that could give K_q and q over a larger, and continuous range of c_s/v_{esc}. This method should work for any continuous range of c_s/v_{esc}, for polytropic winds with $\gamma = 1.05$. A different value of γ, for a fixed value of c_s/v_{esc}, significantly affects the flow velocity and acceleration profile (see e.g., Figures 4.9 and 4.10 in chapter 4). Therefore the prescriptions for K_q and q that are given below cannot be applied to every polytropic model with different values of both γ and c_s/v_{esc}. However the method that is introduced below can be generalized for other polytropic winds, but we do not test that here.

The values of K_q and q versus parameter c_s/v_{esc} are shown in Figure 3.15 for our four temperatures (blue circles). All the values of q are positive, in the range between zero and unity. There is no physical reasoning for not getting wind solutions with values of q, such as $q > 1$, but a $q = 0$ is the lower limit for any accelerating flow. Regardless of the obvious trends in Figure 3.15, (i.e., K_q and q monotonically increase and decrease with an increasing c_s/v_{esc}, respectively), any function that could possibly represent (or fit) these data points, would be rather biased due to the small number of data points (only four). Therefore, in order to construct functions that can fit the data in Figure 3.15, we

employ the following approach. In Figure 3.10, we demonstrated that the $\bar{V}_{R_A}/v_{esc}$-versus-$< R_A > /R_*$ data points exhibit a behavior similar to the shape of the radial-velocity profiles (i.e., v_r/v_{esc} versus r/R_*) of the 1D, hydrodynamic, winds shown in Figures 3.1 and 3.10. Based on that, one can infer what $\bar{V}_{R_A}$ would be for any given flow temperature (or any given value of c_s/v_{esc}) from polytropic, Parker's winds of that value of c_s/v_{esc}. Hence, we produce 14 Parker's wind models, in which parameter c_s/v_{esc} varies between 0.2 and 0.45. The velocity profiles of these winds are functions of radial distance from the surface of the star. Then, we treat any radial distance, of these profiles, as a potential Alfvén radius, and its corresponding flow velocity as the mean speed of the outflow at the Alfvén radius (i.e., $\bar{V}_{R_A}$). Following equation (3.28), we fit these HD wind speed profiles, assuming that the flow speed is a power law in radial distance (i.e., $v(r) \propto K_q^{HD} r^{q^{HD}}$). Since for the entire study the minimum and maximun value of $< R_A > /R_*$ is $3.27R_*$ and $25.3R_*$, respectively, the HD wind speed profiles are fitted for radial distances that range between $4R_*$ and $25R_*$. We obtain 14 new pairs of the dimensionless fitting constants K_q^{HD} and q^{HD}, also shown in figure 3.15 as green diamonds. The values of K_q^{HD} and q^{HD} can be slightly influenced by considering a different range in radii, in order to fit these HD wind speed profiles. The following empirical functions can fit the new data points (i.e., K_q^{HD} and q^{HD})

$$K_q^{HD} = \alpha_1 (c_s/v_{esc})^2 + \beta_1 (c_s/v_{esc}), \tag{3.39}$$

$$q^{HD} = \alpha_2 (c_s/v_{esc})^{\nu_2} + \beta_2 (c_s/v_{esc}), \tag{3.40}$$

where α_1, α_2, β_1, β_2, and ν_2 are fitting coefficients. The best-fit values are $\alpha_1 = 5.87$, $\beta_1 = -1.18$, for equation (3.39), and $\alpha_2 = 0.000979$, $\nu_2 = -4.51$, $\beta_2 = 0.553$, for equation (3.40). Equations (3.39) and (3.40) are represented in both panels of Figure 3.15 by the green dotted curves.

Equations (3.39) and (3.40) can represent the 4 data points (blue circles) in Figure 3.15, just by including a multiplicity factor. Indeed the blue, solid lines in figure 3.15 show

that the data of K_q and q can be fitted by functions in the form of

$$K_q = D_1[\alpha_1(c_s/\upsilon_{esc})^2 + \beta_1(c_s/\upsilon_{esc})], \tag{3.41}$$

$$q = D_2[\alpha_2(c_s/\upsilon_{esc})^{\nu_2} + \beta_2(c_s/\upsilon_{esc})], \tag{3.42}$$

where again D_1, D_2 are fitting constants, and their best-fit values are found to be is $D_1 = 1.36$, and $D_2 = 0.932$. In conclusion, equations (3.41) and (3.42) can successfully predict the values of dimensionless fitting constants K_q and q for any value of parameter c_s/υ_{esc} in the range between 0.2 and 0.45, for thermally-driven winds from slow-rotating stars, with dipolar fields, and a fixed value of polytropic index equal to 1.05.

In general, for any polytropic model, c_s/υ_{esc} and γ are free parameters. There is a constraint that the value of c_s/υ_{esc} must correspond to a temperature at the base of the corona of $\sim 10^6$ K, but there is no restriction on the exact value of the polytropic index, which also determines the energetics of the flow (as long as $\gamma < 3/2$ in order to have an accelerating flow). Typical values of coronal temperatures and γ that have been used in solar-wind studies are $T_{cor} = 1 - 2 \times 10^6$ K and $\gamma = 1 - 1.13$, respectively (see e.g., Parker 1963; Mikić et al. 1999; Keppens and Goedbloed 2000, and references therein), which are consistent with solar-corona/wind observations (see e.g., Feldman et al. 2005). In addition, studies (Réville et al. 2016a; Finley and Matt 2017, 2018) show that more complex field geometries (as long as there is a dipolar component, even in non-axisymmetric cases) do not have a major effect on the fitting laws in the R_A-versus-Υ_{open} space. Note that, K_q and q also appear implicitly in the fitting constants K_o and m_o (see discussion in section 3.5.2). Therefore, assuming that the polytopic approximation and the value of $\gamma = 1.05$ is valid for coronal winds from low-mass stars, the prescriptions (3.41) and (3.42) can provide the values of K_q and q for the range of c_s/υ_{esc} considered here. However, they are limited to slow rotators (i.e., the stellar-spin rates must be less than the 10% of the brake-up speed, Matt et al. 2012b).

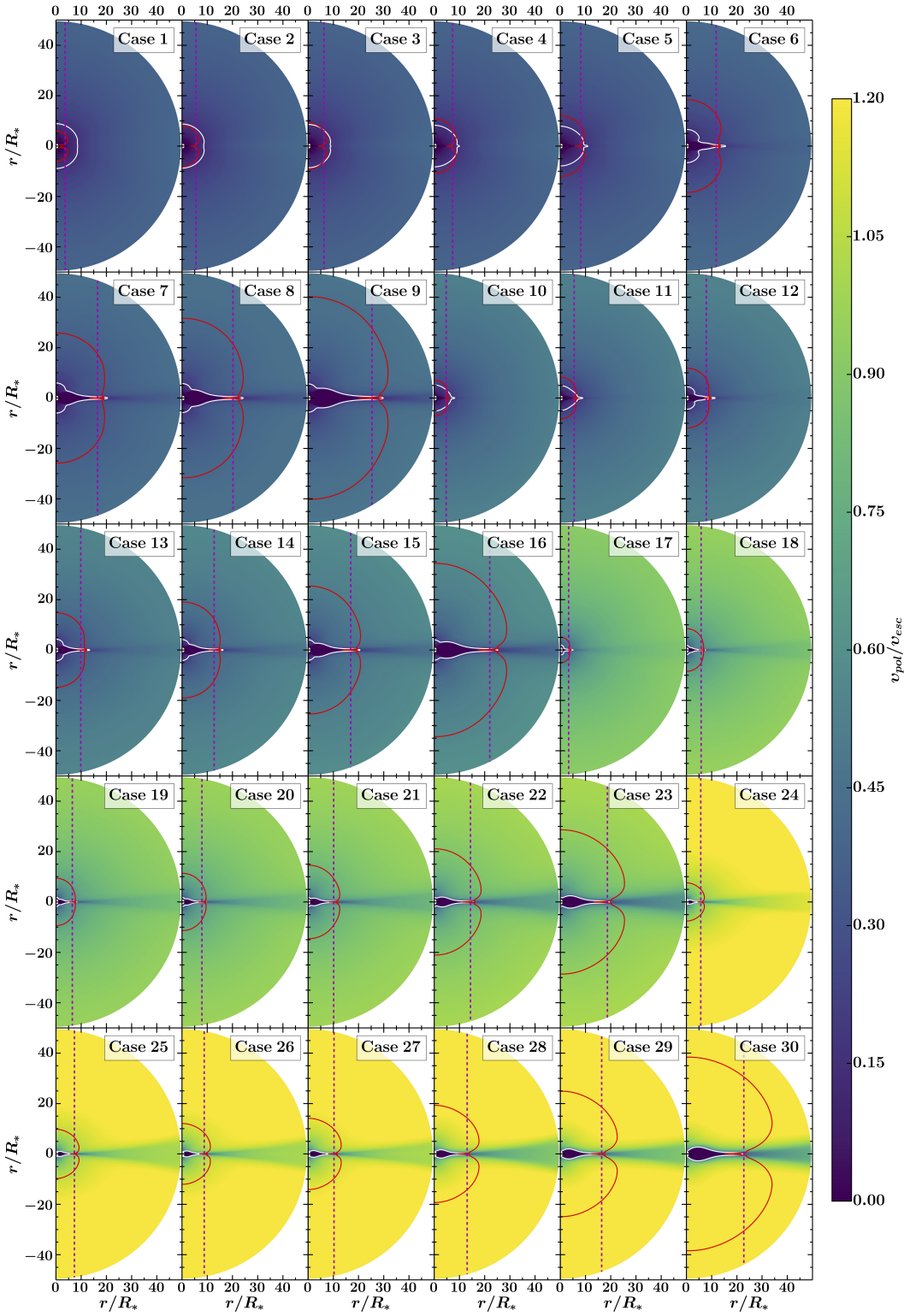

Figure 3.16: Wind poloidal velocity colormaps of the entire study. White and red lines represent the sonic, and Alfvén surfaces respectively. The magenta dashed lines show the location of torque-averaged Alfvén radius (or effective lever arm). Simulations 1 to 9, 10 to 16, 17 to 23, 24 to 30, have respectively $c_s/v_{esc} = 0.2219, 0.25, 0.33, 0.4$.

3.9 Complete Grid of Simulations

Figure 3.16 presents color-scale plots of the wind's poloidal velocity, for all the numerical solutions of this study. Cases 1 to 9, 10 to 16, 17 to 23, 24 to 30, have respectively $c_s/v_{esc} = 0.2219, 0.25, 0.33, 0.4$. Each panel in figure 3.16 shows the full computational grid, the location and the shape of the wind's critical surfaces. The sonic and Alfvén surfaces are depicted with white and red solid lines, respectively. The magenta dashed lines show the effective lever arm, $< R_A > /R_*$, that brakes the stellar rotation. A different coronal temperature (primarily) and a higher wind magnetization (to a lesser extent) affects the outflow speed and acceleration profile. This feature can be seen by the changes in the color scale of each panel. Overall, for a given value of the wind magnetization, Υ, a hotter wind reaches the Alfvén surface in a shorter disctance from the stellar surface, the size of the lever arm decreases, and as a result magnetic torque is reduced.

3.10 Summary and Conclusions

Employing 2.5D, ideal MHD, axisymmetric numerical simualtions, we provide a systematic study on how the thermodynamic conditions (i.e., flow temperature for the current work), in stellar coronae of cool stars, can influence the losses of stellar angular momentum due to magnetized winds. Our parameter space considers polytropic flows, modified with rotation and magnetic fields, includes 30 steady-state wind solutions (see section 3.9 for color scale plots of the complete simulation grid), and quantifies the braking torque for 4 different coronal temperatures, over a wide range of magnetic field strengths, for slow rotators, for dipolar fields, and for a fixed polytropic index ($\gamma = 1.05$). The following points summarize the main conclusions in this work:

1. For a given value of wind magnetization, Υ, (or a given value of Υ_{open}), a hotter wind is faster, reaches the Alfvén speed closer to the star and, as a consequence, the torque exerted on the surface of the star decreases. Our conclusion agrees qualitatively with the results from Mestel and Spruit (1987), who first pointed out the effects of the wind thermodyanmics on the magnetic braking of low-mass stars.

2. We present two formulae that estimate the size of the torque-averaged Alfvén radius:

one that depends on parameter Υ, which is based on stellar-surface parameters, and a second one that depends on Υ_{open}, which is based on the amount of open magnetic flux. Each formulation gives a simple power law for each coronal temperature. By substituting equation (3.15) into equation (3.2), the stellar angular-mometum-loss rate due to a magnetized wind is

$$\tau_w = K_s^2 \Omega_* \upsilon_{esc}^{-2m_s} \dot{M}_w^{1-2m_s} R_*^{2+4m_s} B_*^{4m_s}, \tag{3.43}$$

which is useful if the dipole field strength at the stellar surface is known. Similarly, by combining equations (3.2) and (3.18), we have

$$\tau_w = K_o^2 \Omega_* \upsilon_{esc}^{-2m_o} \dot{M}_w^{1-2m_o} R_*^{2-4m_o} \Phi_{open}^{4m_o}, \tag{3.44}$$

which is useful if the amount of the total open magnetic flux is known. The above relations can be used for studies of the rotational evolution of cool stars, and predict the torque on stars with axisymmetric dipolar magnetic fields, that are slow rotators, and exhibit coronal winds with $\gamma = 1.05$. Four different flow temperatures were studied, and the values of fitting constants, K_s, m_s, K_o, m_o for each temperature, can be found in Table 3.3.

3. Using a simplified analysis (in §3.5), we identified that the wind acceleration profile is a key factor that determines how the torque scales with parameter Υ or Υ_{open}. We found (in Figures 3.9 and 3.11) that by including the dimensionless velocity term, $\upsilon_{esc}/\bar{\mathrm{V}}_{R_A}$, ($\bar{\mathrm{V}}_{R_A}$ is the wind's mean speed at the Alfvén surface), in each of the two torque formulae, all the simulation data collapse into a unique power law, independent of the flow temperature. In other words, we propose that a key term that needs to be included in stellar-torque prescriptions when one considers stars with different coronal conditions (and consequently different wind acceleration profiles) is the average wind speed at the Alfvén surface, *whatever heats and expands the outflow*. This conclusion should be independent of the actual wind temperature or details of how the wind is driven, since the angular momentum flux primarily depends on the flow velocity, mass density, and the magnetic field properties (see

e.g., eqns 3.13 and 3.14).

4. By considering a power-law dependence of $\bar{V}_{R_A}$ (i.e., wind's mean speed at the Alfvén surface) in $< R_A > /R_*$, the torque-averaged Alfvén radius can be expressed with an analytic form (see eqs 3.31, 3.37), for a well-approximated (or known) wind acceleration profile. Equations (3.2), (3.37), and (3.2), (3.31), then yield respectively,

$$\tau_w = \frac{K_l^{8/(4+q)}}{K_q^{2/(4+q)}} \Omega_* \upsilon_{esc}^{-2/(4+q)} \dot{M}_w^{(2+q)/(4+q)} R_*^{(12+2q)/(4+q)} B_*^{4/(4+q)}, \tag{3.45}$$

and

$$\tau_w = \frac{K_c^{4/(2+q)}}{K_q^{2/(2+q)}} \Omega_* \upsilon_{esc}^{-2/(2+q)} \dot{M}_w^{q/(2+q)} R_*^{2q/(2+q)} \Phi_{open}^{4/(2+q)}. \tag{3.46}$$

These equations are sucessors to equations (3.43), (3.44), since they drop the dependence of magnetic braking on the flow temperature. Thus, equations (3.45), and (3.46) should predict stellar torques for any given coronal temperature, but require the wind acceleration profile to be known. The values of fitting constants K_q, q, that determine the acceleration of the outflow, for the temperatures examined in this study, can be found in table 3.3 (see also section 3.8 for predictions on the values of these fitting constants over a continuous range of temperatures), and the values of K_c, K_l exist in subsections 3.5.1 and 3.5.3, respectively.

In order to give an example of how our formulation can be used, we apply it to the solar case. In general, the torque exerted on the Sun (or any star) is an integrated quantity, and its value depends on a sum over the local values of the angular momentum flux (see eqn 3.13). During the solar minimum the solar wind comprises two components, a fast and a slow wind (see also §3.1). Our wind models do not produce a bimodal outflow, and thus, we expect that our estimated solar torque should lie somewhere in-between the torques predicted by our fastest (i.e., with $c_s/\upsilon_{esc} = 0.4$) and one of our slower wind models (i.e., with $c_s/\upsilon_{esc} = 0.25$). To calculate the solar-wind torque, we will use the open-flux formula, given by equation (3.44), because the open magnetic flux is measured in the solar wind by in situ spacecraft. Furthermore, previous works (Réville et al. 2015a; Finley and Matt 2017) showed this formulation to be independent of the higher-order

field geometries studied there (i.e., quadrupolar and octupolar). Smith and Balogh (2003, 2008) show that the open flux at solar minimum is typically $\sim 7 \times 10^{22}$Mx. In addition, by using $\Omega_\odot = 2.87 \times 10^{-6}$rad s^{-1}, $\dot{M}_\odot = 2 \times 10^{-14} M_\odot$yr^{-1}, and the corresponding values of K_o, m_o for $c_s/v_{esc} = 0.25$ and 0.4, equation (3.44) yields an angular-momentum-loss rate of 0.9×10^{30} and 2.3×10^{30}erg, respectively. These values agree with the solar braking rate found by Pizzo et al. (1983), which is $2.5 - 3.8 \times 10^{30}$erg, and that found by Li (1999), which is 2.1×10^{30}erg.

Even though we have used a simplified wind modeling (i.e., polytropic), the proposed torque formalism should work for any cool star with a known wind acceleration, mass-loss rate, and magnetic properties. The physical mechanisms that expand flows from the hot coronae of cool stars are still unknown (e.g., Cranmer 2012; Cranmer et al. 2015), but it is certain from early studies (e.g., Holzer 1977) that the physics of coronal heating is more complex than simple thermal-pressure expansion. The most modern ideas include Alfvén-wave dissipation (e.g., Suzuki and Inutsuka 2005; Cranmer et al. 2007; Sokolov et al. 2013; van der Holst et al. 2014), which work as an energy source and drive magnetized outflows. However our full parameter space, with the range in flow temperatures that has been studied, should produce wind acceleration profiles within the range that exist in real stars.

Future work is needed to test the effects of more realistic wind physics (e.g., with variations in the polytropic index γ or improved coronal heating models), and extending the study into the fast-magnetic-rotator regime.

Chapter 4

Numerical and Thermodynamics Effects in Polytropic Winds and the Angular-Momentum Loss of Late-type Stars.

In this chapter we present two new parameter studies. The objective of this work is: 1) to investigate how the accuracy of the stellar-torque laws, derived in Chapter 3, can be affected by numerical-diffusion effects and 2) to generalize the torque prescriptions of Chapter 3, by considering a wider range of acceleration profiles due to variations in both the coronal temperature and polytropic index. In order to explore the first task, we employ a different and more accurate numerical scheme and reproduce the coronal-temperature parameter study presented in Chapter 3. For the second task, we use 5 new wind models, in which we vary both the flow temperature and polytropic index. The simulations shown here still employ axisymmteric, dipolar field geometries and slow rotators. Therefore, for each wind model, with a given value of c_s/v_{esc} and γ, we complete a parameter study in the surface magnetic field strength. In the following section (§4.1), the numerical setup used for this work is presented. In section 4.2, we briefly recall the input parameters for each simulation. In section 4.3, we focus on the reproduction study of the stellar coronal

temeprature. In section 4.4, we presenct the results of the parameter study that employs variations on both the coronal temperature and polytropic index. Finally, in section 4.5, the conclusions of this work are summarized.

4.1 Numerical Setup

This work employs again ideal MHD axisymmetric stellar-wind simulations, using the PLUTO code (Mignone et al. 2007). Our computational box is 2.5D (with two spatial coordinates and three vector components) and has spherical geometry. The set of the four ideal MHD conservations laws, presented in Chapter 3 (see equations (3.3) - (3.6)), is solved by PLUTO in order to obtain steady- or quasi-steady-state solutions.

The first task in this work is to understand how numerical effects (due to numerical diffusion) influence the global properties of our simulations (i.e. mass loss and angular momentum loss rates, the amount of open magnetic flux) and the accuracy of the derived torque laws, shown in Chapter 3. Therefore, all the simulations presented here are carried out with a less diffusive numerical scheme. All the primitive variables $(\rho, \boldsymbol{v}, p, \boldsymbol{B})$ are still spatially reconstructed with a second-order piecewise linear interpolation, but now the more compressive Van Leer flux limiter is used. In other words, the Van Leer limiter, compared to the minmod limiter used in chapter 3, produces a more accurate spatial reconstruction of the primitive variables. Furthermore, this numerical setup employs the approximate Riemann solver Roe (see e.g., Toro 2009), which provides better accuracy in the computation of the fluxes. The $\nabla \cdot \boldsymbol{B} = 0$ condition is controlled with the constrained transport (CT) method (Balsara and Spicer 1999), as previously. The "background field splitting" technique (Powell et al. 1999), which computes only the deviation from the initial magnetic field, is employed in the treatment of the magnetic field. Finally, the set of the four ideal MHD conservations laws are integrated in time with a second order Runge-Kutta scheme.

The computational grid is uniform along the $\widehat{\theta}$ direction, covering $\theta \in [0, \pi]$, with a total of 512 zones. A logaritmic grid is generated along the $\widehat{r}$ direction. The radial logarithmic grid preserves the cell aspect ratio at any distance from the origin. In order to obtain $\Delta r \simeq r\Delta\theta$, the resolution is increased along the r coordinate, covering $r \in [1, 50]R_*$,

with a total of 637 zones.

We adopt the initial conditions used in the parameter study of Chapter 3. The whole computational domain is inititialized with a dipolar magnetic field, analytically given by Equations (3.7) and (3.8), and a 1D, polytropic Parker's wind solution (for more details see section 3.3.1). The steady-state solutions do not depend on the initial state, but only on the inner boundary conditions. For all the variables (i.e., poloidal and toroidal magnetic field, toroidal velocity, thermal pressure, and mass density), except the poloidal velocity, we adopt the approach on the inner boundary conditions of the first study, described in detail in section 3.3.1. Now, instead of linearly extrapolating the computed value of v_p into the ghost zones, we impose the invariant α to be conserved across across the boundary (Zanni and Ferreira 2009). The invariant α is given as

$$\alpha = \frac{\rho \boldsymbol{v_p}}{\boldsymbol{B_p}}, \tag{4.1}$$

represents the mass flux per magnetic flux and is a constant of motion a along a field line for stationary, axisymmetric MHD solutions (e.g., Mestel 1968, 1999; Okamoto 1975; Heinemann and Olbert 1978; Lovelace et al. 1986; Keppens and Goedbloed 2000). This boundary is consistent with analytic theory of stationary, axisymmetric MHD flows and provides better stability in stellar-wind simulations, which allows us to employ a more accurate numerical scheme. Finally, we use an "outflow" type of boundary condition for the outer boundary of the r coordinate and an "axisymmetric" type of boundary condition for both boundary zones of the θ coordinate. The nature of these two types of boundary conditions was discussed in detail in section 3.3.1.

4.2 Input Parameters of the Simulations

For the studies presented in this chapter, we use the same input parameters for each simulation as previously, discussed in section 3.3.2. The dimensionless velocity of the adiabatic sound speed to the escape speed, c_s/v_{esc}, controls the thermodynamics of the flow. The dimensionless ratio of the Alfvén speed to the escape speed, v_A/v_{esc}, controls the strength of the magnetic field. Finally, the dimensionlesss ratio of the stellar equatorial rotation to

Case	c_s/v_{esc}	γ	v_A/v_{esc}	Υ	$< R_A > /R_*$	Υ_{open}	Φ_{open}/Φ_*	$\bar{V}_{R_A}/v_{esc}$
1	0.2219	1.05	0.0452	42	5.10	765	0.340	0.116
2	0.2219	1.05	0.105	231	7.37	2370	0.255	0.171
3	0.2219	1.05	0.301	2290	13.2	12000	0.182	0.262
4	0.2219	1.05	0.627	13800	21.0	38800	0.134	0.318
5	0.2219	1.05	0.953	38400	27.7	75700	0.112	0.342
6	0.25	1.05	0.21	33.7	4.36	943	0.421	0.196
7	0.25	1.05	0.301	70.3	5.13	1530	0.371	0.228
8	0.25	1.05	0.627	345	7.78	4840	0.298	0.306
9	0.25	1.05	0.953	950	10.0	9470	0.251	0.357
10	0.25	1.05	2.5	10200	18.8	43300	0.164	0.421
11	0.25	1.05	4.14	35000	26.5	96400	0.132	0.461
12	0.33	1.05	1.51	46.9	4.22	2450	0.575	0.529
13	0.33	1.05	2.5	163	5.83	5400	0.458	0.588
14	0.33	1.05	4.14	564	8.19	12000	0.368	0.639
15	0.33	1.05	11	6150	16.0	54500	0.237	0.727
16	0.33	1.05	17.5	18900	22.3	110000	0.191	0.750

Table 4.1: Simulation input parameters and resulting global wind properties. The second and third colum gives the values of input parameters c_s/v_{esc} and γ, respectively, which control the wind thermodynamics. The fourth column tabulates the input parameter v_A/v_{esc}, which controls the dipolar field strength, defined at the stellar equator. The fifth column presents the wind magnetization, Υ (see equation (4.3)). The sixth column provides the value of the effective Alfvén radius. Υ_{open} (see equation (4.2)) is given in the seventh column. The eighth column gives the fractional magnetic open flux and finally, the ninth column presents the average wind speed at the Alfvén surface (see equation (3.25)).

the break-up velocity controls the stellar spin rate, f. These dimensionless velocities are defined at the stellar surface, R_*. The magnetic field geometry is also a parameter in our studies, but in this work we focus only on dipolar fields. Therefore for the two parameter studies presented here, we only vary the dipolar field strength. Furthermore, we do not vary the stellar spin rate, which is kept fixed close to the solar value, $f = 0.00393$, and thus magnetocentrifugal acceleration is negligible in our simulations.

4.3 A Reproduction of the Parameter Study of the Coronal Temperature

4.3.1 Parameters of the Study

The first objective in this work is to examine how numerical diffusion affects the accuracy of our wind solutions, which can produce systematic errors in the derived magnetic braking laws. Therefore, we reproduce the parameter study on the stellar coronal temperature. The input parameter c_s/v_{esc} here varies between 0.2219 and 0.33, and the polytropic index, γ, is kept fixed at the value of 1.05. With the new numerical setup, we cannot simulate cases with $c_s/v_{esc} = 0.4$, because these solutions exhibit supersonic velocities very close to the stellar surface (see for example the velocity profiles of the 1D, hydrodynamic wind in figure 3.1). Wind solutions with such extreme acceleration profiles develop very steep gradients in the boundaries between the wind regions and the dead zones, and as a consequence the new numerical scheme cannot produce stable wind solutions. In order to simulate such cases with this numerical scheme a different approach to the boundary conditions and an increase in the grid resolution is required.However, in this work, we do not investigate this feature. Therefore, we cannot examine the accuracy of the fitting laws, given in chapter 3, for simulations with $c_s/v_{esc} = 0.4$. For this reproduction study we completed 16 numerical simulations and the parameters varied for each case are given in Table 4.1 (see second and fourth columns).

4.3.2 Results

4.3.2.1 Accuracy of the Numerical Solutions

Each simulation is stopped when it relaxes to a steady state. The correctness of each simulation is checked with the method introduced in Keppens and Goedbloed (2000). Analytic theory shows that for stationary, axisymmetric, ideal MHD flows, there are five scalar quantities (i.e., mass flux per magnetic flux, Bernoulli function, entropy, specific angular momentum flux, effective rotation rate of the field lines), which are conserved along a given field line (e.g., Mestel 1968, 1999; Okamoto 1975; Heinemann and Olbert 1978; Lovelace et al. 1986; Keppens and Goedbloed 2000). In order to examine the accuracy of each wind solution, we check whether these five invariants are conserved within some

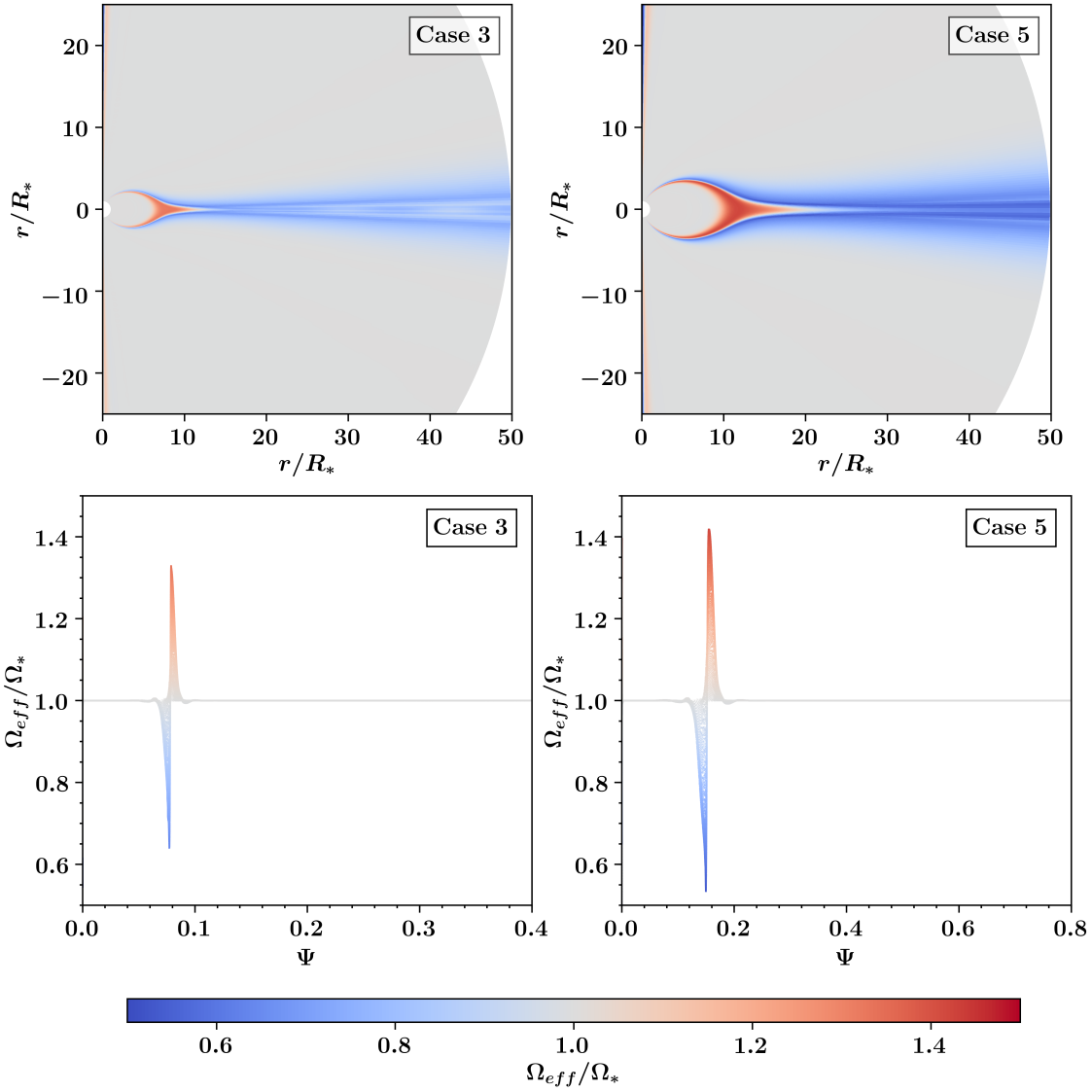

Figure 4.1: The same as figure 3.14. Case 3 has the same input parameters as the case 6 of figure 3.14 and case 5 has about the same wind magnetization as the case 9 of figure 3.14. For the two cases, shown in these plots, the wind region (with open field lines) has a value of Ψ that varies between 0 and 0.08 for case 3 (bottom-left panel), and between 0 and 0.16 for case 5 (bottom-right panel).

tolerance (see also §3.7).

In order to show the numerical accuracy of our wind simulations, we plot in figure 4.1 the normalized effective rotation rate of the field lines, Ω_{eff}/Ω_*, as a 2D colorscale plot (top panels) and as a function of Ψ, (bottom panels). Each value of the magnetic stream function, Ψ, represents a unique magnetic field line. As discussed in detail in section 3.7, any deviation from unity, in the plots of Ω_{eff}/Ω_*, occurs due to numerical errors. Two cases are presented in figure 4.1. Case 3 has the same input parameters as the case 6 in figure 3.14. Case 5 has a lower value of $\upsilon_A/\upsilon_{esc}$, but exhibits about the same wind magnetization when compared to case 6 of the study shown in chapter 3. Therefore both cases 3 and 5 are suitable for comparison with the cases shown in section 3.7, in order to examine whether this numerical scheme improves the numerical accuracy of our wind solutions. From figure 4.1, it is clear that this numerical setup still produces solutions, in which Ω_{eff}/Ω_* is not conserved along field lines adjacent to the dead zones. Both cases have midlatitude field lines, which either subrotate or overrotate by up to 40%. However, the simulations now exhibit sharper boundaries between the regions with wind and closed field lines, indicative of a reduction in the numerical errors in the outflow region. Furthermore, even solutions with high wind magnetization (and fairly extended dead zones), such as case 5, exhibit open field lines in which Ω_{eff}/Ω_* is well conserved (at least within 2%). Overall, we verified that in each of our simulations, presented in this chapter, all the invariants (not shown) exhibit a better conservation along the field lines. Clearly, this setup improves the numerical accuracy of the wind solutions and therefore is more suitable for stellar-wind studies.

The global outflow rates (i.e., mass and angular momentum loss rates) and the amount of the unsigned open magnetic flux are computed using the equations (3.12), (3.13), and (3.16), respectively. To further verify the improved accuracy of our setup, in Figure 4.2, we show the wind mass-loss rate as a function of the radial distance (i.e., cyan line in Figure 4.2) of case 3, given in Table 4.1. The black dotted line in the figure represents the median value of $\dot{M}_w$ above $10R_*$. As mentioned above, case 6 of Table 3.2 has the same input parameters as case 3 shown in this chapter. For comparison, we include in the plot the behavior of $\dot{M}_w(r)$ of this case (i.e., red line in Figure 4.2) and the

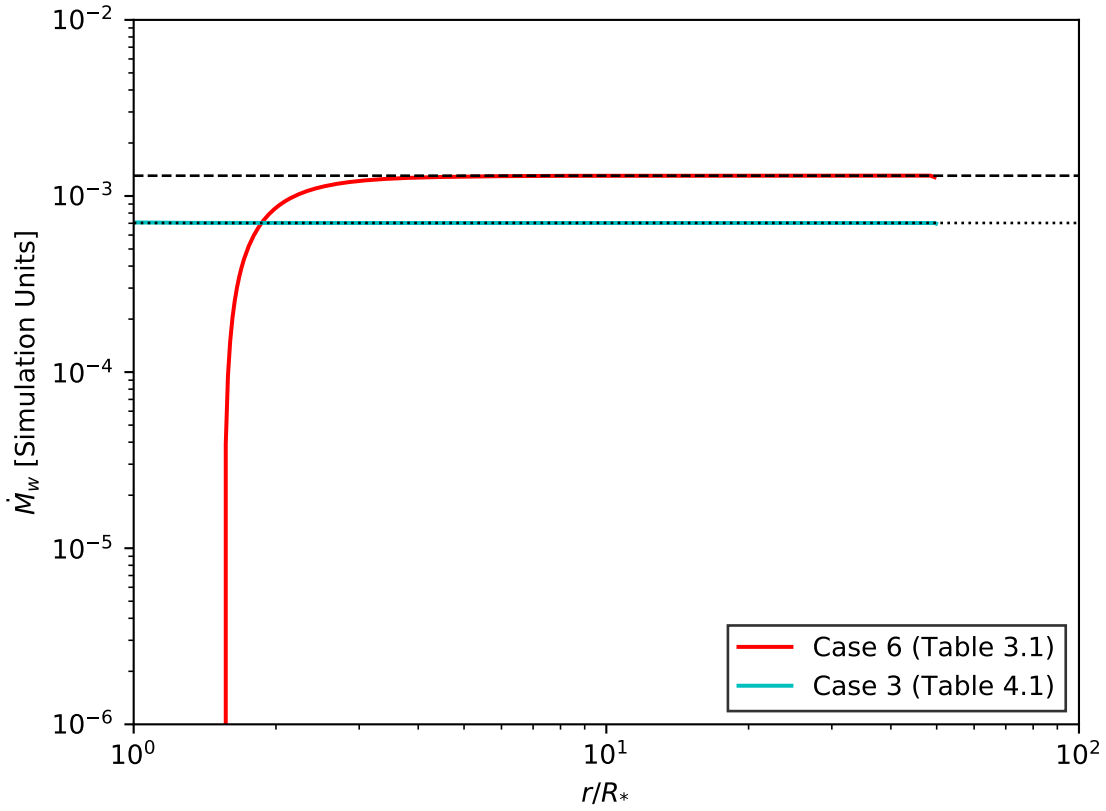

Figure 4.2: $\dot{M}_w$ as a function of the radial distance, r. The cyan line corresponds to case 3, given in Table 4.1. The red line shows the global mass-loss rate of case 6 of chapter 3 (see Table 3.2). The black dotted and dashed lines show the median values (above $10R_*$) of $\dot{M}_w$ of these 2 cases, respectively. Case 6 shows non conservation of $\dot{M}_w$ at the first few stellar radii due to numerical diffusion. The new numerical setup improves the accuracy of our simulations and therefore, case 3 exhibits perfect conservation of $\dot{M}_w$ at all r.

black dashed line in the figure shows the median value of $\dot{M}_w$. From the plot, it is clear that the new setup produces more accurate wind solutions since the wind mass-loss rate is perfectly conserved at all radii (i.e., case 3). In contrast, case 6 exhibits non conservation of mass at the first few stellar radii. Therefore, the method for computing the global outflow rates, introduced in chapter 3, should be used when numerical diffusion affects the global properties of the wind solutions. Furthermore, while the simulations share the same input parameters, they have different mass-loss rates (by $\sim 50\%$). This is also an effect due to numerical diffusion. Our scaling laws are independent of the exact value of $\dot{M}_w$ (i.e., the wind mass-loss rate is treated as a free parameter in our studies), but as we will show in the next sections a less accurate setup affects the wind velocity/acceleration profile and the amount of the magnetic open flux produced in each simulation. These two features affect the value of $< R_A > /R_*$ and this leads to less accurate torque presciptions.

c_s/v_{esc}	γ	K_s	m_s	K_o	m_o	K_q	q	C_o	p_o
0.2219	1.05	1.95 ± 0.08	0.249 ± 0.005	0.43 ± 0.04	0.368 ± 0.009	0.045 ± 0.009	0.64 ± 0.08	1.61 ± 0.03	0.162 ± 0.003
0.25	1.05	1.71 ± 0.03	0.260 ± 0.003	0.29 ± 0.02	0.391 ± 0.008	0.11 ± 0.02	0.46 ± 0.06	1.30 ± 0.04	0.167 ± 0.004
0.33	1.05	1.43 ± 0.03	0.278 ± 0.003	0.136 ± 0.007	0.438 ± 0.005	0.40 ± 0.02	0.21 ± 0.02	0.858 ± 0.006	0.183 ± 0.0009

Table 4.2: Fitting constants of the parameter study. The third and fourth colum gives the fitting constants of the fitting law (3.15). The fifth and sixth column presents the fitting constants of equation (3.18). The seventh and eighth colum provides the fitting constants of the velocity law (3.28). The ninth and tenth column gives the values of the fitting constants of equation (4.4).

4.3.2.2 The Dependence of the Alfvén Radius on Υ_{open}

In this section, we present the dependence of the effective Alfvén radius, $< R_A > /R_*$, on the parameter Υ_{open}, which is defined as

$$\Upsilon_{open} \equiv \frac{\Phi_{open}^2}{R_*^2 \dot{M}_w \upsilon_{esc}}. \tag{4.2}$$

All the values of the parameter Υ_{open} and fractional open flux, Φ_{open}/Φ_*, of this reproduction study, are given in the seventh and eighth column of Table 4.1, respectively. For each simulation, the torque-averaged Alfvén radius, $< R_A > /R_*$, is computed using equation (3.2) and is given in the sixth column of Table 4.1. In figure 4.3, we plot the effective Alfvén radius, $< R_A > /R_*$, versus the parameter Υ_{open}. The data are fitted using the function (3.18) and the fitting constants K_o, m_o are listed in Table 4.2. For comparison, we include in the plot the data and fits of the parameter study presented in Chapter 3. In figure 4.3, three power laws are shown, one for each value of c_s/υ_{esc} (or flow acceleration profile). Now, these power laws appear to be steeper when compared to the scaling laws of $< R_A > /R_*$ versus Υ_{open} presented in the previous chapter. This feature can be understood as an effect due to the different and more accurate numerical scheme used in this study.

In section 3.5.2, we demonstrated that the simple power laws of $< R_A > /R_*$ with Υ_{open} (or parameter Υ), for a given value of c_s/υ_{esc}, can be explained, because the wind's average speed at the Alfvén radius, $\bar{\mathrm{V}}_{R_A}$, scales as a power law with $< R_A > /R_*$ (see equation (3.28)). For each wind solution, $\bar{\mathrm{V}}_{R_A}$ is computed using equation (3.25) and is tabulated in the ninth column of Table 4.1. We find that the data (i.e., $\bar{\mathrm{V}}_{R_A}$ versus $< R_A > /R_*$) exhibit a similar behavior as previously (shown in §4.4.2). The data are fitted using equation (3.28) and the dimensionles fitting constants K_q and q are given in Table 4.1. These two fitting constants are directly related with the flow acceleration profile and therefore critically depend on the correctness (or accuracy) of each numerical simulation. Furthermore, K_q and q are included in the theoretical expressions of K_o and m_o (see equation 3.31). It is clear that the new values of K_q and q systematically differ from their counterparts, given in Table 3.3. We find that for each coronal temperature studied here, K_q has always a higher value (by at least 20%) and q is always smaller (by

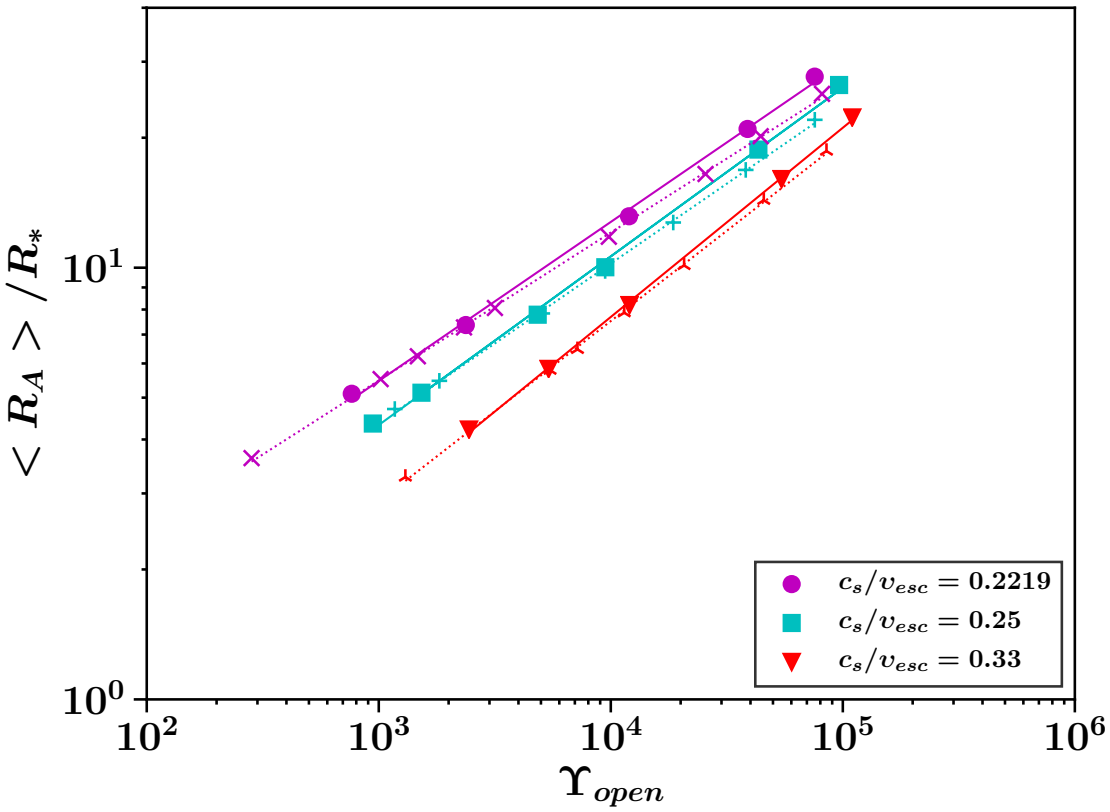

Figure 4.3: The dependence of $< R_A > /R_*$ on the parameter Υ_{open}. Circles (magenta), diamonds (cyan), and pointing-down triangles (red) represent simulations with $c_s/v_{esc} = 0.2219$, 0.25, and 0.33, respectively. Three different power laws (solid lines) are shown, one for each grid of simulation with a given value of c_s/v_{esc}. For comparison the data points (crosses of the same color) and fits (dotted lines of the same color) of the parameter study, presented in Chapter 3, are shown. The new power laws are steeper, but they exhibit about the same range in $< R_A > /R_*$, for a given value of Υ_{open}, when compared to their counterparts of the previous study.

at least 30%) compared to the values of K_q and q given in Table 3.3. As a consequence each simple power law, in figure 4.3, show a steeper dependence of the effective Alfvén radius on parameter Υ_{open}. Since this stellar-wind setup produces more physically correct solutions the new values of K_o, m_o are more appropriate for stellar-torque predictions, using equation (3.44).

In this study, most of the simulations have the same input parameters as the cases of the previous study, and therefore, any difference in the value of Υ_{open}, of each new simulation, indicates differences in the obtained values of Φ_{open} and $\dot{M}_w$, which can also be understood as a result due to the different numerical setup. However, from figure 4.3, it is clear that this reproduction study predicts about the same range in $< R_A > /R_*$ for a given value of Υ_{open}. The fact that the fitting constants K_o and m_o did not significantly change due to the improved accuracy of our wind solutions, indicates that Υ_{open} should be the controlling parameter, in order predict the effective Alfvén radius and the resulting stellar torque. This approach significantly mitigates numerical-diffusion effects that produce systematic errors in torque laws derived from numerical simulations. In other words, the torque laws, which depend on the parameter Υ_{open} (see equations (3.44) and (3.46)) are less sensitive to the accuracy of the simulations.

Using equation (3.34), we verified that all the simulation data collapse into a unique power law, independent of the stellar coronal (or outflow) temperature. At this point, we choose to not show this figure, in order to include the new data points from the parameter study in both the coronal temperature and the flow polytropic index that will be presented in the following sections.

4.3.2.3 The Dependence of the Alfvén Radius on Υ

The wind magnetization, Υ, is defined as

$$\Upsilon \equiv \frac{B_*^2 R_*^2}{\dot{M}_w v_{esc}}, \tag{4.3}$$

and the values of Υ of this study are given in fifth column of Table 4.1. The dependence of $< R_A > /R_*$ on Υ is illustrated in figure 4.4. The function (3.15) is used in order

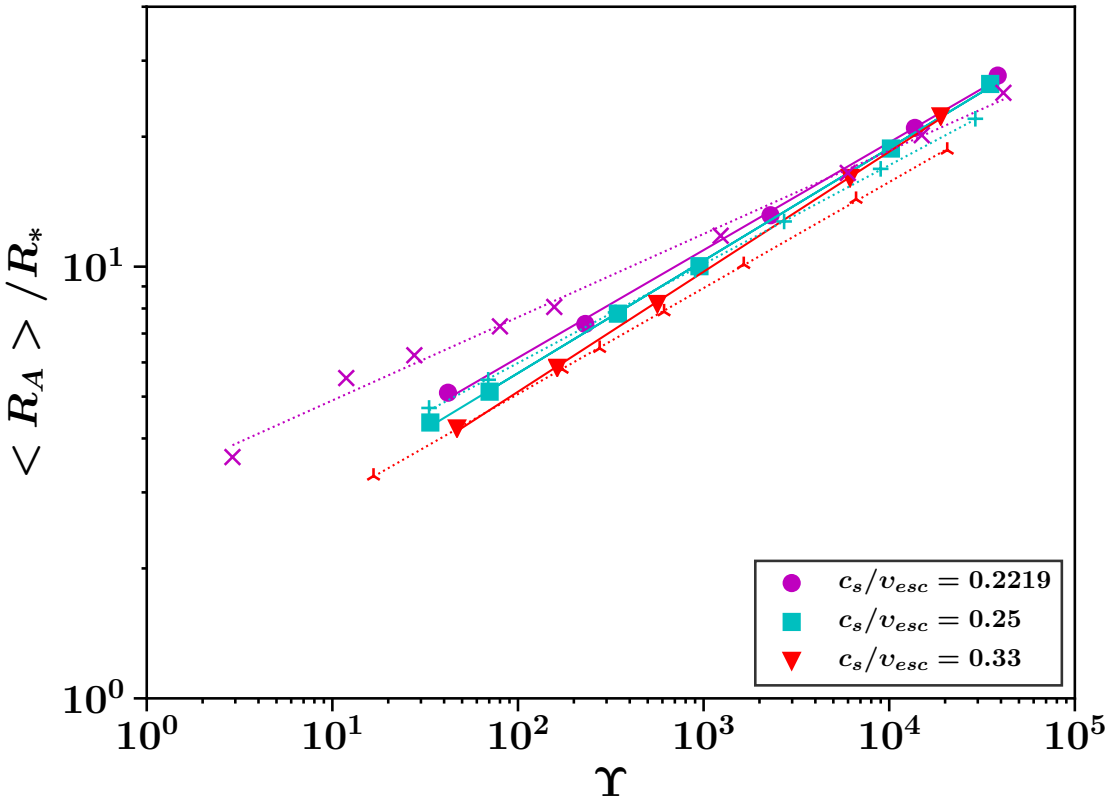

Figure 4.4: The effective Alfvén radius, $< R_A > /R_*$, versus parameter Υ. Colors, symbols, and line styles have the same meaning as in figure 4.3. The three new fitting laws, one for each value of c_s/v_{esc}, show a steeper dependence of $< R_A > /R_*$ on Υ. For a given value of Υ, the power laws produce a smaller range in $< R_A > /R_*$. Due to the behavior of data points in figure 4.3, this feature indicates, for a given Υ that new simulations produce a wider range in the fractional open flux.

to fit the simulation data. The values of the dimensionless fitting constants K_s, m_s are given in Table 4.2. As expected, each value of c_s/v_{esc} gives a simple power law of the effective Alfvén radius on the wind magnetization. For comparison, we show in the figure the data and fits of the study presented in Chapter 3. Every new power law appears to be significantly steeper compared to its previous counterpart of the same value of c_s/v_{esc}. The values of the fitting constant m_s, for the three scaling laws shown in figure 4.4 now vary between 0.249 and 0.278. In section 3.5.3 (see equation (3.37)), it was identified that m_s can be expressed with the form, $m_s = 1/(2l + 2 + q) = 1/(4 + q)$, for a dipolar field geometry (i.e., $l = 1$). In section 3.5.2, it was demonstrated that the fitting constant q is always positive and approaches zero for hotter outflows with faster acceleration profiles. Therefore, it was concluded that m_s cannot exceed the value of 0.25. From the fitting laws, shown in figure 4.4, it is clear that this analysis cannot predict the obtained values of the fitting constant m_s. From equation (3.32), the slopes of the new power laws can be described by an additional scaling of the dimensionless ratio $< R_o > / < R_A >$ with parameter Υ. We investigate this feature in the following section. Lastly, in figure 4.4, the new data points, show a smaller range in the effective Alfvén radius, $< R_A > /R_*$, for a given value of Υ. However, this feature cannot be interpreted as a smaller influence of the wind acceleration (or coronal temperature) on the stellar torque. This behavior of the simulation data indicates that this new numerical setup produces a broader range in the fractional open magnetic flux for a given value of Υ. The main conclusion here is that the torque laws, which depend on the wind magnetization, Υ, are more sensitive to effects due to numerical diffusion. Furthermore, the new values of the fitting constants K_s and m_s are more suitable for predicting stellar torques using equation (3.43).

In figure 4.5, we present the effective Alfvén radius versus the quantity $\Upsilon v_{esc} \bar{V}_{R_A}^{-1}$. The data points are fitted with the function (3.34). From the plot, it is clear that the data do not collapse into a single power, independent of the flow acceleration profile. The spread of the data points is now broader and more systematic, compared to the spread of the data shown in figure 3.11, and indicates systematic variations of $< R_o > / < R_A >$ with the flow temperature (see also equation (3.32)). Futhermore, the points exhibit a slope, which cannot be represented by a fitting law with a fixed power-law index at the value of 1/4.

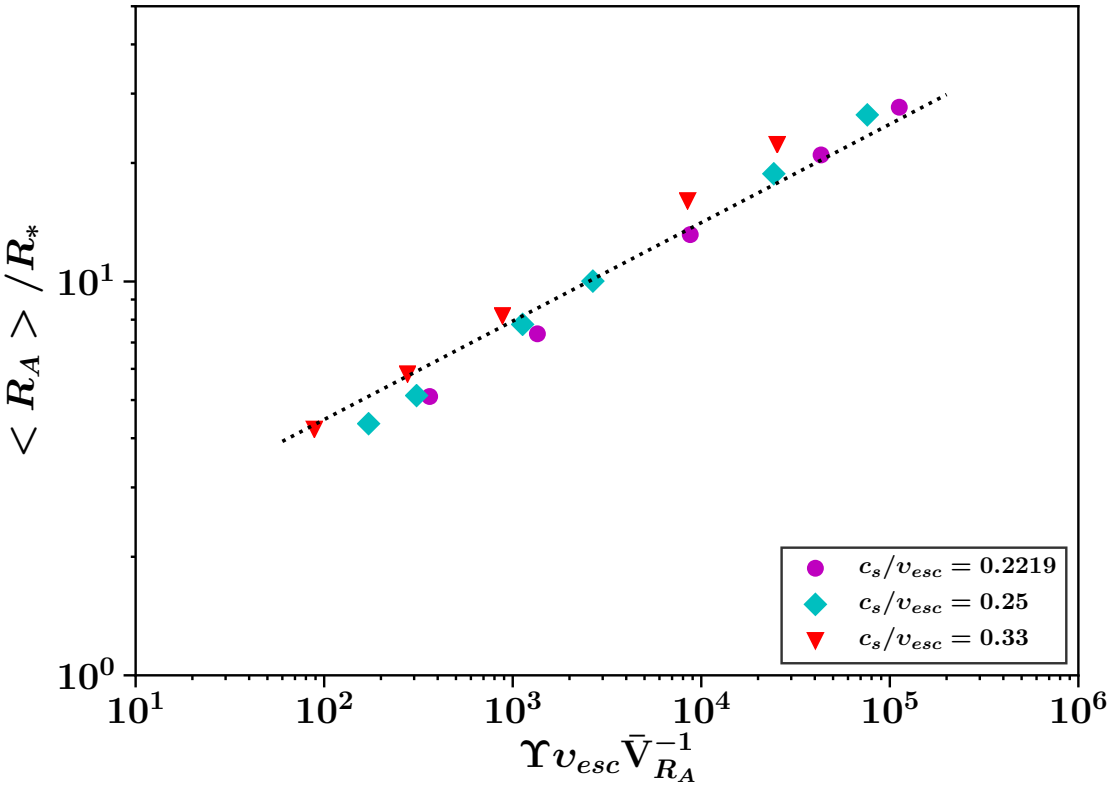

Figure 4.5: $< R_A > /R_*$ versus the quantity $\Upsilon v_{esc} \bar{V}_{R_A}^{-1}$. Color/symbols are the same as in figure 4.3. The dotted line represents the fitting function (3.34). The data points do not collapse into a single power law and follow a line of a different slope. The more systematic and wider spread of the data, compared to the behavior of the points in figure 3.11, implies a stronger dependence of the value of $< R_o > / < R_A >$ on the flow temperature.

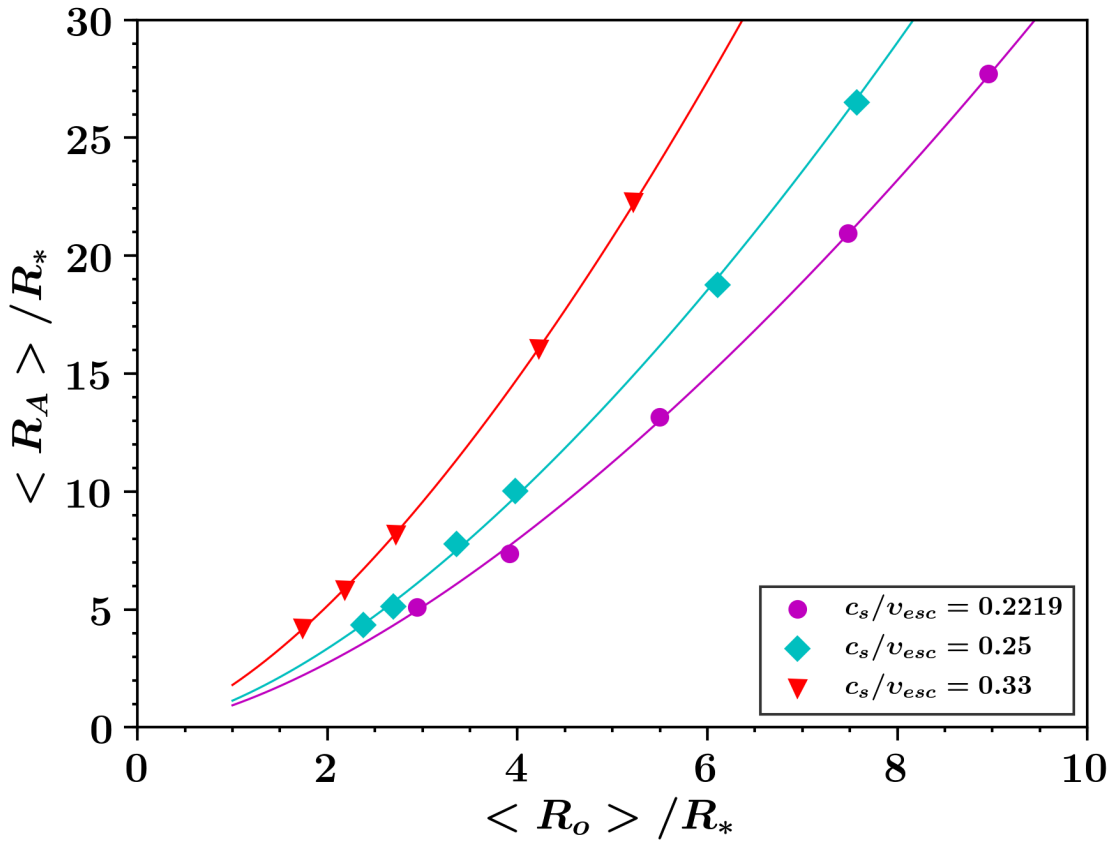

Figure 4.6: The dependence of $< R_A > / < R_* >$ on the effective open-field radius, $< R_o > / < R_* >$. Color/symbols are the same as in figure 4.3. Three power laws are shown, one for each value of c_s/υ_{esc}. The precise trends between $< R_A > / < R_* >$ and $< R_o > / < R_* >$, shown in the plot, can now explain the scatter of the data in figure 4.5.

4.3.2.4 The Dependendence of the Open-Field Radius on Υ

For our simulations, $< R_o > /R_*$ is computed using equation (3.36) and for the rest of this work, $< R_o > /R_*$ will be referred as the "effective open-field radius" or "flux-averaged open-field radius". In figure 4.6, the dependence of the effective Alfvén radius, $< R_A > /R_*$ on the flux-averaged open-field radius, $< R_o > /R_*$, is illustrated. From the plot, it is clear that the new simulation data cannot be represented by a single linear function as previously (see figure 3.12). Now, each set of simulations with a given value of c_s/υ_{esc} gives a unique scaling between $< R_A > /R_*$ and $< R_o > /R_*$. In order to fit the data, we use a power-law function in the form of, $< R_A > /R_* = C(< R_o > /R_*)^p$, where C and p are dimensionless fitting constants. As shown in the figure, this functional form provides an excellent fit to the data. The fittng constants of the power laws of figure 4.6 are not listed in a table, because we choose to tabulate the fitting constants of the scalings

between $< R_o > /R_*$ and Υ, which will be shown in the next figure. The precise scalings shown in figure 4.6 can now explain the scatter of the data observed in figure 4.5 (see also discussion in §3.5.3).

The dependence of $< R_o > /R_*$ on the wind magnetization, Υ, for this reproduction study is presented in figure 4.7. The data are fitted with a function in the form of

$$< R_o > /R_* = C_o \Upsilon^{p_o}, \tag{4.4}$$

where again C_o and p_o represent dimensionless fitting constants. Three simple power laws are shown in figure 4.7, and the fitting constants for each scaling law are given in Table 4.2. The plot demonstrates that differences in the wind themodynamics, the coronal temperature here, have a singnificant influence on the radius, at which the magnetic field opens and decreases as a monopole (i.e., open-field radius). For the flow acceleration profiles studied here, the range in $< R_o > /R_*$ for a given value of the Υ is about 2.

Equation (3.32) can also be written in an explicit form for R_A/R_* as

$$\left(\frac{R_A}{R_*}\right)^2 = \left(\frac{R_*}{R_o}\right)^{2l} \Upsilon \frac{\upsilon_{esc}}{\upsilon(R_A)}. \tag{4.5}$$

Following equation (4.5), in figure 4.8, we plot the effective Alfvén radius, $< R_A > /R_*$, versus the quantity $(R_*/ < R_o >)^{-2} \Upsilon \upsilon_{esc} \bar{\mathrm{V}}_{R_A}$. To fit the data we use the function

$$\frac{< R_A >}{R_*} = K_l \left[\left(\frac{R_*}{< R_o >} \right)^2 \Upsilon \frac{\upsilon_{esc}}{\bar{\mathrm{V}}_{R_A}} \right]^{1/2}, \tag{4.6}$$

where K_l is the only fitting constant, and its best-fit value is

$$K_l = 0.762 \pm 0.006. \tag{4.7}$$

The value of K_l deviates from unity due to 2D effects, neglected in equation (4.5) and moreover, agrees very well with the value of the fitting constant K_c, given by equation (3.27). From figure 4.7 it is clear that, by including in the torque formalism, which depends on Υ, both the dimensionless terms $< R_o > / < R_* >$ and $\bar{\mathrm{V}}_{R_A}/\upsilon_{esc}$, the data collapse

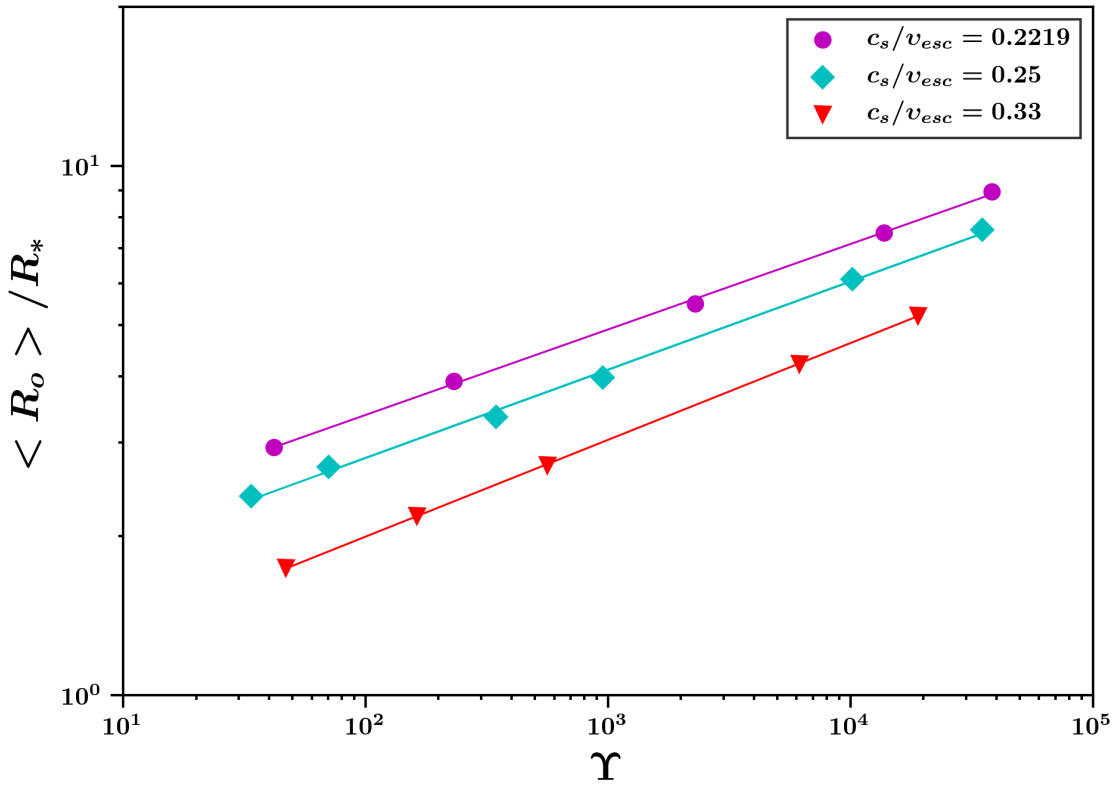

Figure 4.7: Dependence of the effective open-field radius, $< R_o > / < R_* >$ on Υ. Color/symbols are the same as in figure 4.3. Each power law corresponds to a specific value of c_s/v_{esc}. For a given Υ, a faster wind, due to a higher coronal temperature, stretches the magnetic field to a radial configuration closer to the star.

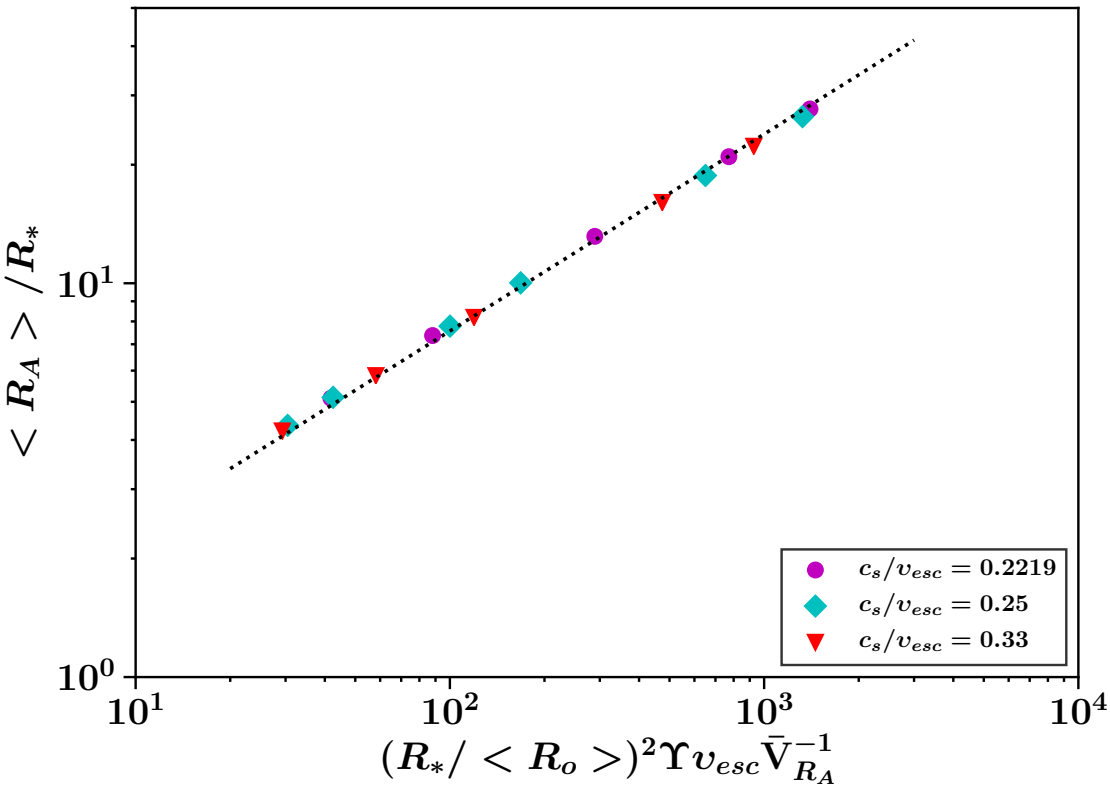

Figure 4.8: $< R_A > /R_*$ versus the quantity $(R_*/ < R_o >)^2 \Upsilon v_{esc} \bar{V}_{R_A}$. Color/symbols are the same as in figure 4.3. All the simulation data can now be represented by a single and precise power law, independent of the flow acceleration. The fitting line (dotted line) has a fixed power-law index to 1/2, according to function (4.6).

in a single and precise power law. In other words, equation (4.6) can predict the effective Alfvén radius, but now requires the knowledge of Υ, $\bar{\mathrm{V}}_{R_A}$, and $< R_o >$.

By substituting the expression for $< R_o > /R_*$ and $\bar{\mathrm{V}}_{R_A}/\upsilon_{esc}$ given by equations (3.28) and (4.4), respectively, equation (4.6) becomes

$$\frac{< R_A >}{R_*} = \left(\frac{K_l^2}{C_o^2 K_q}\right)^{\frac{1}{2+q}} \Upsilon^{\frac{1-2p_o}{2+q}}. \tag{4.8}$$

Comparing equations (3.15) and (4.8), we identify that $K_s \sim [K_l^2/(C_o^2 K_q)]^{\frac{1}{2+q}}$ and $m_s \sim (1-2p_o)/(2+q)$. The new dependence of the fitting constant m_s on both p_o and q can now describe the values of the power-law indices extracted from the scalings between $< R_A > / < R_* >$ and Υ in figure 4.4. Furthermore, this latter analysis explains why the fitting constants K_s, m_s (and the torque fomulae that predict stellar torques based on the wind magnetization) are very sensitive to the numerical accuracy of the simulations. The exact scalings of $\bar{\mathrm{V}}_{R_A}$ versus $< R_A > / < R_* >$ and $< R_o > / < R_* >$ versus Υ, which determine the values of K_s and m_s, strongly depend on the ability of the numerical scheme to produce physically correct (or numerically accurate) wind solutions.

4.4 A Parameter Study on both the Flow Temperature and Polytropic Index

In this section, we present the results of a second parameter study, in which we consider wind models with a wider range of wind acceleration profiles by including variations in both the coronal temperature and polytropic index.

4.4.1 Parameters of the Study

This parameter study includes 24 new simulations. As previously, for each wind model with a given value of c_s/υ_{esc} and γ, we vary the surface magnetic field strength, parametrized by the dimsensionless velocity $\upsilon_A/\upsilon_{esc}$. The stellar spin rate is still taken to be close to the solar one (see also section 4.2). Five new flow acceleration profiles are considered here. Two wind models have a value of $c_s/\upsilon_{esc} = 0.25$ and values of $\gamma = 1.08$ and $\gamma = 1.01$, respectively. Three wind models have a value of $c_s/\upsilon_{esc} = 0.33$ and values of $\gamma = 1.15$,

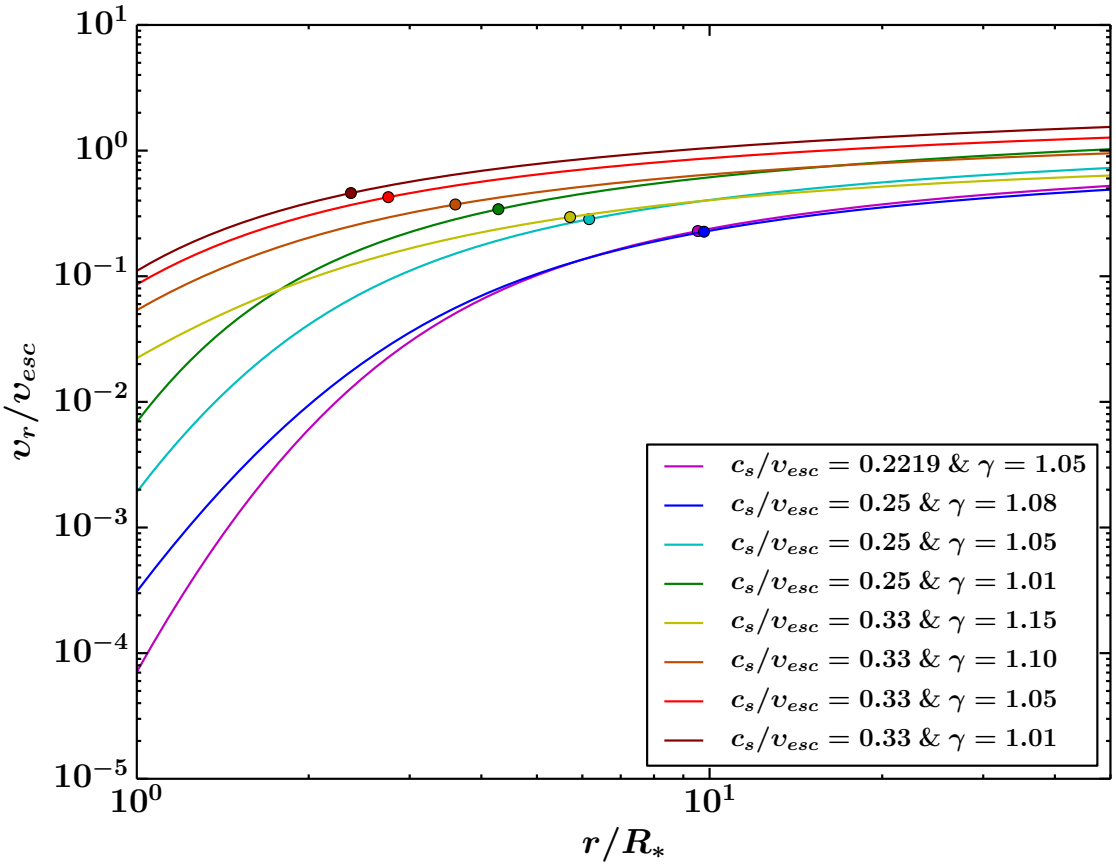

Figure 4.9: Normalized wind velocity versus r/R_* for eight different polytropic wind models (i.e., Parker's winds) with different values in the coronal temperature and polytropic index. The above profiles are also used as the initial velocity wind profile in our simulations. Each wind model, with a given combination of c_s/v_{esc} and γ exhibits a distinct acceleration profile. The circles on each velocity profile represent the sonic point.

$\gamma = 1.10$, and $\gamma = 1.01$, respectively. Figure 4.9 depicts the analytic velocity laws, as a function of radial distance, of one-dimensional, hydrodynamic, and polytropic winds (i.e., Parker's winds). Each curve, shown by a different color, corresponds to a flow with a given coronal temperature (parametrized by c_s/v_{esc}) and a given value of the polytropic index. Furthermore, these profiles are used as an initial condition for each set of simulations having a specific combination of c_s/v_{esc} and γ (see sections 3.3.1 and 4.1). In all the figures that will be shown below, we will include the data and fits found in section 4.3.2. Therefore, in figure 4.9, we also include the velocity profiles considered in the previous study of this chapter. From the plot, it is clear that each wind with a different value of c_s/v_{esc} and γ exhibits a unique velocity and acceleration profile. The trend in figure 4.9 is the following. For a fixed value of γ, a wind model with a higher value of c_s/v_{esc} is faster everywhere compared to a flow with a lower value. In contrast, for a fixed value of c_s/v_{esc}, a flow with a lower value of γ is faster at every radius compared to wind with a higher value. The winds shown in the plot exhibit a range in velocities at R_* of about three orders of magnitude and of more than a factor of 2 at $50R_*$. However, it is clear from figure 4.9 that this study, compared to the previous one, considers a more extensive range of wind acceleration profiles. The parameters varied for each of the 24 simulations, presented here, are given in second, third, and fourth column of Table 4.3.

4.4.2 Results

The main conclusion, from the study presented in Chapter 3, was that a faster wind (due to a higher coronal temperature), for a given Υ or Υ_{open}, reaches the Alfvén speed at a radial distance closer to the star and therefore the size of the magnetic lever-arm is reduced. Thus, the magnetic torque on the stellar surface becomes weaker. Here, we find that for a fixed value of c_s/v_{esc}, a decrease in the flow polytropic index γ, which also results in a faster wind, has the same effect on the stellar torque. Figure 4.10 shows the colorscale plots of the normalized poloidal velocity, v_{pol}/v_{esc}, with magnetic field lines (white lines) for three steady-state wind solutions of this parameter study. Each simulation illustrated in the plot has the same order of magnitude (and about the same value) in Υ, a value of c_s/v_{esc} equal to 0.25, but a different polytropic index. The figure clearly demonstrates that a lower value of γ leads to a wind that is faster everywhere. As a consequence the

Case	c_s/v_{esc}	γ	T_* (MK)	v_A/v_{esc}	Υ	$< R_A > /R_*$	Υ_{open}	Φ_{open}/Φ_*	$\bar{V}_{R_A}/v_{esc}$
1	0.25	1.08	1.61	0.105	51.6	5.43	914	0.335	0.121
2	0.25	1.08	1.61	0.301	438	8.73	3700	0.231	0.188
3	0.25	1.08	1.61	0.953	6260	17.3	23200	0.153	0.284
4	0.25	1.08	1.61	2.5	66600	32.9	107000	0.101	0.331
5	0.25	1.01	1.72	0.627	94.1	5.27	2680	0.425	0.376
6	0.25	1.01	1.72	0.953	255	6.79	5290	0.362	0.441
7	0.25	1.01	1.72	2.5	2730	12.6	24100	0.236	0.536
8	0.25	1.01	1.72	6.2	25000	23.3	98900	0.158	0.601
9	0.33	1.15	2.63	0.627	24.5	4.08	889	0.479	0.205
10	0.33	1.15	2.63	0.953	56.9	4.99	1540	0.414	0.236
11	0.33	1.15	2.63	2.5	541	9.00	7280	0.292	0.334
12	0.33	1.15	2.63	4.14	1900	12.6	15900	0.231	0.358
13	0.33	1.15	2.63	8.6	11600	20.8	50100	0.165	0.392
14	0.33	1.15	2.63	11	21200	24.7	73900	0.148	0.395
15	0.33	1.10	2.75	0.953	24.1	3.76	1280	0.580	0.350
16	0.33	1.10	2.75	2.5	247	6.84	5920	0.389	0.468
17	0.33	1.10	2.75	4.14	862	9.61	13100	0.310	0.509
18	0.33	1.10	2.75	6.2	2340	12.7	24600	0.258	0.528
19	0.33	1.10	2.75	11	9560	18.9	60200	0.200	0.565
20	0.33	1.10	2.75	17.5	29600	26.2	123000	0.162	0.577
21	0.33	1.01	2.99	2.5	130	5.31	5190	0.503	0.681
22	0.33	1.01	2.99	6.2	1200	9.79	21700	0.338	0.766
23	0.33	1.01	2.99	11	4830	14.6	51900	0.261	0.855
24	0.33	1.01	2.99	17.5	14800	20.0	99700	0.206	0.881

Table 4.3: Simulation input parameters and resulting global wind properties. The stellar coronal temperatures, presented in the fourth column of this table, were computed from equation (3.10) using $M_* = 1M_\odot$ and $R_* = 1R_\odot$. Using the method introduced in section 3.3.2, B_* can be evaluated from the values of Υ, for given stellar parameters and $\dot{M}_w$.

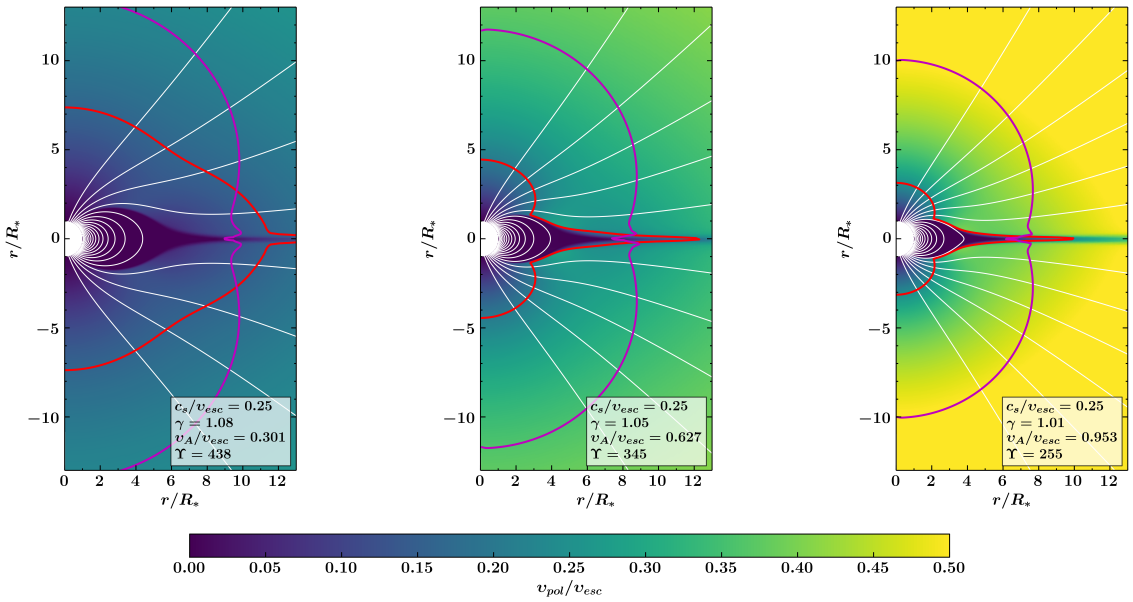

Figure 4.10: Normalized poloidal velocity (colorscale) with magnetic field lines in the inner region of three steady-state wind solution with similar magnetization, same coronal temperature, but different polytropic index γ. The red and magnenta lines represent the sonic and Alfvénic surfaces, respectively. A decrease in γ, for about the same value of Υ, produces a faster wind solution, and thus both these two critical surfaces move closer to the star.

location of the sonic (red line) and Alfvénic (magenta line) surface is closer to the stellar surface.

We found that the analysis and conclusions regarding the influence of the flow thermodynamics on the stellar magnetic torque, presented in the previous sections of this chapter and chapter 3, can be generalized for any axisymmetric polytropic flow with a given coronal temperature and a polytropic index, for dipolar fields and slow rotators. Therefore in this section we mainly present the scaling laws found from this study.

c_s/v_{esc}	γ	K_s	m_s	K_o	m_o	K_q	q	C_o	p_o
0.25	1.08	1.9 ± 0.1	0.252 ± 0.007	0.40 ± 0.04	0.38 ± 0.01	0.05 ± 0.01	0.6 ± 0.1	1.60 ± 0.04	0.166 ± 0.003
0.25	1.01	1.56 ± 0.04	0.266 ± 0.004	0.20 ± 0.01	0.412 ± 0.008	0.24 ± 0.03	0.30 ± 0.05	1.04 ± 0.02	0.178 ± 0.002
0.33	1.15	1.71 ± 0.03	0.267 ± 0.003	0.25 ± 0.02	0.407 ± 0.007	0.13 ± 0.02	0.36 ± 0.06	1.19 ± 0.03	0.173 ± 0.003
0.33	1.10	1.54 ± 0.04	0.273 ± 0.004	0.17 ± 0.01	0.427 ± 0.007	0.27 ± 0.03	0.25 ± 0.04	0.96 ± 0.01	0.180 ± 0.002
0.33	1.01	1.35 ± 0.02	0.281 ± 0.002	0.11 ± 0.01	0.448 ± 0.008	0.49 ± 0.02	0.2 ± 0.02	0.79 ± 0.03	0.187 ± 0.004

Table 4.4: Fitting constants of the parameter study.

The values of Υ, $< R_A > /R_*$, Υ_{open}, Φ_{open}/Φ_*, and $\bar{\mathrm{V}}_{R_A}/\upsilon_{esc}$, for each simulation of this second study, are listed in Table 4.3. The dependence of $< R_A > /R_*$ on parameter Υ_{open} is shown in figure 4.11. The data are fitted with equation (3.18) and the values of the fitting constants K_o, m_o, for each power law shown in the plot, are given in Tables 4.2 and 4.4. In figure 4.12, we plot $\bar{\mathrm{V}}_{R_A}/\upsilon_{esc}$ versus $< R_A > /R_*$, Υ_{open}. The data are fitted with equation (3.28) and the fitting constans K_q and q, for each scaling law shown, are listed in Tables 4.2 and 4.4. In figure 4.13, the effective Alfvén radius is plotted versus the quantity $\Upsilon_{open}\upsilon_{esc}\bar{\mathrm{V}}_{R_A}^{-1}$. As expected, the data collapse in single power law, indepent of the flow thermodynamics and field geometry. The function (3.26), provides an excellent fit and for the fitting constant K_c, we obtain

$$K_c = 0.754\left(\frac{1}{4\pi}\right) \pm 0.002. \tag{4.9}$$

Based on the analysis presented in the previous sections the outcome of figures 4.11, 4.13, and 4.13 is the following. For winds with different acceleration profiles, the quantity $\bar{\mathrm{V}}_{R_A}$ is the key term that needs to be included in torque prescriptions that are based on Υ_{open}. Furthermore, for a given value of Υ_{open}, the wind that exhibits the highest average speed at the Alfvén surface, regardless of how the plasma accelerates out to this critical surface, has the smaller effective lever-arm, which results in a less efficient magnetic braking.

The effective Alfvén radius, $< R_A > /R_*$, is plotted versus the wind magnetization Υ in figure 4.14. The function (3.15) is used to fit the data and the values of the fitting constants K_s, m_s, for each scaling law shown in the plot, are given in Tables 4.2 and 4.4. In figure 4.15, the dependence of the effective open-field radius, $< R_o > /R_*$, on Υ is presented. The function (4.4) fits the data and the values of C_o and p_o, for each power law, are listed in Tables 4.2 and 4.4. Finally, in figure 4.16, we plot $< R_A > /R_*$ versus the quantity $(R_*/ < R_o >)^{-2}\Upsilon\upsilon_{esc}\bar{\mathrm{V}}_{R_A}$. Again, the data collapse is a single braking law, which is represented by equation (4.6). We find that the best-fit value of K_l is

$$K_l = 0.756 \pm 0.004. \tag{4.10}$$

From figures 4.12, 4.14, 4.15, and 4.16, we arrive at the following conclusions. Torque

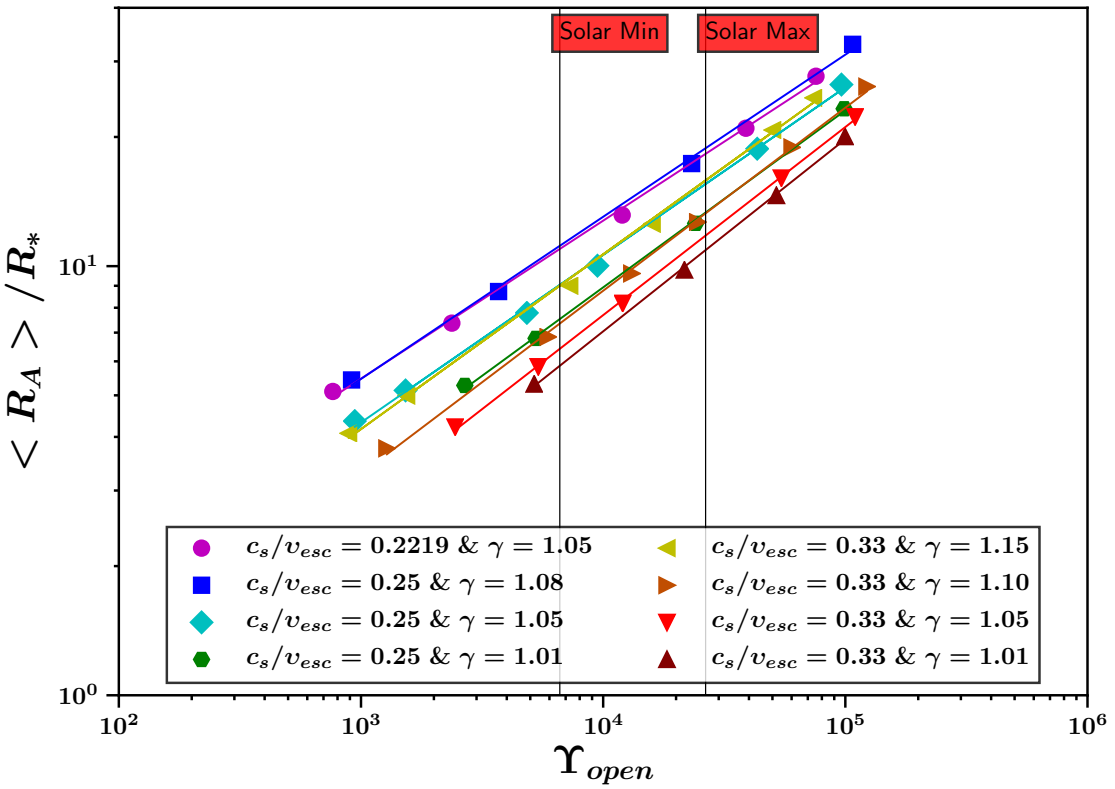

Figure 4.11: $< R_A > /R_*$ versus parameter Υ_{open}. Circles (magenta) represent simulations $c_s/v_{esc} = 0.2219$ and $\gamma = 1.05$. Squares (blue), diamonds (cyan), and hexagons (green) correspond to cases with $c_s/v_{esc} = 0.25$ and $\gamma = 1.08$, 1.05, 1.01, respectively. Pointing-left (yellow), pointing-right (brown), pointing-down (red), and pointing-up (dark red) triangles represent cases with $c_s/v_{esc} = 0.33$ and $\gamma = 1.15$, 1.10, 1.05, 1.01, respectively. Eight different power laws (solid lines) are presented, one for each wind model with given combination of coronal temperature and polytropic index. For a given value of Υ_{open}, the wind that is the faster at the Alfvén radius, has a smaller size of $< R_A > /R_*$, and therefore applies a weaker magnetic torque to the stellar surface. The black vertical lines, labelled as "Solar Min" and "Solar Max", show the Υ_{open} values of the Sun during the minimum and maximum of sunspot cycle 23, respectively.

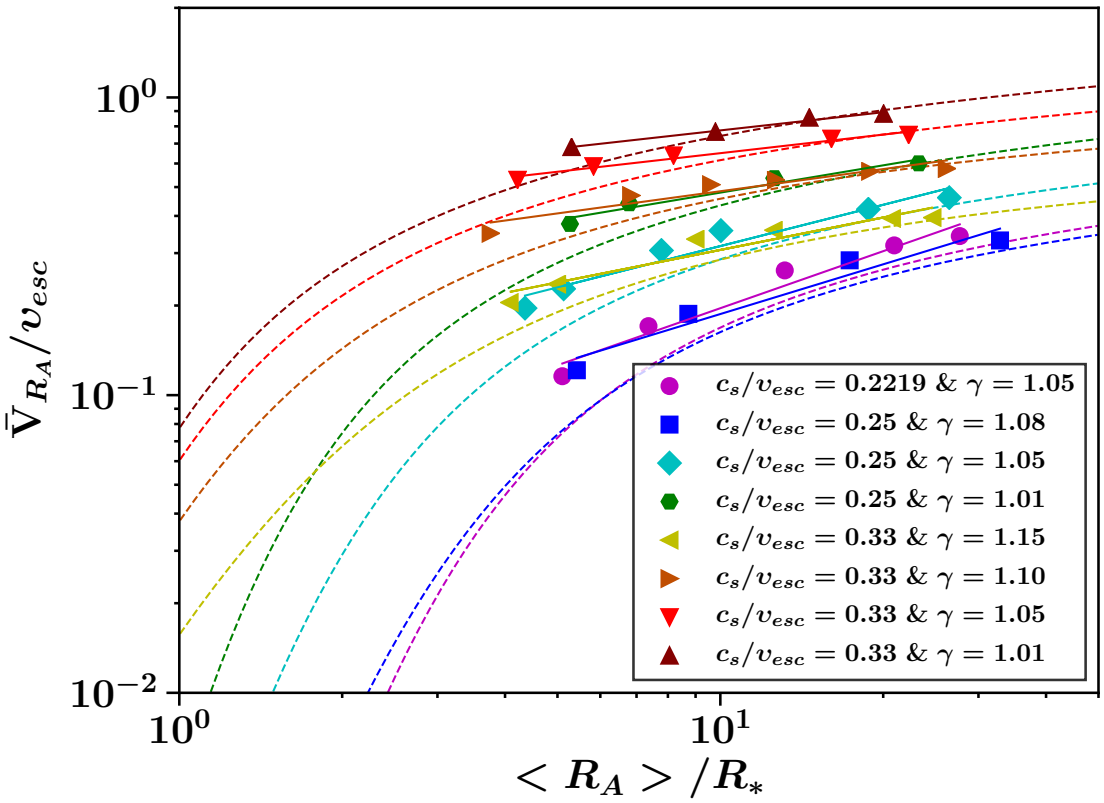

Figure 4.12: $\bar{V}_{R_A}/v_{esc}$ versus $< R_A > /R_*$ of for all the simulations presented in this chapter. Colors/symbols are the same as in figure 4.11. Eight different scaling laws are shown, and each one corresponds to a given combination of c_s/v_{esc} and γ. The solid lines represent the fitting function (3.28). The dashed lines show the velocity laws of the 1D, hydrodynamic, winds illustrated in figure 4.9.

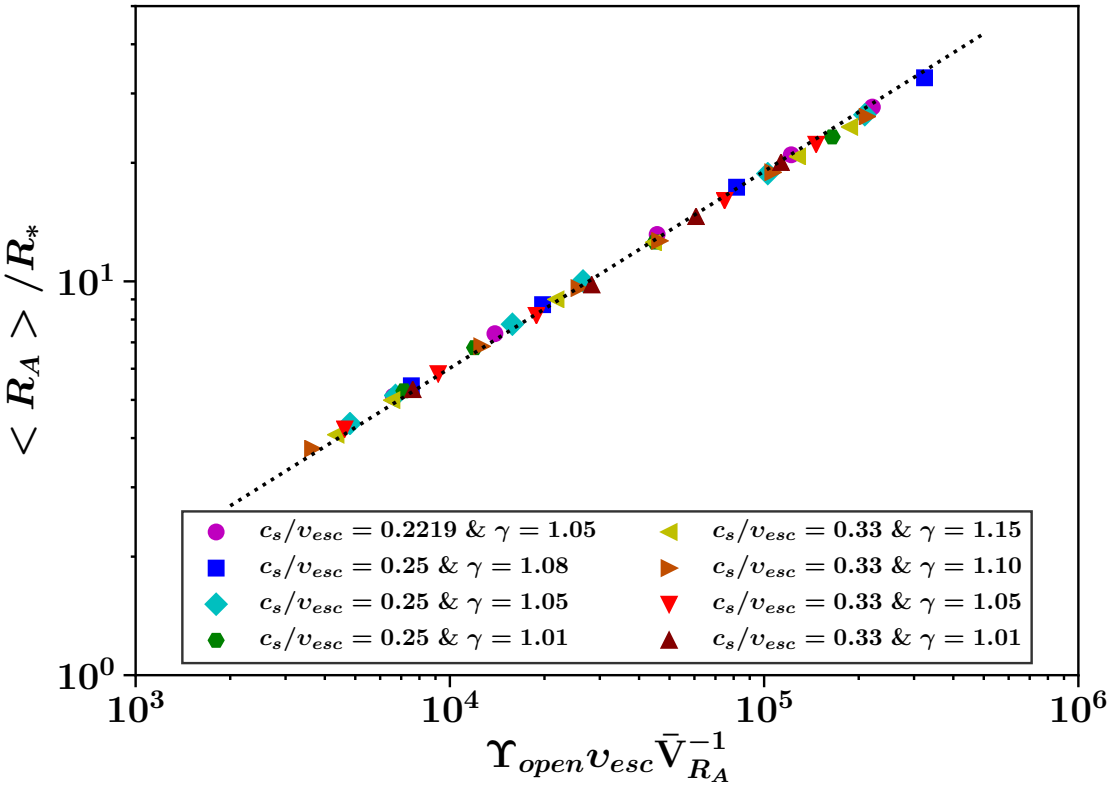

Figure 4.13: $< R_A > /R_*$ versus $\Upsilon_{open} v_{esc} \bar{V}_{R_A}^{-1}$. Colors/symbols are the same as in figure 4.11. All the simulation data can be represented by a single fitting law (dotted line), given by equation (3.26).

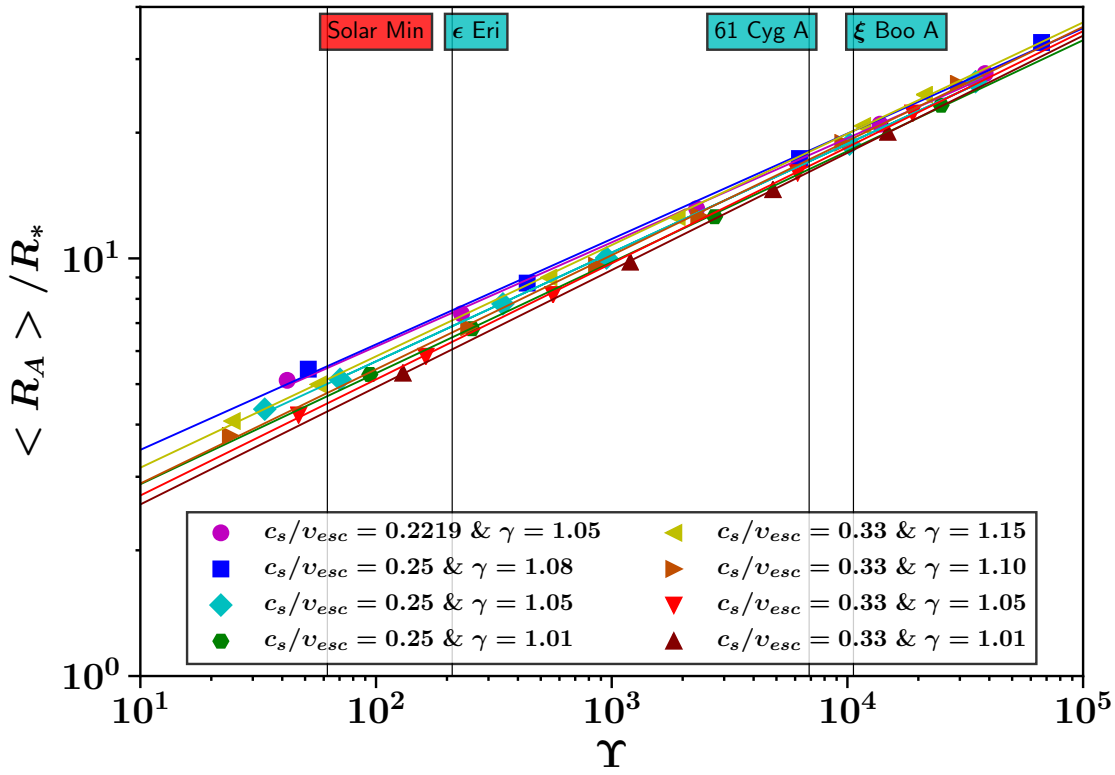

Figure 4.14: $< R_A > /R_*$ versus parameter Υ. Colors/symbols are the same as in figure 4.11. Each set simulations with a different combination of c_s/v_{esc} and γ scales as a different power law with Υ for various surface magnetic field strengths. The black vertical lines correspond to the Υ values of the Sun (during the minimum of sunspot cycle 23), ϵ Eri, 61 Cyg A, and ξ Boo A, respectively (see also table 4.5).

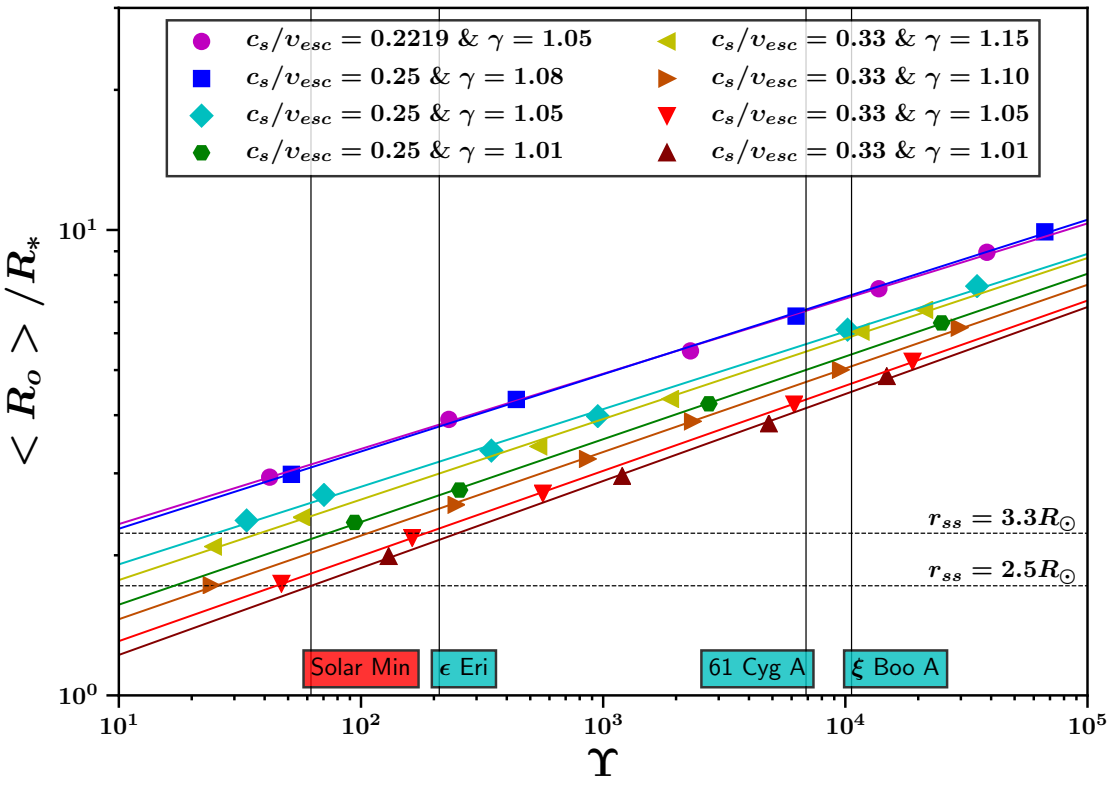

Figure 4.15: $< R_o > /R_*$ versus parameter Υ. Colors/symbols are the same as in figure 4.11. The plot shows eight power laws, one for each combination of c_s/v_{esc} and γ. For a given Υ, the acceleration profiles, studied here, produce a range of ~ 2 in the effective open-field radius, for dipolar fields. The black vertical lines have the same meaning as in figure 4.14. The horizontal black dashed lines correspond to the inverse of the solar fractional magnetic open flux, according to equation (4.11), where r_{ss} is the solar source surface.

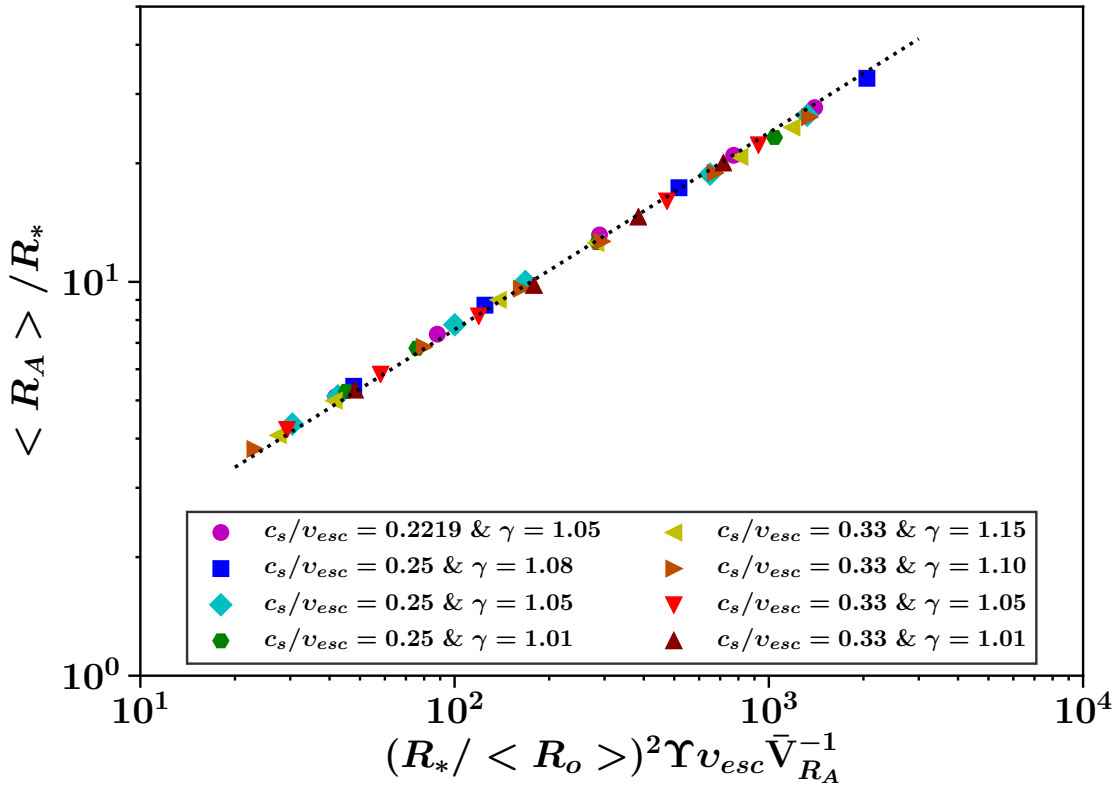

Figure 4.16: $< R_A > /R_*$ versus the quantity $(R_*/ < R_o >)^{-2} \Upsilon v_{esc} \bar{V}_{R_A}$. Colors/symbols are the same as in figure 4.11. The simulation data collapse in a single braking law. The fitting function (dotted line) is given by equation (4.6).

	Sun		61 Cyg A	ϵ Eri	ξ Boo A
	Minimum	Maximum			
Sp. Type	G2V		K5V	K2V	G8V
$R_*(R_\odot)$	1		0.67	0.74	0.86
$M_*(M_\odot)$	1		0.66	0.86	0.93
f	0.004		0.002	0.008	0.02
$B^2_{dip}(\mathrm{G}^2)$	1×10^0	...	1.2×10^2	2×10^2	1.2×10^3
$\dot{M}_w(\dot{M}_\odot)$	1	1.5	0.5	30	5
Υ	62.2	...	6880	210	10600
Υ_{open}	6620	26500	...	...	...
$< R_o > /R_*$	1.72 - 3.09	...	4.14 - 6.75	2.16 - 3.78	4.49 - 7.25
$< R_A > /R_*$	4.30 - 5.52	...	16.1 - 18.01	6.06 - 7.51	18.2 - 20.2
	5.86 - 11.2	10.9 - 18.8	...	...	...
$\tau_w(\times 10^{30}\mathrm{erg})$	0.294 - 0.484	...	0.757 - 0.957	26.0 - 40.0	97.2 - 120
	0.545 - 1.98	1.97 - 6.22	...	...	...

Table 4.5: Stellar parameters and wind global properties of the stars studied in this work. The stellar mass, radius, and spin rate as a fraction of the break-up speed, f, of 61 Cyg A, ϵ Eri, and ξ Boo A were adopted from Finley et al. (2019). We choose the values of the solar magnetic field and open flux, during sunspot cycle 23, based on the analysis by Finley et al. (2018). B^2_{dip} for 61 Cyg A is computed from its magnetic properties shown in Boro Saikia et al. (2016). The averaged squared dipolar field strengths of ϵ Eri and ξ Boo A are taken from Vidotto et al. (2016). The solar-wind mass loss rate during the minimum and maximum is taken from Wang (1998), where $\dot{M}_\odot = 2 \times 10^{-14} M_\odot \mathrm{yr}^{-1}$. The wind mass loss rates of 61 Cyg A, ϵ Eri, and ξ Boo A are from Wood et al. (2005a) and Wood et al. (2005b).

prescriptions that are based on parameter Υ, require both $< R_o >$ and $\bar{\mathrm{V}}_{R_A}$ to be known, in order to be applicable for any wind with a given acceleration profile. For a given value of Υ, a faster flow at every r, exerts a weaker torque on the star. For wind models with acceleration profiles such as the cases with $c_s/v_{esc} = 0.25$, $\gamma = 1.05$ and $c_s/v_{esc} = 0.33$, $\gamma = 1.15$ (see cyan and yellow velocity laws, respectively, in figure 4.12), the $< R_A >$-versus-Υ_{open} (compared to the $< R_A >$-versus-Υ) space illustrates more clearly the dependence of the effective Alfvén radius (and the resulting torque) on the flow thermodynamics, due to the power-law dependence of $< R_o >$ on Υ, which appear implicitly in K_s and m_s.

In the last part of this section, we apply the scaling laws (3.15), (3.18), and (4.4) to the Sun and three other low-mass, main-sequence stars: 61 Cyg A, ϵ Eri, and ξ Boo A. The parameters (i.e., stellar mass, radius, and spin rate as a fraction of the break-up

speed) of these three stars are taken from Finley et al. (2019, see also references therein), and are listed in Table 4.5.

During the solar minimum of sunspot cycle 23, Finley et al. (2018) computed the dipolar field strength (at the pole) to vary between 2 - 3 G. Parameter Υ, which is included in the scaling law (3.15), requires the dipolar field strength at the equator. Therefore, we use $B_* = 1$ G as the solar equatorial field strength at the minimum of cycle 23 (see fifth row of Table 4.5). The solar mass loss rate at the minimum is taken to be $\dot{M}_\odot = 2 \times 10^{-14} M_\odot \mathrm{yr}^{-1}$. These two values combined with the solar parameters given in Table 4.5 (see also section 3.3.2) yield a value of $\Upsilon = 62.2$ (see the vertical line labelled as "Solar Min" in figure 4.14 and the seventh row of Table 4.5). This value of Υ gives a range in $< R_A > /R_*$ between 4.30 and 5.52 (see the tenth row of Table 4.5), and using the torque formula (3.43), we predict a torque of $0.294 - 0.484 \times 10^{30}$ erg at solar minimum (see the twelfth row of Table 4.5). For this first demonstration we focused only at the solar minimum, when the solar dipolar field dominates over other higher order field geometries (see e.g., DeRosa et al. 2012; Finley et al. 2018), because the braking law (3.15) show a dependence on the field geometry. Finley et al. (2018) show that the solar open flux during cycle 23 is $\sim 5 \times 10^{22}$ and $\sim 10 \times 10^{22}$ at the minimum and maximum, respectively. The solar-mass-loss rate increases at solar maximum and a value of $3 \times 10^{-14} M_\odot \mathrm{yr}^{-1} = 1.5 \dot{M}_\odot$ is adopted. Then Υ_{open} is estimated to be 6620 and 26500 at minimum and maximum, respectively (see the vertical lines labelled as "Solar Min" and "Solar Max" in Figure 4.11 and the eighth row of Table 4.5). Therefore, we predict a range of $< R_A > /R_*$ that varies between 5.86 - 11.2 and 10.9 - 18.8 at minimum and maximum, respectively (see also the eleventh row of Table 4.5). Using the torque formula (3.44), we estimate the solar torque to be $0.545 - 1.98 \times 10^{30}$ erg at minimum and $1.97 - 6.22 \times 10^{30}$ erg at maximum, during cycle 23 (see the thirteenth row of Table 4.5). The fact that the two formulae (i.e., equation (3.43) that is based on the surface flux and equation (3.44) that is based on the open flux) provide a solar-torque estimation that differs by a factor of 2 or more at minimum, for a given flow acceleration profile, is due to the well known solar open flux problem (see e.g., Linker et al. 2017). Solar-wind models cannot reproduce the observed solar magnetic open flux. This can be understood as either a consequence of underestimating the solar surface magnetic field strength or due to solar active regions contributing to the open flux (via

magnetic reconnection at the boundaries between coronal holes and helmeted streamers, see e.g., Linker et al. 2017).

We also attempt to predict the effective open-field radius, $< R_o > /R_*$, during the solar minimum of cycle 23. In our work, $< R_o > /R_*$ is the inverse of the fractional open flux of a dipolar magnetosphere and therefore, it does not correspond to the exact radius at which the wind stretches the stellar magnetic field into a radial configuration (i.e., split monopole). In solar and stellar physics, a model that predicts the amount of the magnetic open flux is the potential field source surface (PFSS) model (Altschuler and Newkirk 1969). Assuming that the magnetic field is potential (i.e., current free), the PFSS method uses a solar/stellar magnetogram to extrapolate the magnetic field towards the source surface. Above the source surface the magnetic field lines are taken to follow a radial geometry and carry a wind. Studies have shown that PFSS and MHD models give different answers on the open-field radius of the solar wind (see e.g., review by Wiegelmann et al. 2017). For the Sun a typical value of the source surface is $2.5R_\odot$ (Hoeksema et al. 1983). However, Arden et al. (2014) showed that this value needs to be increased by $15 - 30\%$ during the solar minimum of cycle 23 in order to match the observed solar open flux. In order to compare our predictions for the solar fractional open flux with the ones derived from PFSS models, we use the formula from See et al. (2018), which expresses the amount of the fractional open flux of a dipolar field as a function of the source surface, r_{ss}. This relation is

$$\frac{\Phi_{open}}{\Phi_*} = \frac{3r_{ss}^2}{2r_{ss}^3 + 1}. \tag{4.11}$$

From above, the value of Υ, during the minimum of the solar sunspot cycle 23, is 62.2 and equation (4.4) predicts $< R_o > /R_\odot$ to vary between 1.72 and 3.09 (see also the ninth row of Table 4.5). Following Hoeksema et al. (1983) and Arden et al. (2014), we take the solar source surface to be $r_{ss} = 2.5 - 3.3R_\odot$. Then equation (4.11) gives $< R_o > /R_\odot$ to be between 1.72 and 2.23 (see the black dashed lines in figure 4.15). Clearly the flow acceleration profiles studied here bracket the solar fractional open flux. We do not attempt to predict $< R_o > /R_\odot$ during the solar maximum because studies show that more complex field geometries affect the amount of the wind magnetic open flux (Finley and Matt 2018).

61 Cyg A (HD 201091) is a K5V star with an age of $\sim$ 2 Gyrs (see e.g., Barnes 2007; Mamajek and Hillenbrand 2008; Marsden et al. 2014). From the Wood et al. (2005a) and Wood et al. (2005b) sample, 61 Cyg A was observed to exhibit a mass loss rate of $0.5\dot{M}_{\odot}$. Boro Saikia et al. (2016) measured the total averaged field strength of 61 Cyg A, during its minimum activity, to be $B_{mean} = 12$ G. 85% of the magnetic field is in the dipolar component. Therefore in order to extract the average dipolar field strength we use the formula from Finley et al. (2019), which is $B_{mean,dip} \approx B_{mean} f_{dip}^{1/2}$, where f_{dip} is the fraction of the dipolar field energy to the total field energy (see e.g., Boro Saikia et al. 2016; Vidotto et al. 2016, and the fifth row of table 4.5). We find an Υ value of 6880 (see the black verical line labelled as "61 Cyg A" in figures 4.14 and 4.15), which gives an $< R_A > /R_*$ from 16.1 to 18.01 and a magnetic torque that ranges from 0.757 to 0.957 $\times 10^{30}$erg (see also table 4.5). Lastly, the effective open field radius, $< R_o > /R_*$, is found to be between 4.14 and 6.75 (see also table 4.5).

ϵ Eri (HD 22049) is a K2V star with an age estimation of 400 Myrs (Barnes 2007; Mamajek and Hillenbrand 2008). Vidotto et al. (2016, see also references therein) computed the averaged squared dipolar field strength of this star to be 2×10^2 G^2 (see the fifth row of Table 4.5), with 75% of the field being in the dipolar component. Wood et al. (2005a) and Wood et al. (2005b) measured the wind mass loss rate from ϵ Eri to be $30\dot{M}_{\odot}$. Furthermore, Johnstone and Güdel (2015) estimate an average coronal temperature for ϵ Eri of 3.48 MK. We compute an Υ value that is 210 (see the black vertical line labelled as "ϵ Eri" in figures 4.14 and 4.15), which yields an effective lever arm, $< R_A > /R_*$, of 6.06 - 7.51 and a braking torque of 26 - 40 $\times 10^{30}$erg (see also Table 4.5). $< R_o > /R_*$ is predicted to range from 2.16 to 3.78 (see also Table 4.5).

ξ Boo A (HD 131156A) is a G8V and studies estimate to be 200Myrs old (Barnes 2007; Mamajek and Hillenbrand 2008). The averaged squared dipolar field strength of ξ Boo A was computed to be 1.2×10^3 G^2 (see the fifth row of Table 4.5) and 40% of this magnetic field is in the dipolar component (Vidotto et al. 2016, see also references therein). The wind mass loss rate is etsimated to be $5\dot{M}_{\odot}$ (Wood et al. 2005a; Wood et al. 2005b), and Johnstone and Güdel (2015) predicts an average coronal temperature of 4.37 MK. These paremeters yield a value of $\Upsilon = 10600$ (see the black vertical line labelled

as "ξ Boo A" in figures 4.14 and 4.15). This value of the wind magnetization predcits $< R_A > /R_*$ to range from 18.2 to 20.2, a stellar torque of 97.2 - 120 $\times 10^{30}$erg, and an effective open-field radius, $< R_o > /R_*$, of 4.49-7.25 (see also table 4.5).

Closing this section, we should mention that the field strengths used to estimate the magnetic torques of 61 Cyg A, ϵ Eri, and ξ Boo correspond to averaged dipolar field strengths. These averaged values were inferred by considering both the poloidal and toroidal component of these stellar dipolar fields. Our torque formula, based on parameter Υ, is a function of the dipolar poloidal field strength at the equator. Therefore all the quantities (i.e., $< R_A > /R_*$, τ_w, $< R_o > /R_*$) derived above should be understood as an upper limit and more detailed analysis is required in order to further verify the accuracy of these results.

4.5 Summary and Conclusions

This work employed 2.5D, ideal MHD, axisymmetric numerical simulations. We presented 40 new wind simulations in total, all of them carried out with a more accurate numerical setup. For the first part of this work, we investigated how the numerical accuracy of our simulations can affect the stellar torque prescriptions presented in Chapter 3. We completed 16 simulations to reproduce that parameter study on the coronal temperature. In the second part of this work, we completed 24 new simulations, in which we varied both the coronal temperature and the flow polytropic index. We considered 5 new wind models, and for each wind model, with a given combination of temperature and polytropic index, we varied the surface magnetic field strength. All the simulations used dipolar field geometries and were limited to slow rotators. The following points summarize the main conclusions in this work.

1. Torque prescriptions which are based on parameter Υ_{open} or the amount of the total open magnetic flux are less sensitive to the numerical accuracy of the simulations. This comes as a consequence of the fact that the fitting constants K_o, m_o, which determime the amount of the angular-momentum-loss rate (see also equations (3.44) and (3.46)) only depend on the values of K_q and q. However, the new stellar-wind setup produces simulations of better numerical accuracy simulation, and therefore,

the new values of K_o, m_o and Kq, q are more suitable for predicting torques using equations (3.44) and (3.46).

2. Torque prescriptions which are based on parameter Υ or the surface dipole strength are very sensitive to the numerical accuracy of the simulations. The new values of K_s, m_s were explained by the power-law dependence of $< R_A > /R_*$ on $< R_o > /R_*$ or $< R_o > /R_*$ on Υ. Similarly, the values of K_s and m_s are clearly more suitable for torque presciptions given by equation (3.43). Furthermore, we derived a fitting function based on Υ (see equation 4.6), which collapses the data in a single braking law independent of the flow energetics, but now requires both $< R_o >$ and $\bar{\mathrm{V}}_{R_A}$ to be known quantities.

3. By considering five new flow acceleration profiles (and eight in total), with different values of both the coronal temperature and polytropic index, we verified that all the analysis, presented in Chapter 3 and in the previous sections, can be expanded for any polytropic wind model, from a slow-rotating star with an axisymmteric, dipolar field.

4. Using the power-law dependence of $\bar{\mathrm{V}}_{R_A}$ on $< R_A > /R_*$ and $< R_o > /R_*$ on Υ, we rederive the form of equation (3.45). By combining equations (3.2) and (4.6) we obtain

$$\tau_w = \left(\frac{K_l^2}{C_o^2 K_q}\right)^{2/(2+q)} \Omega_* \upsilon_{esc}^{(4p_o-2)/(2+q)} \dot{M}_w^{(q-4p_o)/(2+q)} \times R_*^{(8-8p_o+2q)/(2+q)} B_*^{(4-8p_o)/(2+q)}. \tag{4.12}$$

Equation (4.12) predicts the stellar torque exerted on the star, for axisymmetric dipolar fields, slow rotators, and for the 8 acceleration profiles, considered in this work. The values of the fitting constants K_q, q, C_o, p_o, and K_l can be found in Tables 4.2, 4.4, and section 4.4.2, respectively.

Chapter 5

Conclusions

In this work we investigated the effects of the wind energetics on the magnetcic braking of late-type stars that are slow rotators. For polytropic winds, the two critical parameters, which determine the flow energetics (and the resulting wind velocity and acceleration profiles) are the coronal temperature and the polytropic index. In total, 70 2.5D, axisymmetric, ideal MHD, wind simulations, were presented. We studied, 8 different wind models, with different values of c_s/v_{esc} (i.e., coronal temperature) and γ, with dipolar fields, using a fixed stellar spin rate close to the solar one. For each wind model considered here, a parameter study on the surface magnetic field strength was completed.

The main conclusion of this work is the following. *For stellar winds having an amount of total open magnetic flux and mass-loss rate, the wind that is the faster at the Alfvén surface, regardless of how the flow is heated and expands, has the smaller magnetic lever arm, and therefore exerts the weaker torque on the stellar surface.*

It was demonstrated that for braking laws, which depends on parameter Υ_{open} (or the amount of the total open magnetic flux), the key parameter that needs to be included, in order these formulae to be independent of effects due to different wind energetics, is the wind speed at the Alfvén surface, $\bar{\mathrm{V}}_{R_A}$. Similarly, for braking laws, which depend on paramater Υ (or the surface dipole field strength), both $\bar{\mathrm{V}}_{R_A}$ and the effective open-field radius, $< R_o > /R_*$, needs to be included.

We derived 4 new torque formulae (see equations (3.43), (3.44), (3.46), and (4.12)), which predict the stellar magnetic braking for different flow thermodynamics. These prescriptions either provide the stellar magnetic torque for each wind model studied here or give a range in the resulting stellar torque produced by these models. Therefore, these relations are useful for rotational evolution studies.

We examined the accuracy of our simulations by improving our stellar-wind numerical setup. We concluded that torque prescriptions, which depend on parameter Υ_{open} are less sensitive to systematic errors due to the accuracy of the numerical simulations. Thus these formulae should provide more accurate stellar torque estimations.

Holzwarth and Jardine (2007) introduced scaling laws between the stellar angular velocity and the coronal temperature. Such relationships can provide an applicability of our torque prescriptions in the angular-momentum-evolution modeling (see e.g., Gallet and Bouvier 2013). The main limitation of this study is that all our simulations consider slow rotators. Therefore, future work is needed to expand our studies in the fast-magnetic-rotator regime. Matt et al. (2012a) showed that megnetocentrfugal effects are important in torque estimations when the star is rotating at $\sim 10\%$ of its break-up speed. However this work used fixed thermodynamics. Therefore investigating whether this threshold is a global one or depdends on the wind thermodynamics is required. For example Mestel and Spruit (1987) introduced an approximate form for the wind speed at the Alfvén surface, which depends on both the wind thermodynamics and the stellar rotation rate. Therefore, such a study will provide a better definition on whether a star can be considered as a fast or slow rotator for torque estimations.

Employing more realistic wind models, in order to test the accuracy of the torque prescriptions presented here, is also needed. While our torque scaling laws treat some of the global wind parameters (e.g., wind mass loss rate, open flux, wind speed at the Alfvén surface) as free parameters, the exact scalings (i.e., the fitting constants) we obtain are model dependent and based on the polytropic approximation used here. Over the last years, studies has started to adopt more realistic coronal heating models in their wind simulations (see e.g., Cohen et al. 2007; Cohen and Drake 2014; Garraffo et al. 2015; Alvarado-Gómez et al. 2016). Therefore, development of our work into this direction will

add another layer of consistency in our simulations and torque prescriptions, and most likely will open a new unexplored parameter space.

As mentioned in the introduction classical T-Tauri stars magnetically interact with their surrounding disks and due to both accretion and contraction, they are expected to spin-up during their pre-main-sequence life. However observations suggest that these stars are in spin equilibrium, indicative of processes, which effectively brake the stellar rotation (see e.g., Bouvier et al. 2014). In the literature, various mechanisms (e.g., stellar winds, magnetospheric ejections, disk winds) have been proposed to explain this phenomenon (see e.g., Romanova and Owocki 2015). Simulation show that the presence of magnetospheric ejections confine the stellar wind expansion, resulting in a jet-like geometry of the outflow (Zanni and Ferreira 2013). This specific geometry of the stellar wind might have an impact on the plasma speed and acceleration and therefore, on the location of the Alfvén radius. Therefore expanding our parameter studies during the T-Tauri phase of late-type stars, employing star-disk-ineraction simulations in order to derive stellar-wind braking laws, might provide useful insights on the angular momentum evolution problem of young late-type stars.

In conclusion, we still have a big parameter space that needs to be explored in order to quantify in more detail how stellar-wind torques apply on late-type stars, during all the phases of their lifes.

.

Bibliography

Altschuler, M. D., and G. Newkirk. 1969. 'Magnetic Fields and the Structure of the Solar Corona. I: Methods of Calculating Coronal Fields.' Sol. Phys. 9 (September): 131–149.

Alvarado-Gómez, J. D., G. A. J. Hussain, O. Cohen, et al. 2016. 'Simulating the environment around planet-hosting stars. II. Stellar winds and inner astrospheres.' A&A 594 (October): A95.

Amard, L., A. Palacios, C. Charbonnel, F. Gallet, and J. Bouvier. 2016. 'Rotating models of young solar-type stars. Exploring braking laws and angular momentum transport processes.' A&A 587 (March): A105.

Antiochos, S. K., J. A. Linker, R. Lionello, et al. 2012. 'The Structure and Dynamics of the CoronaHeliosphere Connection.' Space Sci. Rev. 172 (November): 169–185.

Antiochos, S. K., Z. Mikić, V. S. Titov, R. Lionello, and J. A. Linker. 2011. 'A Model for the Sources of the Slow Solar Wind.' ApJ 731 (April): 112.

Arden, W. M., A. A. Norton, and X. Sun. 2014. 'A "breathing" source surface for cycles 23 and 24.' *Journal of Geophysical Research (Space Physics)* 119 (March): 1476–1485.

Aschwanden, M. J. 2005. *Physics of the Solar Corona. An Introduction with Problems and Solutions (2nd edition).* Springer-Verlag Berlin Heidelberg, December.

Balick, B., and A. Frank. 2002. 'Shapes and Shaping of Planetary Nebulae.' ARA&A 40:439–486.

Balsara, D. S., and D. S. Spicer. 1999. 'A Staggered Mesh Algorithm Using High Order Godunov Fluxes to Ensure Solenoidal Magnetic Fields in Magnetohydrodynamic Simulations.' *Journal of Computational Physics* 149 (March): 270–292.

Baraffe, I., G. Chabrier, F. Allard, and P. H. Hauschildt. 1998. 'Evolutionary models for solar metallicity low-mass stars: mass-magnitude relationships and color-magnitude diagrams.' A&A 337 (September): 403–412.

Barnes, S. A. 2003. 'On the Rotational Evolution of Solar- and Late-Type Stars, Its Magnetic Origins, and the Possibility of Stellar Gyrochronology.' ApJ 586 (March): 464–479.

———. 2007. 'Ages for Illustrative Field Stars Using Gyrochronology: Viability, Limitations, and Errors.' ApJ 669 (November): 1167–1189.

———. 2010. 'A Simple Nonlinear Model for the Rotation of Main-sequence Cool Stars. I. Introduction, Implications for Gyrochronology, and Color-Period Diagrams.' ApJ 722 (October): 222–234.

Belcher, J. W., and K. B. MacGregor. 1976. 'Magnetic acceleration of winds from solar-type stars.' ApJ 210 (December): 498–507.

Boro Saikia, S., S. V. Jeffers, J. Morin, et al. 2016. 'A solar-like magnetic cycle on the mature K-dwarf 61 Cygni A (HD 201091).' A&A 594 (October): A29.

Bouvier, J. 2013. 'Observational studies of stellar rotation.' In *EAS Publications Series,* edited by P. Hennebelle and C. Charbonnel, 62:143–168. EAS Publications Series. September.

Bouvier, J., S. P. Matt, S. Mohanty, et al. 2014. 'Angular Momentum Evolution of Young Low-Mass Stars and Brown Dwarfs: Observations and Theory.' *Protostars and Planets VI* (September): 433–450.

Brandt, J. C. 1970. *Introduction to the solar wind.* San Francisco: Freeman.

Brun, A. S., and M. K. Browning. 2017. 'Magnetism, dynamo action and the solar-stellar connection.' *Living Reviews in Solar Physics* 14 (September): 4.

Brun, A. S., R. A. Garcıa, G. Houdek, D. Nandy, and M. Pinsonneault. 2014. 'The Solar-Stellar Connection.' Space Sci. Rev. (November).

Castor, J. I., D. C. Abbott, and R. I. Klein. 1975. 'Radiation-driven winds in Of stars.' ApJ 195 (January): 157–174.

Cohen, O. 2011. 'The independency of stellar mass-loss rates on stellar X-ray luminosity and activity level based on solar X-ray flux and solar wind observations.' MNRAS 417 (November): 2592–2600.

Cohen, O., and J. J. Drake. 2014. 'A Grid of MHD Models for Stellar Mass Loss and Spin-down Rates of Solar Analogs.' ApJ 783 (March): 55.

Cohen, O., I. V. Sokolov, I. I. Roussev, et al. 2007. 'A Semiempirical Magnetohydrodynamical Model of the Solar Wind.' ApJL 654 (January): L163–L166.

Cox, N. L. J., F. Kerschbaum, A.-J. van Marle, et al. 2012. 'A far-infrared survey of bow shocks and detached shells around AGB stars and red supergiants.' A&A 537 (January): A35.

Cranmer, S. R. 2008. 'Winds of Main-Sequence Stars: Observational Limits and a Path to Theoretical Prediction.' In *14th Cambridge Workshop on Cool Stars, Stellar Systems, and the Sun,* edited by G. van Belle, 384:317. Astronomical Society of the Pacific Conference Series. April.

———. 2012. 'Self-Consistent Models of the Solar Wind.' Space Sci. Rev. 172 (November): 145–156.

Cranmer, S. R., M. Asgari-Targhi, M. P. Miralles, et al. 2015. 'The role of turbulence in coronal heating and solar wind expansion.' *Philosophical Transactions of the Royal Society of London Series A* 373 (April): 20140148–20140148.

Cranmer, S. R., S. E. Gibson, and P. Riley. 2017. 'Origins of the Ambient Solar Wind: Implications for Space Weather.' Space Sci. Rev. 212 (November): 1345–1384.

Cranmer, S. R., and S. H. Saar. 2011. 'Testing a Predictive Theoretical Model for the Mass Loss Rates of Cool Stars.' ApJ 741 (November): 54.

Cranmer, S. R., A. A. van Ballegooijen, and R. J. Edgar. 2007. 'Self-consistent Coronal Heating and Solar Wind Acceleration from Anisotropic Magnetohydrodynamic Turbulence.' ApJS 171 (August): 520–551.

Davenport, J. R. A. 2017. 'Rotating Stars from Kepler Observed with Gaia DR1.' ApJ 835 (January): 16.

De Moortel, I., and P. Browning. 2015. 'Recent advances in coronal heating.' *Philosophical Transactions of the Royal Society of London Series A* 373 (April): 20140269–20140269.

DeForest, C. E., T. A. Howard, and D. J. McComas. 2014. 'Inbound Waves in the Solar Corona: A Direct Indicator of Alfvén Surface Location.' ApJ 787 (June): 124.

DeRosa, M. L., A. S. Brun, and J. T. Hoeksema. 2012. 'Solar Magnetic Field Reversals and the Role of Dynamo Families.' ApJ 757 (September): 96.

Donati, J.-F., and S. F. Brown. 1997. 'Zeeman-Doppler imaging of active stars. V. Sensitivity of maximum entropy magnetic maps to field orientation.' A&A 326 (October): 1135–1142.

Donati, J.-F., and J. D. Landstreet. 2009. 'Magnetic Fields of Nondegenerate Stars.' ARA&A 47 (September): 333–370.

ud-Doula, A., and S. P. Owocki. 2002. 'Dynamical Simulations of Magnetically Channeled Line-driven Stellar Winds. I. Isothermal, Nonrotating, Radially Driven Flow.' ApJ 576 (September): 413–428.

Ud-Doula, A., S. P. Owocki, and R. H. D. Townsend. 2009. 'Dynamical simulations of magnetically channelled line-driven stellar winds - III. Angular momentum loss and rotational spin-down.' MNRAS 392 (January): 1022–1033.

ud-Doula, A., S. Owocki, R. Townsend, V. Petit, and D. Cohen. 2014. 'X-rays from magnetically confined wind shocks: effect of cooling-regulated shock retreat.' MNRAS 441 (July): 3600–3614.

ud-Doula, A., J. O. Sundqvist, S. P. Owocki, V. Petit, and R. H. D. Townsend. 2013. 'First 3DMHD simulation of a massive-star magnetosphere with application to Hα emission from ^{1} Ori C.' MNRAS 428 (January): 2723–2730.

Dupree, A. K. 1986. 'Mass Loss from Cool Stars.' *Mitteilungen der Astronomischen Gesellschaft Hamburg* 67:101.

Feldman, U., E. Landi, and N. A. Schwadron. 2005. 'On the sources of fast and slow solar wind.' *Journal of Geophysical Research (Space Physics)* 110 (July): A07109.

Finley, A. J., and S. P. Matt. 2017. 'The Effect of Combined Magnetic Geometries on Thermally Driven Winds. I. Interaction of Dipolar and Quadrupolar Fields.' ApJ 845 (August): 46.

———. 2018. 'The Effect of Combined Magnetic Geometries on Thermally Driven Winds. II. Dipolar, Quadrupolar, and Octupolar Topologies.' ApJ 854 (February): 78.

Finley, A. J., S. P. Matt, and V. See. 2018. 'The Effect of Magnetic Variability on Stellar Angular Momentum Loss. I. The Solar Wind Torque during Sunspot Cycles 23 and 24.' ApJ 864 (September): 125.

Finley, A. J., V. See, and S. P. Matt. 2019. 'The Effect of Magnetic Variability on Stellar Angular Momentum Loss II: The Sun, 61 Cygni A, ϵ Eridani, ξ Bootis A and τ Bootis A.' *arXiv e-prints* (March).

Fisk, L. A. 2003. 'Acceleration of the solar wind as a result of the reconnection of open magnetic flux with coronal loops.' *Journal of Geophysical Research (Space Physics)* 108 (April): 1157.

Folsom, C. P., J. Bouvier, P. Petit, et al. 2018. 'The evolution of surface magnetic fields in young solar-type stars II: the early main sequence (250-650 Myr).' MNRAS 474 (March): 4956–4987.

Gallet, F., and J. Bouvier. 2013. 'Improved angular momentum evolution model for solar-like stars.' A&A 556 (August): A36.

———. 2015. 'Improved angular momentum evolution model for solar-like stars. II. Exploring the mass dependence.' A&A 577 (May): A98.

Garraffo, C., J. J. Drake, and O. Cohen. 2015. 'Magnetic Complexity as an Explanation for Bimodal Rotation Populations among Young Stars.' ApJL 807 (July): L6.

Garraffo, C., J. J. Drake, and O. Cohen. 2016. 'The missing magnetic morphology term in stellar rotation evolution.' A&A 595 (November): A110.

Gilman, R. C. 1972. 'On the Coupling of Grains to the Gas in Circumstellar Envelopes.' ApJ 178 (December): 423–426.

Golub, L., and J. M. Pasachoff. 1997. *The Solar Corona.* September.

Güdel, M. 2004. 'X-ray astronomy of stellar coronae.' A&A Rev. 12 (September): 71–237.

Güdel, M., and Y. Nazé. 2009. 'X-ray spectroscopy of stars.' A&A Rev. 17 (September): 309–408.

Hall, J. C. 2008. 'Stellar Chromospheric Activity.' *Living Reviews in Solar Physics* 5 (March).

Hansteen, V. H., and M. Velli. 2012. 'Solar Wind Models from the Chromosphere to 1 AU.' Space Sci. Rev. 172 (November): 89–121.

Harper, G. 1996. 'Mass loss and winds from cool giants.' In *Cool Stars, Stellar Systems, and the Sun,* edited by R. Pallavicini and A. K. Dupree, 109:481. Astronomical Society of the Pacific Conference Series.

Hartmann, L. 2001. *Accretion Processes in Star Formation.* January.

Hartmann, L., and K. B. MacGregor. 1982. 'Protostellar mass and angular momentum loss.' ApJ 259 (August): 180–192.

Heinemann, M., and S. Olbert. 1978. 'Axisymmetric ideal MHD stellar wind flow.' J. Geophys. Res. 83 (June): 2457–2460.

Heyvaerts, J. 1996. 'Rotating MHD Winds.' In *Plasma Astrophysics,* edited by C. Chiuderi and G. Einaudi, 468:31. Lecture Notes in Physics, Berlin Springer Verlag.

Higginson, A. K., S. K. Antiochos, C. R. DeVore, P. F. Wyper, and T. H. Zurbuchen. 2017. 'Dynamics of Coronal Hole Boundaries.' ApJ 837 (March): 113.

Hoeksema, J. T., J. M. Wilcox, and P. H. Scherrer. 1983. 'The structure of the heliospheric current sheet - 1978-1982.' J. Geophys. Res. 88 (December): 9910–9918.

Höfner, S. 2015. 'Wind Acceleration in AGB Stars: Solid Ground and Loose Ends.' In *Why Galaxies Care about AGB Stars III: A Closer Look in Space and Time,* edited by F. Kerschbaum, R. F. Wing, and J. Hron, 497:333. Astronomical Society of the Pacific Conference Series. August.

Holzer, T. E. 1977. 'Effects of rapidly diverging flow, heat addition, and momentum addition in the solar wind and stellar winds.' J. Geophys. Res. 82 (January): 23–35.

———. 2005. 'Heating and Acceleration of the Solar Plasma (Tutorial Talk).' In *Solar Wind 11/SOHO 16, Connecting Sun and Heliosphere,* edited by B. Fleck, T. H. Zurbuchen, and H. Lacoste, 592:115. ESA Special Publication. September.

Holzwarth, V., and M. Jardine. 2007. 'Theoretical mass loss rates of cool main-sequence stars.' A&A 463 (February): 11–21.

Irwin, J., and J. Bouvier. 2009. 'The rotational evolution of low-mass stars.' In *The Ages of Stars,* edited by E. E. Mamajek, D. R. Soderblom, and R. F. G. Wyse, 258:363–374. IAU Symposium. June.

Jacobs, C., and S. Poedts. 2011. 'A polytropic model for the solar wind.' *Advances in Space Research* 48 (December): 1958–1966.

Jacques, S. A. 1977. 'Momentum and energy transport by waves in the solar atmosphere and solar wind.' ApJ 215 (August): 942–951.

Johnstone, C. P. 2017. 'On the fast magnetic rotator regime of stellar winds.' A&A 598 (February): A24.

Johnstone, C. P., and M. Güdel. 2015. 'The coronal temperatures of low-mass main-sequence stars.' A&A 578 (June): A129.

Johnstone, C. P., M. Güdel, I. Brott, and T. Lüftinger. 2015a. 'Stellar winds on the main-sequence. II. The evolution of rotation and winds.' A&A 577 (May): A28.

Johnstone, C. P., M. Güdel, T. Lüftinger, G. Toth, and I. Brott. 2015b. 'Stellar winds on the main-sequence. I. Wind model.' A&A 577 (May): A27.

Kawaler, S. D. 1988. 'Angular momentum loss in low-mass stars.' ApJ 333 (October): 236–247.

Keppens, R., and J. P. Goedbloed. 1999. 'Numerical simulations of stellar winds: polytropic models.' A&A 343 (March): 251–260.

———. 2000. 'Stellar Winds, Dead Zones, and Coronal Mass Ejections.' ApJ 530 (February): 1036–1048.

Klimchuk, J. A. 2006. 'On Solving the Coronal Heating Problem.' Sol. Phys. 234 (March): 41–77.

———. 2015. 'Key aspects of coronal heating.' *Philosophical Transactions of the Royal Society of London Series A* 373 (April): 20140256–20140256.

Kopp, R. A., and T. E. Holzer. 1976. 'Dynamics of coronal hole regions. I - Steady polytropic flows with multiple critical points.' Sol. Phys. 49 (July): 43–56.

Kraft, R. P. 1967. 'Studies of Stellar Rotation. V. The Dependence of Rotation on Age among Solar-Type Stars.' ApJ 150 (November): 551.

Krumholz, M. R. 2015. 'Notes on Star Formation.' *ArXiv e-prints* (November).

Krumholz, M. R., M. R. Bate, H. G. Arce, et al. 2014. 'Star Cluster Formation and Feedback.' *Protostars and Planets VI:* 243–266.

Kwok, S. 1994. 'Planetary nebulae: A modern view.' PASP 106 (April): 344–355.

Lamers, H. J. G. L. M., and J. P. Cassinelli. 1999. *Introduction to Stellar Winds.* Cambridge, UK: Cambridge University Press, June.

Lammer, H., and M. Blanc. 2018. 'From Disks to Planets: The Making of Planets and Their Early Atmospheres. An Introduction.' Space Sci. Rev. 214 (March): 60.

Lammer, H., and M. Khodachenko. 2015. *Characterizing Stellar and Exoplanetary Environments.* Springer, Cham.

Leer, E., and T. E. Holzer. 1980. 'Energy addition in the solar wind.' J. Geophys. Res. 85 (September): 4681–4688.

Li, J. 1999. 'Magnetic braking of the present Sun.' MNRAS 302 (January): 203–208.

Linker, J. A., R. M. Caplan, C. Downs, et al. 2017. 'The Open Flux Problem.' ApJ 848 (October): 70.

Linker, J. A., R. Lionello, Z. Mikić, V. S. Titov, and S. K. Antiochos. 2011. 'The Evolution of Open Magnetic Flux Driven by Photospheric Dynamics.' ApJ 731 (April): 110.

Lionello, R., C. Downs, J. A. Linker, et al. 2013. 'Magnetohydrodynamic Simulations of Interplanetary Coronal Mass Ejections.' ApJ 777 (November): 76.

Lionello, R., J. A. Linker, and Z. Mikić. 2009. 'Multispectral Emission of the Sun During the First Whole Sun Month: Magnetohydrodynamic Simulations.' ApJ 690 (January): 902–912.

Lovelace, R. V. E., C. Mehanian, C. M. Mobarry, and M. E. Sulkanen. 1986. 'Theory of axisymmetric magnetohydrodynamic flows - Disks.' ApJS 62 (September): 1–37.

Lovelace, R. V. E., M. M. Romanova, and A. W. Barnard. 2008. 'Planet migration and disc destruction due to magneto-centrifugal stellar winds.' MNRAS 389 (September): 1233–1239.

Low, B. C., and K. Tsinganos. 1986. 'Steady hydromagnetic flows in open magnetic fields. I - A class of analytic solutions.' ApJ 302 (March): 163–187.

Lüftinger, T., A. A. Vidotto, and C. P. Johnstone. 2015. 'Magnetic Fields and Winds of Planet Hosting Stars.' In *Characterizing Stellar and Exoplanetary Environments,* edited by H. Lammer and M. Khodachenko, 411:37. Astrophysics and Space Science Library.

MacGregor, K. B., and M. Brenner. 1991. 'Rotational evolution of solar-type stars. I - Main-sequence evolution.' ApJ 376 (July): 204–213.

Mamajek, E. E., and L. A. Hillenbrand. 2008. 'Improved Age Estimation for Solar-Type Dwarfs Using Activity-Rotation Diagnostics.' ApJ 687 (November): 1264–1293.

Marsden, S. C., P. Petit, S. V. Jeffers, et al. 2014. 'A BCool magnetic snapshot survey of solar-type stars.' MNRAS 444 (November): 3517–3536.

Matt, S. P., A. S. Brun, I. Baraffe, J. Bouvier, and G. Chabrier. 2015. 'The Mass-dependence of Angular Momentum Evolution in Sun-like Stars.' ApJL 799 (January): L23.

Matt, S. P., K. B. MacGregor, M. H. Pinsonneault, and T. P. Greene. 2012a. 'Magnetic Braking Formulation for Sun-like Stars: Dependence on Dipole Field Strength and Rotation Rate.' ApJL 754 (August): L26.

Matt, S. P., G. Pinzón, T. P. Greene, and R. E. Pudritz. 2012b. 'Spin Evolution of Accreting Young Stars. II. Effect of Accretion-powered Stellar Winds.' ApJ 745 (January): 101.

Matt, S., and R. E. Pudritz. 2008. 'Accretion-powered Stellar Winds. II. Numerical Solutions for Stellar Wind Torques.' ApJ 678 (May): 1109–1118.

McComas, D. J., N. Angold, H. A. Elliott, et al. 2013. 'Weakest Solar Wind of the Space Age and the Current "Mini" Solar Maximum.' ApJ 779 (December): 2.

McComas, D. J., R. W. Ebert, H. A. Elliott, et al. 2008. 'Weaker solar wind from the polar coronal holes and the whole Sun.' Geophys. Res. Lett. 35 (September): L18103.

McComas, D. J., H. A. Elliott, N. A. Schwadron, et al. 2003. 'The three-dimensional solar wind around solar maximum.' Geophys. Res. Lett. 30 (May): 24–1.

McComas, D. J., M. Velli, W. S. Lewis, et al. 2007. 'Understanding coronal heating and solar wind acceleration: Case for in situ near-Sun measurements.' *Reviews of Geophysics* 45 (March): RG1004.

Meibom, S., S. A. Barnes, D. W. Latham, et al. 2011. 'The Kepler Cluster Study: Stellar Rotation in NGC 6811.' ApJL 733 (May): L9.

Meibom, S., S. A. Barnes, I. Platais, et al. 2015. 'A spin-down clock for cool stars from observations of a 2.5-billion-year-old cluster.' Nature 517 (January): 589–591.

Mestel, L. 1961. 'A note on equatorial acceleration in a magnetic star.' MNRAS 122:473.

———. 1968. 'Magnetic braking by a stellar wind-I.' MNRAS 138:359.

———. 1984. 'Angular Momentum Loss During Pre-Main Sequence Contraction.' In *Cool Stars, Stellar Systems, and the Sun,* edited by S. L. Baliunas and L. Hartmann, 193:49. Lecture Notes in Physics, Berlin Springer Verlag.

———. 1999. *Stellar magnetism.* New York: Oxford University Press.

Mestel, L., and H. C. Spruit. 1987. 'On magnetic braking of late-type stars.' MNRAS 226 (May): 57–66.

Michel, F. C. 1969. 'Relativistic Stellar-Wind Torques.' ApJ 158 (November): 727.

Mignone, A., G. Bodo, S. Massaglia, et al. 2007. 'PLUTO: A Numerical Code for Computational Astrophysics.' ApJS 170 (May): 228–242.

Mikić, Z., J. A. Linker, D. D. Schnack, R. Lionello, and A. Tarditi. 1999. 'Magnetohydrodynamic modeling of the global solar corona.' *Physics of Plasmas* 6 (May): 2217–2224.

Nerney, S. F., and S. T. Suess. 1975. 'Restricted three-dimensional stellar wind modeling. I - Polytropic case.' ApJ 196 (March): 837–847.

Neugebauer, M., and C. W. Snyder. 1962. 'Solar Plasma Experiment.' *Science* 138 (December): 1095–1097.

———. 1966. 'Mariner 2 Observations of the Solar Wind, 1, Average Properties.' J. Geophys. Res. 71 (October): 4469.

Noyes, R. W., L. W. Hartmann, S. L. Baliunas, D. K. Duncan, and A. H. Vaughan. 1984. 'Rotation, convection, and magnetic activity in lower main-sequence stars.' ApJ 279 (April): 763–777.

O'Fionnagáin, D., and A. A. Vidotto. 2018. 'The solar wind in time: a change in the behaviour of older winds?' MNRAS 476 (May): 2465–2475.

Ofman, L. 2004. 'The origin of the slow solar wind in coronal streamers.' *Advances in Space Research* 33:681–688.

———. 2010. 'Wave Modeling of the Solar Wind.' *Living Reviews in Solar Physics* 7 (October): 4.

Okamoto, I. 1975. 'Magnetic braking by a stellar wind. V - Approximate determination of the poloidal field.' MNRAS 173 (November): 357–379.

Ollivier, M., F. Roques, F. Casoli, T. Encrenaz, and F. Selsis. 2009. *Planetary Systems.*

Owens, M. J., M. Lockwood, and P. Riley. 2017. 'Global solar wind variations over the last four centuries.' *Scientific Reports* 7 (January): 41548.

Owocki, S. P. 2009a. 'Radiation Hydrodynamics of Line-Driven Winds.' In *American Institute of Physics Conference Series,* edited by I. Hubeny, J. M. Stone, K. MacGregor, and K. Werner, 1171:173–186. American Institute of Physics Conference Series. September.

———. 2009b. 'Stellar Magnetospheres.' In *EAS Publications Series,* edited by C. Neiner and J.-P. Zahn, 39:223–254. EAS Publications Series.

———. 2015. 'Instabilities in the Envelopes and Winds of Very Massive Stars.' In *Very Massive Stars in the Local Universe,* edited by J. S. Vink, 412:113. Astrophysics and Space Science Library.

Owocki, S. P., A. ud-Doula, J. O. Sundqvist, et al. 2016. 'An 'analytic dynamical magnetosphere' formalism for X-ray and optical emission from slowly rotating magnetic massive stars.' MNRAS 462 (November): 3830–3844.

Pantolmos, G., and S. P. Matt. 2017. 'Magnetic Braking of Sun-like and Low-mass Stars: Dependence on Coronal Temperature.' ApJ 849 (November): 83.

Parker, E. N. 1958. 'Dynamics of the Interplanetary Gas and Magnetic Fields.' ApJ 128 (November): 664.

———. 1960. 'The Hydrodynamic Theory of Solar Corpuscular Radiation and Stellar Winds.' ApJ 132 (November): 821.

———. 1963. *Interplanetary Dynamical Processes.* New York: Interscience Publishers.

———. 1965. 'Dynamical Theory of the Solar Wind.' Space Sci. Rev. 4 (September): 666–708.

Parnell, C. E., and I. De Moortel. 2012. 'A contemporary view of coronal heating.' *Philosophical Transactions of the Royal Society of London Series A* 370 (July): 3217–3240.

Pasachoff, J. M., V. Rušin, M. Druckmüller, et al. 2009. 'The 2008 August 1 Eclipse Solar-Minimum Corona Unraveled.' ApJ 702 (September): 1297–1308.

Pauldrach, A., J. Puls, and R. P. Kudritzki. 1986. 'Radiation-driven winds of hot luminous stars - Improvements of the theory and first results.' A&A 164 (August): 86–100.

Petit, P., B. Dintrans, S. K. Solanki, et al. 2008. 'Toroidal versus poloidal magnetic fields in Sun-like stars: a rotation threshold.' MNRAS 388 (July): 80–88.

Petit, V., S. P. Owocki, G. A. Wade, et al. 2013. 'A magnetic confinement versus rotation classification of massive-star magnetospheres.' MNRAS 429 (February): 398–422.

Pizzo, V., R. Schwenn, E. Marsch, et al. 1983. 'Determination of the solar wind angular momentum flux from the HELIOS data - an observational test of the Weber and Davis theory.' ApJ 271 (August): 335–354.

Pizzolato, N., A. Maggio, G. Micela, S. Sciortino, and P. Ventura. 2003. 'The stellar activity-rotation relationship revisited: Dependence of saturated and non-saturated X-ray emission regimes on stellar mass for late-type dwarfs.' A&A 397 (January): 147–157.

Pneuman, G. W. 1966. 'Interaction of the Solar Wind with a Large-Scale Solar Magnetic Field.' ApJ 145 (July): 242.

Pneuman, G. W., and R. A. Kopp. 1971. 'Gas-Magnetic Field Interactions in the Solar Corona.' Sol. Phys. 18 (June): 258–270.

Powell, Kenneth G., Philip L. Roe, Timur J. Linde, Tamas I. Gombosi, and Darren L. De Zeeuw. 1999. 'A Solution-Adaptive Upwind Scheme for Ideal Magnetohydrodynamics.' *Journal of Computational Physics* 154 (2): 284–309.

Priest, E. 2014. *Magnetohydrodynamics of the Sun.* Cambridge, UK: Cambridge University Press, May.

Pudritz, R. E., and S. Matt. 2014. 'The Early History of Stellar Spin: the Theory of Accretion onto Young Stellar Objects.' In *European Physical Journal Web of Conferences,* 64:4001. European Physical Journal Web of Conferences. January.

Rappazzo, A. F., W. H. Matthaeus, D. Ruffolo, S. Servidio, and M. Velli. 2012. 'Interchange Reconnection in a Turbulent Corona.' ApJL 758 (October): L14.

Reiners, A., and S. Mohanty. 2012. 'Radius-dependent Angular Momentum Evolution in Low-mass Stars. I.' ApJ 746 (February): 43.

Réville, V., and A. S. Brun. 2017. 'Global Solar Magnetic Field Organization in the Outer Corona: Influence on the Solar Wind Speed and Mass Flux Over the Cycle.' ApJ 850 (November): 45.

Réville, V., A. S. Brun, S. P. Matt, A. Strugarek, and R. F. Pinto. 2015a. 'The Effect of Magnetic Topology on Thermally Driven Wind: Toward a General Formulation of the Braking Law.' ApJ 798 (January): 116.

Réville, V., A. S. Brun, A. Strugarek, et al. 2015b. 'From Solar to Stellar Corona: The Role of Wind, Rotation, and Magnetism.' ApJ 814 (December): 99.

Réville, V., C. P. Folsom, A. Strugarek, and A. S. Brun. 2016a. 'Age Dependence of Wind Properties for Solar-type Stars: A 3D Study.' ApJ 832 (December): 145.

———. 2016b. 'Superradially Expanding Flux Tubes Of Young Star'S Coronae.' In *19th Cambridge Workshop on Cool Stars, Stellar Systems, and the Sun (CS19),* 33. October.

Riley, P., J. A. Linker, Z. Mikić, et al. 2006. 'A Comparison between Global Solar Magnetohydrodynamic and Potential Field Source Surface Model Results.' ApJ 653 (December): 1510–1516.

Romanova, M. M., and S. P. Owocki. 2015. 'Accretion, Outflows, and Winds of Magnetized Stars.' Space Sci. Rev. 191 (October): 339–389.

Sadeghi Ardestani, L., T. Guillot, and P. Morel. 2017. 'A semi-empirical model for magnetic braking of solar-type stars.' MNRAS 472 (December): 2590–2607.

Sakurai, T. 1985. 'Magnetic stellar winds - A 2-D generalization of the Weber-Davis model.' A&A 152 (November): 121–129.

———. 1990. 'Magnetohydrodynamic solar/stellar wind models.' *Computer Physics Reports* 12 (May): 247–273.

Schatzman, E. 1962. 'A theory of the role of magnetic activity during star formation.' *Annales d'Astrophysique* 25 (February): 18.

Schwadron, N. A., and D. J. McComas. 2003. 'Solar Wind Scaling Law.' ApJ 599 (December): 1395–1403.

———. 2008. 'The Solar Wind Power from Magnetic Flux.' ApJL 686 (October): L33.

Sedlmayr, E., and C. Dominik. 1995. 'Dust Driven Winds.' Space Sci. Rev. 73 (August): 211–272.

See, V., M. Jardine, A. A. Vidotto, et al. 2015. 'The energy budget of stellar magnetic fields.' MNRAS 453 (November): 4301–4310.

See, V., M. Jardine, A. A. Vidotto, et al. 2016. 'The connection between stellar activity cycles and magnetic field topology.' MNRAS 462 (November): 4442–4450.

See, V., M. Jardine, A. A. Vidotto, et al. 2017. 'Studying stellar spin-down with Zeeman-Doppler magnetograms.' MNRAS 466 (April): 1542–1554.

See, V., M. Jardine, A. A. Vidotto, et al. 2018. 'The open flux evolution of a solar-mass star on the main sequence.' MNRAS 474 (February): 536–546.

Skumanich, A. 1972. 'Time Scales for CA II Emission Decay, Rotational Braking, and Lithium Depletion.' ApJ 171 (February): 565.

Smith, E. J., and A. Balogh. 2003. 'Open Magnetic Flux: Variation with Latitude and Solar Cycle.' In *Solar Wind Ten,* edited by M. Velli, R. Bruno, F. Malara, and B. Bucci, 679:67–70. American Institute of Physics Conference Series. September.

———. 2008. 'Decrease in heliospheric magnetic flux in this solar minimum: Recent Ulysses magnetic field observations.' Geophys. Res. Lett. 35 (November): L22103.

Sokolov, I. V., B. van der Holst, R. Oran, et al. 2013. 'Magnetohydrodynamic Waves and Coronal Heating: Unifying Empirical and MHD Turbulence Models.' ApJ 764 (February): 23.

Steinolfson, R. S., S. T. Suess, and S. T. Wu. 1982. 'The steady global corona.' ApJ 255 (April): 730–742.

Strassmeier, K. G. 2009. 'Starspots.' A&A Rev. 17 (September): 251–308.

Suzuki, T. K. 2007. 'Structured Red Giant Winds with Magnetized Hot Bubbles and the Corona/Cool Wind Dividing Line.' ApJ 659 (April): 1592–1610.

Suzuki, T. K., S. Imada, R. Kataoka, et al. 2013. 'Saturation of Stellar Winds from Young Suns.' PASJ 65 (October): 98.

Suzuki, T. K., and S.-i. Inutsuka. 2005. 'Making the Corona and the Fast Solar Wind: A Self-consistent Simulation for the Low-Frequency Alfvén Waves from the Photosphere to 0.3 AU.' ApJL 632 (October): L49–L52.

Suzuki, T. K., and S.-I. Inutsuka. 2006. 'Solar winds driven by nonlinear low-frequency Alfvén waves from the photosphere: Parametric study for fast/slow winds and disappearance of solar winds.' *Journal of Geophysical Research (Space Physics)* 111 (June): A06101.

Telleschi, A., M. Güdel, K. Briggs, et al. 2005. 'Coronal Evolution of the Sun in Time: High-Resolution X-Ray Spectroscopy of Solar Analogs with Different Ages.' ApJ 622 (March): 653–679.

Testa, P., S. H. Saar, and J. J. Drake. 2015. 'Stellar activity and coronal heating: an overview of recent results.' *Philosophical Transactions of the Royal Society of London Series A* 373 (April): 20140259–20140259.

Tielens, A. G. G. M., L. B. F. M. Waters, and T. J. Bernatowicz. 2005. 'Origin and Evolution of Dust in Circumstellar and Interstellar Environments.' In *Chondrites and the Protoplanetary Disk,* edited by A. N. Krot, E. R. D. Scott, and B. Reipurth, 341:605. Astronomical Society of the Pacific Conference Series. December.

Tokumaru, M., M. Kojima, and K. Fujiki. 2010. 'Solar cycle evolution of the solar wind speed distribution from 1985 to 2008.' *Journal of Geophysical Research (Space Physics)* 115 (April): A04102.

Toro, E. F. 2009. *Riemann Solvers and Numerical Methods for Fluid Dynamics.* Springer-Verlag: Berlin.

Tout, C. A., and J. E. Pringle. 1992. 'Spin-down of rapidly rotating, convective stars.' MNRAS 256 (May): 269–276.

Townsend, R. H. D., M. E. Oksala, D. H. Cohen, S. P. Owocki, and A. ud-Doula. 2010. 'Discovery of Rotational Braking in the Magnetic Helium-strong Star Sigma Orionis E.' ApJL 714 (May): L318–L322.

Tsinganos, K., T. Ray, and M. Stute. 2009. 'Protostellar Jets in Context.' *Astrophysics and Space Science Proceedings* 13.

Usmanov, A. V., M. L. Goldstein, B. P. Besser, and J. M. Fritzer. 2000. 'A global MHD solar wind model with WKB Alfvén waves: Comparison with Ulysses data.' J. Geophys. Res. 105 (June): 12675–12696.

Usmanov, A. V., M. L. Goldstein, and W. H. Matthaeus. 2016. 'A Four-fluid MHD Model of the Solar Wind/Interstellar Medium Interaction with Turbulence Transport and Pickup Protons as Separate Fluid.' ApJ 820 (March): 17.

Ustyugova, G. V., A. V. Koldoba, M. M. Romanova, V. M. Chechetkin, and R. V. E. Lovelace. 1999. 'Magnetocentrifugally Driven Winds: Comparison of MHD Simulations with Theory.' ApJ 516 (May): 221–235.

Vaiana, G. S., J. P. Cassinelli, G. Fabbiano, et al. 1981. 'Results from an extensive Einstein stellar survey.' ApJ 245 (April): 163–182.

van der Holst, B., I. V. Sokolov, X. Meng, et al. 2014. 'Alfvén Wave Solar Model (AWSoM): Coronal Heating.' ApJ 782 (February): 81.

van Saders, J. L., and M. H. Pinsonneault. 2013. 'Fast Star, Slow Star; Old Star, Young Star: Subgiant Rotation as a Population and Stellar Physics Diagnostic.' ApJ 776 (October): 67.

Veilleux, S., G. Cecil, and J. Bland-Hawthorn. 2005. 'Galactic Winds.' ARA&A 43 (September): 769–826.

Velli, M., F. Pucci, F. Rappazzo, and A. Tenerani. 2015. 'Models of coronal heating, turbulence and fast reconnection.' *Philosophical Transactions of the Royal Society of London Series A* 373 (April): 20140262–20140262.

Verdini, A., M. Velli, W. H. Matthaeus, S. Oughton, and P. Dmitruk. 2010. 'A Turbulence-Driven Model for Heating and Acceleration of the Fast Wind in Coronal Holes.' ApJL 708 (January): L116–L120.

Vidotto, A. A., J.-F. Donati, M. Jardine, et al. 2016. 'Could a change in magnetic field geometry cause the break in the wind-activity relation?' MNRAS 455 (January): L52–L56.

Vidotto, A. A., S. G. Gregory, M. Jardine, et al. 2014a. 'Stellar magnetism: empirical trends with age and rotation.' MNRAS 441 (July): 2361–2374.

Vidotto, A. A., M. Jardine, J. Morin, et al. 2014b. 'M-dwarf stellar winds: the effects of realistic magnetic geometry on rotational evolution and planets.' MNRAS 438 (February): 1162–1175.

Vidotto, A. A., M. Jardine, M. Opher, J. F. Donati, and T. I. Gombosi. 2011. 'Powerful winds from low-mass stars: V374 Peg.' MNRAS 412 (March): 351–362.

Vidotto, A. A., M. Opher, V. Jatenco-Pereira, and T. I. Gombosi. 2009. 'Three-dimensional Numerical Simulations of Magnetized Winds of Solar-like Stars.' ApJ 699 (July): 441–452.

Wang, Y.-M. 1998. 'Cyclic Magnetic Variations of the Sun.' In *Cool Stars, Stellar Systems, and the Sun,* edited by R. A. Donahue and J. A. Bookbinder, 154:131. Astronomical Society of the Pacific Conference Series.

Wang, Y.-M., Y.-K. Ko, and R. Grappin. 2009. 'Slow Solar Wind from Open Regions with Strong Low-Coronal Heating.' ApJ 691 (January): 760–769.

Wang, Y.-M., and N. R. Sheeley Jr. 1991. 'Why fast solar wind originates from slowly expanding coronal flux tubes.' ApJL 372 (May): L45–L48.

Washimi, H., and T. Sakurai. 1993. 'A simulation study of the solar wind including the solar rotation effect.' Sol. Phys. 143 (January): 173–186.

Washimi, H., and S. Shibata. 1993. 'Thermo-centrifugal wind from a rotating magnetic dipole.' MNRAS 262 (June): 936–944.

Weber, E. J., and L. Davis Jr. 1967. 'The Angular Momentum of the Solar Wind.' ApJ 148 (April): 217–227.

Wiegelmann, T., G. J. D. Petrie, and P. Riley. 2017. 'Coronal Magnetic Field Models.' Space Sci. Rev. 210 (September): 249–274.

Wood, B. E., J. L. Linsky, and M. Güdel. 2015. 'Stellar Winds in Time.' In *Characterizing Stellar and Exoplanetary Environments,* edited by H. Lammer and M. Khodachenko, 411:19. Astrophysics and Space Science Library.

Wood, B. E., H.-R. Müller, S. Redfield, and E. Edelman. 2014. 'Evidence for a Weak Wind from the Young Sun.' ApJL 781 (February): L33.

Wood, B. E., H.-R. Müller, G. P. Zank, and J. L. Linsky. 2002. 'Measured Mass-Loss Rates of Solar-like Stars as a Function of Age and Activity.' ApJ 574 (July): 412–425.

Wood, B. E., H.-R. Müller, G. P. Zank, J. L. Linsky, and S. Redfield. 2005a. 'New Mass-Loss Measurements from Astrospheric Lyα Absorption.' ApJL 628 (August): L143–L146.

Wood, B. E., S. Redfield, J. L. Linsky, H.-R. Müller, and G. P. Zank. 2005b. 'Stellar Lyα Emission Lines in the Hubble Space Telescope Archive: Intrinsic Line Fluxes and Absorption from the Heliosphere and Astrospheres.' ApJS 159 (July): 118–140.

Wright, N. J., J. J. Drake, E. E. Mamajek, and G. W. Henry. 2011. 'The Stellar-activity-Rotation Relationship and the Evolution of Stellar Dynamos.' ApJ 743 (December): 48.

Yeh, T. 1976. 'Mass and angular momentum effluxes of stellar winds.' ApJ 206 (June): 768–776.

Zanni, C., and J. Ferreira. 2009. 'MHD simulations of accretion onto a dipolar magnetosphere. I. Accretion curtains and the disk-locking paradigm.' A&A 508 (December): 1117–1133.

———. 2013. 'MHD simulations of accretion onto a dipolar magnetosphere. II. Magnetospheric ejections and stellar spin-down.' A&A 550 (February): A99.

Index